LOCAL MECHANICAL PROPERTIES OF PEROVSKITE OXIDE FERROELECTRIC MATERIALS

Katarina Žiberna

Doctoral Dissertation
Jožef Stefan International Postgraduate School
Ljubljana, Slovenia

Supervisor: Prof. Dr. Andreja Benčan Golob, Jožef Stefan Institute, Ljubljana, Slovenia
Co-Supervisor: Assoc. Prof. Dr. Hana Uršič Nemevšek, Jožef Stefan Institute, Ljubljana, Slovenia

Evaluation Board:
Prof. Dr. Miha Čekada, Chair, Jožef Stefan Institute, Ljubljana, Slovenia
Dr. Francisco Ruiz Zepeda, Member, National Institute of Chemistry, Ljubljana, Slovenia
Dr. Habil. Xufei Fang, Member, Karlsruhe Institute of Technology, Karlsruhe, Germany

MEDNARODNA PODIPLOMSKA ŠOLA JOŽEFA STEFANA
JOŽEF STEFAN INTERNATIONAL POSTGRADUATE SCHOOL

Katarina Žiberna

LOCAL MECHANICAL PROPERTIES OF PEROVSKITE OXIDE FERROELECTRIC MATERIALS

Doctoral Dissertation

LOKALNE MEHANSKE LASTNOSTI PEROVSKITNIH OKSIDNIH FEROELEKTRIČNIH MATERIALOV

Doktorska disertacija

Supervisor: Prof. Dr. Andreja Benčan Golob

Co-Supervisor: Assoc. Prof. Dr. Hana Uršič Nemevšek

Ljubljana, Slovenia, September 2025

Acknowledgments

I have had the pleasure of meeting and working with many incredible people during my PhD journey. Without their support and contributions, this dissertation would not have taken its current form.

First and foremost, I would like to express my deepest gratitude to Prof. Dr. Andreja Benčan Golob, whose mentorship went beyond academic guidance. She created an environment where I felt both supported and inspired. Her encouragement helped me grow not only as a scientist but also as a person. I am also deeply grateful to my co-mentor, Assoc. Prof. Dr. Hana Uršič Nemevšek, for her positivity and motivation throughout our work with atomic force microscopy. Finally, I would like to thank Prof. Dr. Barbara Malič, our department head, for giving me the opportunity to work at the Electronic Ceramics Department and for her continuous support.

I am especially grateful to Prof. Dr. Goran Dražić for always taking the time to discuss electron microscopy. Thanks to Dr. Aljaž Drnovšek for introducing me to nanoindentation and for his patient guidance. I would like to acknowledge Dr. Andraž Bradeško for the insightful discussions on the elastic properties of ferroelectrics. My sincere thanks go to Lina Lengar for her valuable help in the laboratory and to Val Fišinger for his support with atomic force microscopy.

My time at the department was made unforgettable thanks to my office mates, Dr. Samir Salmanov and Dr. Ankita Sarkar. Special thanks go to Maja Koblar for countless conversations about electron microscopy and life. Thanks also to Victor Regis for widening my perspectives and for Flagdoku.

I gratefully acknowledge the opportunity to conduct part of my research at the GREMAN laboratories in Tours. I want to thank Prof. Dr. Franck Levassort and Dr. Micka Bah for their hospitality and support during my stay.

This work was supported by the Slovenian Research and Innovation Agency through national postgraduate funding, core funding (P2-0105), and research projects (J7-4637, J2-3041, N2-0212, J2-3058, J2-2497, I0-0005), including the bilateral project with France (BI-FR/22–23-PROTEUS-10). Their financial support is gratefully acknowledged.

Finally, I would like to thank my sister and closest friends. Most of all, thank you, Anže, for your unconditional love and support.

Abstract

Ferroelectric materials have the ability to convert electrical energy into mechanical energy and vice versa, which makes them widely used as sensors, actuators, and ultrasonic transducers. While their electrical and electromechanical properties are well studied, mechanical properties like Young's modulus (E) and hardness (H) remain known to a lesser extent. Accurate knowledge of mechanical properties and determination of elastic and plastic parameters significantly contribute to more efficient modeling and prediction of the mechanical behavior of these materials.

In the doctoral thesis, we studied the elastic and plastic properties of perovskite oxide ferroelectrics and analyzed structural changes after mechanical loading down to the atomic level. The mechanical properties were determined by *in-situ* nanoindentation in a scanning electron microscope, which allowed us to target specific areas in the material (e.g., domains, domain walls (DWs)). Additionally, atomic force microscopy (AFM) was used to measure elastic properties. The results of mechanical analyses were complemented by in-depth studies of the structural and microstructural characteristics of the materials using electron microscopy.

In the first part of this thesis, we investigated the microstructural and mechanical properties of electromechanically active $0.9Pb(Mg_{1/3}Nb_{2/3})O_3$–$0.1PbTiO_3$ thick films prepared by the aerosol deposition method before and after annealing in air. We demonstrated that additional heating triggers grain growth and pore redistribution, while the mechanical properties of the films, i.e., H and E, increase by ~16 % compared to films that were not additionally heated. The microstructural changes are also reflected in a greater dispersion of the indentation curves and in a higher frequency of pop-in events.

In the second part, we examined H and E, measured via nanoindentation, as well as the plastic deformation behavior of polycrystalline $BiFeO_3$. In the force range between 200 μN and 2 mN, H and E decrease by ~37 % and ~8 %, respectively, with increasing force. The sequence of plastic deformation was revealed through the first pop-in analysis in combination with a variety of electron microscopy techniques, starting from homogeneous dislocation nucleation through the activation of the $\{110\}_{pc}\langle 1\bar{1}0\rangle_{pc}$ slip system, followed by dislocation motion and multiplication into arrays, and ultimately leading to dislocation accumulation and grain subdivision.

In the final part, we used AFM techniques to determine the elastic properties of domains and non-180° DW in $(K_{0.5}Na_{0.5})NbO_3$ single crystal. The average E measured was ~130 GPa. The domains exhibited elastic anisotropy. At 90° DW, a difference in the elastic response was observed compared to the surrounding domains, whereas at 60° DW, such a difference was not observed. It is known that the measurement is influenced by both the intrinsic elastic properties of the DWs and extrinsic contributions, such as the influence of neighboring domains and the interaction of the DW with the AFM tip.

Povzetek

Feroelektrične materiale odlikuje sposobnost pretvorbe električne energije v mehansko in obratno, zaradi česar se pogosto uporabljajo kot senzorji, aktuatorji in ultrazvočni pretvorniki. Njihove električne in elektromehanske lastnosti so zato dobro raziskane, medtem ko so mehanske lastnosti, kot sta Youngov modul (E) in trdota (H), precej manj poznane. Natančno poznavanje mehanskih lastnosti ter določanje elastičnih in plastičnih parametrov pa bistveno prispeva k učinkovitejšemu modeliranju in napovedovanju mehanskega obnašanja teh materialov.

V okviru doktorske disertacije smo preučevali elastične in plastične lastnosti perovskitnih oksidnih feroelektrikov ter analizirali strukturne spremembe po mehanski obremenitvi, vse do atomskega nivoja. Mehanske lastnosti smo določali z in-situ nanoindentacijo v vrstičnem elektronskem mikroskopu, kar nam je omogočilo ciljno merjenje specifičnih področij v materialu (npr. domene, domenske stene (DS)). Dodatno smo za merjenje elastičnih lastnosti uporabili tudi mikroskopijo na atomsko silo (AFM). Rezultate mehanskih analiz smo dopolnili s preučevanjem strukturnih in mikrostrukturnih značilnosti materialov z uporabo elektronske mikroskopije.

V prvem delu disertacije smo raziskali mikrostrukturne in mehanske lastnosti polikristaliničnih debelih plasti $0{,}9Pb(Mg_{1/3}Nb_{2/3})O_3{-}0{,}1PbTiO_3$, pripravljenih z metodo nanašanja plasti v curku aerosola, pred in po dodatnem segrevanju na zraku, ker se ta velikokrat uporablja za izboljševanje elektromehanskih lastnosti. Pokazali smo, da zrna pri dodatnem segrevanju rastejo, prihaja do prerazporeditve por, medtem ko se mehanski lastnosti plasti, tj. H in E, zvišata za ~16 % . Mikrostrukturne spremembe se odražajo tudi v večji razpršitvi indentacijskih krivulj in v večji pogostosti dogodkov, kjer merjena globina naglo poskoči pri konstantni sili (angl. pop-in).

V drugem delu smo z in-situ nanoindentacijo izmerili H in E ter raziskali plastično obnašanje polikristaliničnega $BiFeO_3$. Z višanjem sile obremenitve v območju od 200 μN do 2 mN se je H zmanjšal za ~37 %, E pa za ~8 %. V kombinaciji z različnimi tehnikami elektronske mikroskopije smo pokazali zaporedje plastične deformacije, in sicer od homogene nukleacije dislokacij z aktivacijo sistema zdrsa $\{110\}_{pc}\langle 1\bar{1}0\rangle_{pc}$, ki mu je sledilo premikanje dislokacij in njihovo množenje, kar je na koncu privedlo do kopičenja dislokacij in nastanka podzrn.

V zadnjem delu doktorske disertacije smo z uporabo tehnike AFM določili elastične lastnosti domen in ne-180° DS monokristalu $(K_{1/2}Na_{1/2})NbO_3$. Povprečni izmerjeni E je ~130 GPa. Domene so elastično anizotropne, pri 90° DS smo opazili razliko v elastičnem odzivu v primerjavi z okoliškimi domenami, medtem ko pri 60° DS tega nismo opazili. Znano je, da na rezultate meritev vplivajo tako intrinzične elastične lastnosti same DS kot zunanji dejavniki, kot sta vpliv sosednjih domen ter interakcija sten in konice AFM.

Contents

List of Figures

Abbreviations

(S)TEM ... (scanning) transmission electron microscopy
4D STEM ... four-dimensional scanning transmission electron microscopy
AC ... alternative current
AFM ... atomic force microscopy
BF ... bright field
BSE ... backscattered electrons
CoM ... center of mass
CRFM ... contact resonance frequency mapping
DW ... domain wall
EBSD ... electron backscatter diffraction
EDS ... energy dispersive X-ray spectroscopy
EELS ... electron energy loss spectroscopy
FIB ... focused ion beam
GND ... geometrically necessary dislocations
HAADF ... high angle annular dark field
ISE ... indentation size effect
pc ... pseudo cubic
PF-QNM ... peak force quantitative nanomechanical mapping
PFM ... piezoresponse force microscopy
PZT ... lead zirconate titanite
SAED ... selected area electron diffraction
SE ... secondary electrons
SEM ... scanning electron microscopy
TKD ... transmission Kikuchi diffraction
WDS ... wavelength dispersive X-ray spectroscopy

Symbols

A ... projected contact area
a_c ... cell constant a in the cubic unite cell
a_t ... cell constant a in the tetragonal unite cell
$\mathbf{b}$ ... Burgers vector
C ... elastic constant
c_t ... cell constant c in the tetragonal unite cell
E ... Young's modulus
E_p ... Young's modulus of the probe
E_r ... reduced Young's modulus
F ... force
F_0 ... force measure at the first pop-in
F_{max} ... maximum force
H ... hardness
h_c ... depth over which the contact is made
P_s ... spontaneous polarization
R ... radius of the curvature of the indentation probe
S ... stiffness of the elastic contact
T ... temperature
T_C ... Curie temperature
Z ... atomic number
ε ... strain
ν ... Poison ratio
ν_p ... Poison ratio of the probe
σ ... stress
τ_{max} ... maximum sheer stress
τ_{th} ... theoretical sheer stress

Chapter 1

Introduction

The chapter Introduction provides a literature overview of the topic considered relevant for this thesis. Firstly, the motivation for the work at hand is presented. The chapter continues with an overview of the fundamentals of ferroelectrics and mechanical properties. The final part focuses on local mechanical measurements, which are supported by examples from the literature.

1.1 Motivation

Perovskite oxide ferroelectric materials are technologically significant and play a crucial role in our modern way of life. The dielectric, piezoelectric, and ferroelectric properties they possess make them the bases of sensors, actuators, ultrasonic transducers, and energy-harvesting devices [1]. Mechanical properties represent a crucial yet often overlooked aspect of ferroelectric materials, having historically been explored to a much lesser extent than their functional properties [2].

In terms of mechanical properties, ferroelectrics are often described as "brittle" at room temperature conditions, with a fracture toughness in the range of a few $MPam^{1/2}$ [3], [4]. This description is based on comparisons with metals whose fracture toughness can reach several hundreds of $MPam^{1/2}$. The term "brittle" in this case is used too broadly, as the deformation of ferroelectric materials through dislocation-mediated plasticity will be affected by many parameters, such as temperature, the force applied, and the size of the testing sample. In addition, several perovskites exhibited "surprising" deformation, namely $SrTiO_3$ [5], [6], $KTaO_3$ [7], and ferroelectric $KNbO_3$ [8]. Furthermore, overcoming the inherent brittleness and improving the plastic deformability of ferroelectrics, as well as of other non-ferroelectric perovskites, is being addressed in several ways. One approach is through structural and microstructural engineering via non-conventional synthesis routes that influence the dislocation density within the samples, for example, as in the case of cold sintering [9], [10], or favor another deformation mechanism over dislocation-mediated plasticity, e.g., grain boundary sliding as in aerosol-deposited thick films [11], [12]. Alternatively, deformability is enhanced by introducing dislocations into dislocation-depleted samples after synthesis through controlled mechanical deformation at various length scales [13]–[16]. The introduced dislocations will, in addition to affecting mechanical properties, also modify the macroscopic ferroelectric response, making them effective defects for controlling electromechanical properties [17], [18]. A thorough understanding of the mechanisms of deformation at different length scales of ferroelectric perovskites is essential for effectively tailoring their mechanical response and/or functional properties.

The elastic properties of ferroelectrics have also been overlooked. Within ferroelectric materials, elasticity changes locally through the ferroelectric domain structure and can be

manipulated via domain structure engineering to achieve desired elastic properties. Regions with homogeneous spontaneous polarization direction, known as domains, exhibit anisotropic elastic properties dependent on the direction of spontaneous polarization [19]–[21].

Domain walls (DWs), which are the interphases separating domains, exhibit their distinct elastic responses. For example, 180° DWs have been shown to exhibit a lower Young's modulus, reduced by approximately 19 %, compared to their neighboring domains with out-of-plane spontaneous polarization. This trend has been observed across various compositions, including periodically poled $LiNbO_3$, $BaTiO_3$, and $PbTiO_3$, as well as in different morphologies, such as crystals and thin films [19]. In contrast, the elastic response of 90° DWs is more complex. For inclined 90° DWs, Young's modulus increases on one side of the DW and decreases on the other [20]. Although the origin of the distinct mechanical behavior of DW is still not understood in full, proposals have been made on how this property can be exploited, for example, in thermal switches. Since elastic properties will influence the phonon scattering and heat propagation, DWs with a different Young's modulus could serve as nanochannels within which the heat will propagate at a different speed [19]. The newly discovered properties offer opportunities to reuse already well-known ferroelectric materials in novel applications.

1.2 Ferroelectric Materials

1.2.1 Basic Characteristics

By definition, ferroelectric materials are a subgroup of dielectric materials that have two key properties [22]:

a) They have a net internal electrical dipole called spontaneous polarization (P_s) in the absence of an external electric field,
b) The P_s can be switched by application of an external electric field.

P_s forms naturally as a ferroelectric material is cooled down over a critical temperature called the Curie temperature (T_C), at which a break in the structure's symmetry occurs. Figure 1.1 depicts the rise of P_s in the oxide perovskite structure ABO_3, one of the most technologically relevant types of ferroelectrics [23], which is also the focus of this thesis. At high temperature, the structure is in a centrosymmetric paraelectric phase. Upon reaching T_C, the paraelectric phase transitions to a non-centrosymmetric ferroelectric characterized by a displacement of ions from their equilibrium positions. As simplistically shown in Figure 1, this transition involves a relative shift of the B atom with respect to the A sublattice and the O sublattice. Consequently, the offset of ions leads to a displacement of the center of the positive and negative charge in the structure, giving rise to an intrinsic electric dipole.

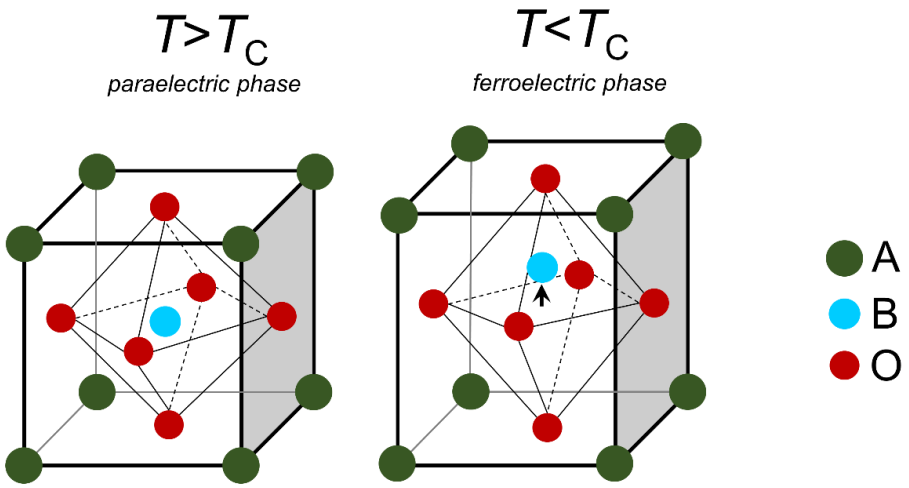

Figure 1.1: Simplified schematic of a perovskite unite cell a) in the centrosymmetric paraelectric phase when temperature (T) is higher than the T_C and b) in the non-centrosymmetric ferroelectric phase at T lower than T_C. The arrow marks the displacement of the central B atom from its equilibrium position as well as the direction of P_s. Adapted after [22].

A characteristic feature of ferroelectrics are ferroelectric domains-regions of uniformly ordered P_s within the material. The subdivision into domains is caused by the material's need to minimize the electrostatic energy from the depolarizing field that forms at the material surface during the transition from the paraelectric to the ferroelectric phase and the elastic energy from mechanical stresses acting on/in the material. The morphology of the domains and, thus, the domain structure of a single crystal, a polycrystalline material (a ceramic), and a thin film differ due to different boundary conditions, both electrostatic and elastic [22].

Interfaces where the P_s vector transitions from one direction to another are referred to as domain walls (DWs). Depending on the symmetry of the ferroelectric phase, different types of DWs are created at the transition over T_C. DWs are classified by the angle between the P_s vectors in the adjected domains. In a tetragonal system, where the P_s vector forms along $\{001\}_{pc}$ planes, 180° and 90° DW will form, as depicted in Figure 1.2. Similarly, in a rhombohedral system, the P_s will be along $\{111\}_{pc}$ planes, leading to the formation of 180°, 109°, and 71° DWs, while in an orthorhombic system, the P_s lies along $\{110\}_{pc}$ planes leading to the formation of 180°, 120°, 90° and 60° DWs [24]. The notation pc denotes the pseudocubic symmetry metric. In principle, a division is made between 180° DWs and non-180° DWs due to their different properties. 180° DW are exclusively ferroelectric in character and, thus, their dynamics can only be triggered by electric fields, while non-180° DWs have ferroelectric and ferroelastic characteristics, implying that they are not only mobile under electric field but also under mechanical stress.

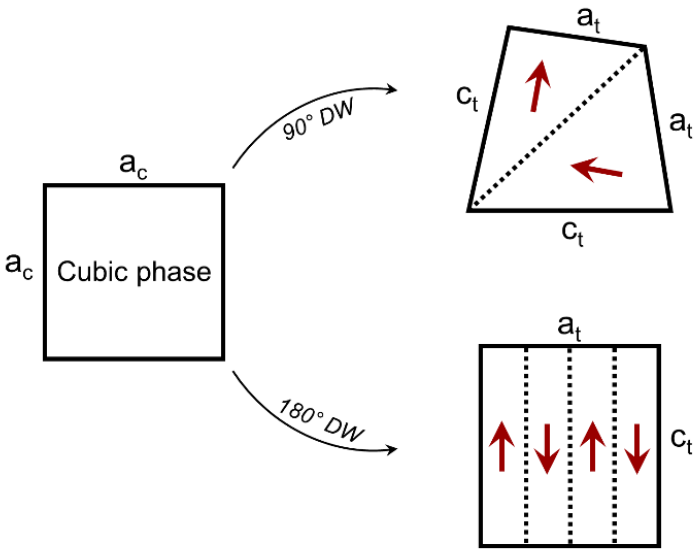

Figure 1.2: Formation of 180° and 90° DWs in a tetragonal ferroelectric material as it is cooled down from the cubic phase. Red arrows represent the direction of P_s. DWs are drawn as dashed lines. a_c, a_t, and c_t, indicate the lattice cell parameters of the a cubic axis, the a tetragonal axis, and the c tetragonal axis, respectively. Adapted after [22].

1.2.2 Electromechanical Coupling

Ferroelectric materials exhibit several electromechanical phenomena by which the material changes dimensions when an electric field is applied. The electromechanical response can arise from three intrinsic lattice effects: piezoelectricity, electrostriction, and flexoelectricity.

The *piezoelectric effect* describes the polarization of a material in response to an applied mechanical force, as shown in Figure 1.3a. The relationship is linear, with the generated electric charge and the applied stress connected by the piezoelectric coefficient. Via the converse piezoelectric effect, the opposite can be achieved: the material will deform when exposed to an external electric field. Again, the relation between the resulting strain and the electric field is governed by the piezoelectric coefficient. Piezoelectricity is only present in materials that belong to non-centrosymmetric point groups, with the exception of the non-centrosymmetric point group 432, which is non-piezoelectric. The ferroelectric materials are the subgroup of piezoelectric materials [22].

Unlike piezoelectricity, *electrostriction* is independent of material symmetry and can thus be found in all materials. It describes the quadratic relation between the strain and the electric field applied, connected by the electrostriction coefficient. This phenomenon results in material deformation that is independent of the polarity of the applied electric field [25].

Flexoelectricity, on the other hand, describes the linear coupling between polarization and inhomogeneous strain. Contrary to piezoelectricity and electrostriction, flexoelectricity arises from strain gradients, as shown in Figure 1.3b, which locally break centrosymmetry and polarize the material. The relationship between strain gradients and polarization is governed by the flexoelectric coefficient [26].

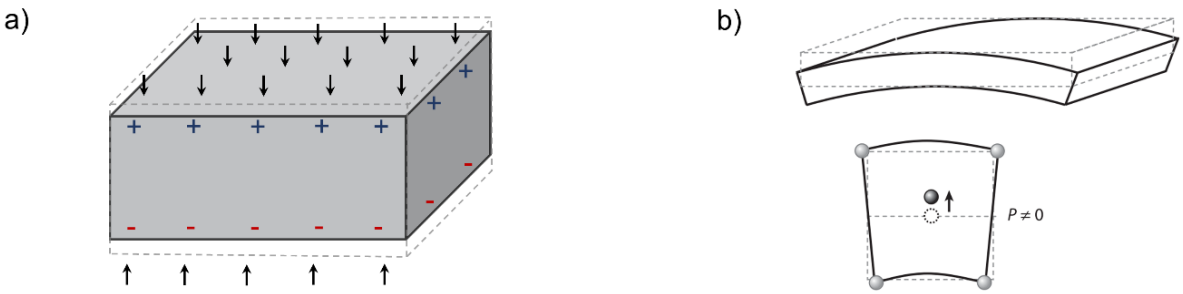

Figure 1.3: a) Direct piezoelectric effect generating positive and negative charge as the material is compressed; b) Strain gradient, in this case, caused by bending, leads to a displacement of the positive and negative charge centers, polarizing the material (from [26]). The dashed lines represent the material shape before deformation.

1.2.3 Characterization of Ferroelectric Materials Using Electron Microscopy

Electron microscopy is an analytical tool that is indispensable for characterizing ferroelectric materials. Its versatility enables simultaneous imaging in both real and reciprocal space, as well as chemical and crystallographic orientation analysis, providing comprehensive information about the microstructure, crystal structure, and chemistry, spanning from the microscale down to the atomic level.

The basic principle involves accelerating electrons through vacuum, shaping the electron beam using electromagnetic lenses within the electron column, and collecting the signals generated by the interaction of electrons with the sample. Depending on the interaction, signals can be broadly categorized into two groups: signals that escape the sample surface after the interaction, which is usually the case in scanning electron microscopy (SEM), and signals that are created from electrons passing through the sample as in the case of (scanning) transmission electron microscopy ((S)TEM).

1.2.3.1 Scanning Electron Microscopy

The three most useful signals in SEM are the secondary electrons (SE), backscattered electrons (BSE), and characteristic X-rays generated during the interaction of the primary electron beam with the sample. Inelastic scattering of primary electrons by the sample's electron cloud leads to the emission of SEs. The SEs have low energies, typically 50 eV or less, and only those generated near the surface can escape, resulting in a topography-sensitive image [27]. As illustrated schematically in Figure 1.4a, the contrast mechanism relies on variations in the number of SEs emitted from flat versus inclined surfaces, allowing for detailed visualization of surface features.

In contrast, BSEs are generated by elastic interactions between the primary electrons and the atomic nuclei. Such interactions alter the trajectories of the primary electrons with minimal energy loss. Therefore, BSEs have energies close to the incident beam energy, and the BSE signal is less surface-sensitive, as it is formed deeper compared to the SE signal. The intensity of backscattering increases with the atomic number (Z), resulting in composition contrast on the BSE images. The composition contrast obtained by BSE imaging is particularly useful for distinguishing different phases that may form during processing. Figure 1.4b shows undesirable secondary phases that often form in $BiFeO_3$ during solid-state synthesis [28]. In addition, BSE imaging is also employed in the study of ferroelectric materials to reveal domain structures by an orientation-sensitive contrast

mechanism known as electron channeling. The contract is based on the different orientations of the atomic columns, which affect the penetration depth of the primary electron beam, resulting in a contrast due to variation in crystallographic orientation. An example of domain imaging with electron channeling is shown in Figure 1.4c, along with the schematically drawn mechanism.

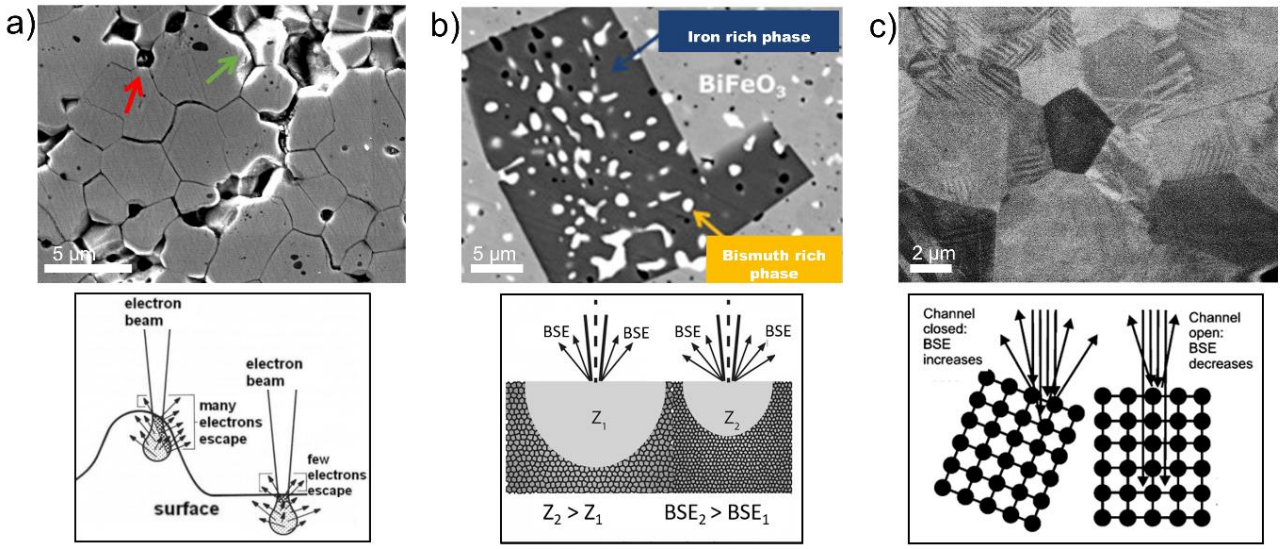

Figure 1.4: Topographic contrast (by SEs), compositional contrast (by BSEs), and electron channeling contrast (by BSEs). $BiFeO_3$ ceramic imaged with a) SEs, the red arrow indicates dark pores and the green arrow indicates brighter unpolished grains [29] and b) BSEs, blue and yellow arrows indicate the iron-rich (dark grey, low Z inclusions) and the bismuth-rich phases (brighter, high Z phase) [30]. c) Domain structure of $Pb(Mg,Nb)O_3$–$PbTiO_3$ ceramics imaged with BSEs. Below each example, the corresponding contrast-forming mechanisms are schematically illustrated. Adapted after [27] and [31].

Primary electrons can diffract on the specimen crystal planes. Such a signal gives information about the crystallographic orientation from a few nanometers below the surface, and it is thus very important that the surface is flattened and polished prior to analysis. The diffraction of the electrons is the basis for a technique called electron backscattered diffraction (EBSD). In addition, diffraction can be performed in transmitted mode, also referred to as transmission Kikuchi diffraction (TKD).

Finally, X-rays can be formed as the primary electrons interact with and eject the electrons from the inner shells of atoms. The atom then fills the inner shell vacancy with an electron from the outer shell, emitting an X-ray photon. The energy difference between two electron shells is element-specific and thus provides information about the exact chemical composition of the specimen. X-rays are the basis for two electron-probe microanalytical techniques within a SEM: energy-dispersive X-ray spectroscopy (EDS) and wavelength-dispersive X-ray spectroscopy (WDS).

1.2.3.2 (Scanning) Transmission Electron Microscopy

In TEM, a parallel beam of primary electrons is used to illuminate the electron-transparent sample. This leads to scattering/diffraction (the term “scattering” is used when considering the particle nature of an electron, while “diffraction” is used when considering its wave nature) of electrons, which form the basis for imaging and diffraction. TEM can, therefore, be used for imaging in real space or for obtaining information in reciprocal space using selected area electron diffraction (SAED) based on Bragg’s law [32]. SAED can be

particularly valuable for assessing DW types by comparing experimental SAED patterns with simulated ones. For example, Figure 1.5 illustrates how reflections split in the presence of non-180° DWs in $BiFeO_3$ due to slight variations in unit cell parameters between adjacent domains when viewed along a specific zone axis. The 180° DWs do not cause splitting.

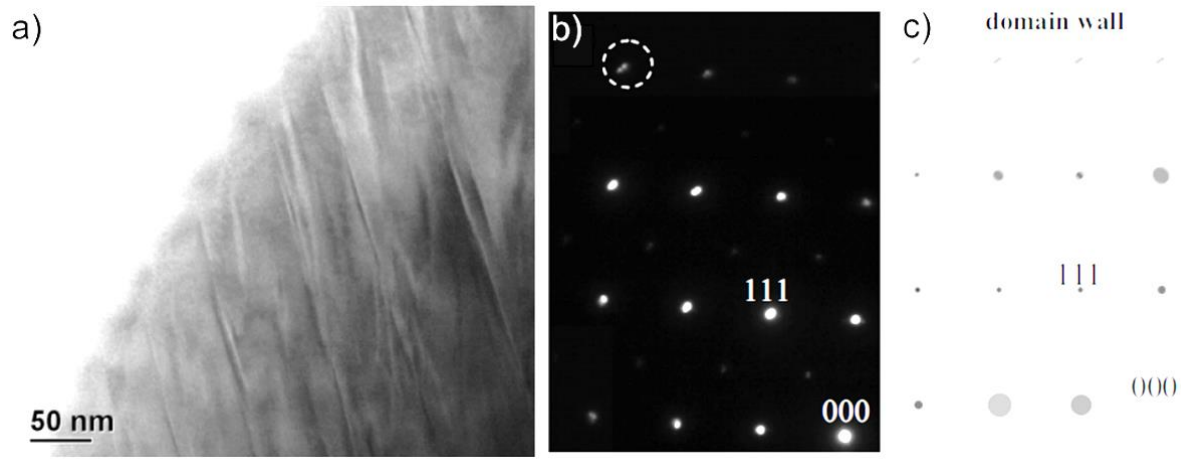

Figure 1.5: a) BF TEM image of domains in $BiFeO_3$ ceramic; b) Experimental SAED patterns taken in [110] zone axis showing splitting of the (333) reflections; c) simulated SAED of a 71° DW. Adapted after [33].

Instead of parallel electron illumination, as in TEM, STEM uses a converging beam that is scanned over the sample by scanning coils. Annular detectors then collect the electrons elastically scattered at each probe position to form images. The high-angle annular dark field (HAADF) detector, for example, collects off-axis scattered electrons and provides chemistry-based contrast, also known as Z-contrast, due to the dependence of the signal on the Z number ($\sim Z^{1.7}$) [34]. A limitation of HAADF is the inability to image light elements such as oxygen. An alternative is bright field (BF) imaging, which captures on-axis forward-scattered electrons as well as the unscattered beam and can also visualize light elements [32], [35].

Most STEM imaging techniques, including HAADF and BF, collect a portion of the diffracted electrons that fall on the detector, integrate them, and display the collected signal as intensity on a greyscale at each probe position. The information about the location where each diffracted electron hits the detector is thus lost. A pixelated detector, on the other hand, makes it possible to image the entire diffraction pattern by registering the locations where the diffracted electrons are detected. The imaging of reciprocal space at each probe position in real space is referred to as four-dimensional STEM (4D STEM). Capturing the diffraction pattern at each probe position offers extensive analysis possibilities. The simplest is a virtual reconstruction of the HAADF and BF image using a so-called virtual detector. Other analyses include, for example, the center of mass (CoM) analysis, where displacements of the diffracted beam caused by internal field(s) within the sample are evaluated and related to various properties such as electrostatic potential, magnetic fields, and strain [34]–[36].

Finally, as in SEM, (S)TEM also uses analytical techniques based on inelastically scattered electrons, namely EDS and electron energy loss spectroscopy (EELS). While both techniques provide information about the chemistry, EELS offers better energy resolution and can be used to detect light elements, determine oxidation states, and identify bonding, and is therefore used to complement EDS.

1.3 Mechanical Properties

While the primary focus of this thesis is on ferroelectric oxide perovskites, non-ferroelectric oxide perovskites will also be discussed in this chapter, namely $SrTiO_3$, which is one of the more extensively studied perovskite oxides in terms of mechanical properties.

1.3.1 Elastic and Plastic Deformation

The mechanical properties describe how a material reacts when a force is applied. The properties are primarily related to interatomic bonding, the structure, and the microstructure of the investigated material, and determine the elastic (reversible) and plastic (irreversible) deformation under stress. Figure 1.6a depicts the relationship between stress and strain during a tensile test, which will be used as an example to explain elasticity and plastic deformation.

When initially applying stress, the material will first respond elastically and return back to the original form when the stress is removed. The elastic deformation can be seen as a linear progression of the stress-strain curve in Figure 1.6a and can be described by Hooke's law. For anisotropic materials, both stress and strain are described as tensors, and Hooke's law can be written as [37]:

$$\sigma_{ij} = C_{ijkl}\varepsilon_{kl}, \tag{1.1}$$

where σ_{ij} denotes the stress tensor, ε_{kl} the strain tensor, and C_{ijkl} the elastic constants. For isotropic materials, the elastic constant matrix is reduced to one constant referred to as the elastic modulus or Young's modulus (E) [Pa]. Alternatively, elasticity can be expressed as stiffness [Nm^{-1}].
In the later stage, at a point referred to as the yield point or strength, the material starts to deform plastically until failure occurs (Figure 1.5a). Two different examples of plastic deformation are shown in Figure 1.6b, i.e., stress-strain curves for a brittle and a ductile material, respectively. Brittle materials withstand higher yield stresses compared to ductile materials, but they fracture after little or no plastic deformation, whereas ductile materials withstand a significant amount of plastic deformation before failure. A property that refers to the plastic deformability of the material is hardness (H) [Pa], which describes the resistance of a material to penetration of another harder material.

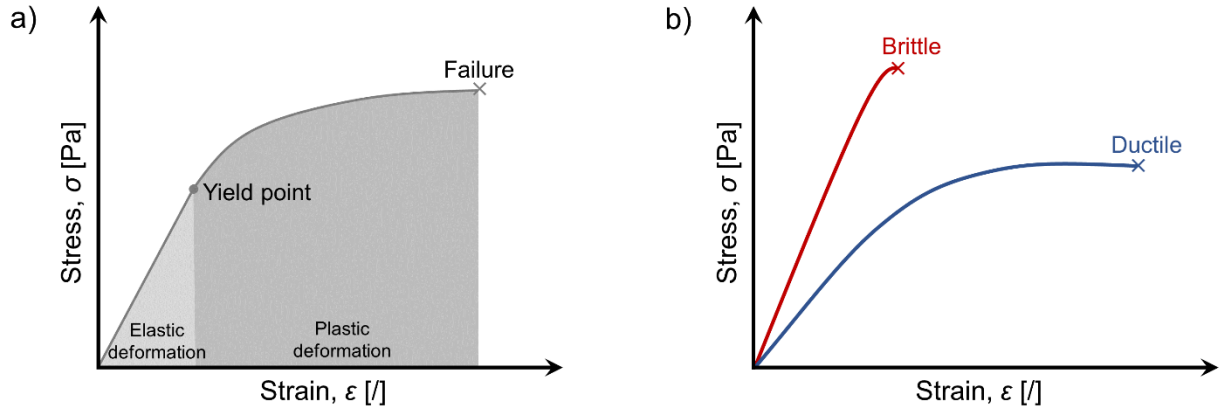

Figure 1.6: a) Stress-strain curve, b) Stress-strain curves of a brittle and ductile material.

1.3.2 Dislocations and Their Role in Plastic Deformation

Perhaps the most well-known carriers of plastic flow are found in metals, where plasticity is primarily governed by dislocations, one-dimensional crystallographic defects, where a half-plane of atoms is inserted between two atomic planes, as shown in Figure 1.7a. However, the ionic/covalent nature of bonds in perovskites has significant implications for the structure and motion of dislocations.

Firstly, in perovskite (as well as other ionic solids), dislocations are characterized by a relatively large Burgers vector **b** (Figure 1.7a) compared to metals. To maintain local charge neutrality, the extra half-plane must include both cations and anions [38]. Additionally, ionic bonding restricts the available slip systems, preventing ions of the same charge from passing over each other. As a result, the only active slip system in perovskites at room temperature is <110>{1$\bar{1}$0}where the {1$\bar{1}$0} planes glide in the <110> direction [2].

High-temperature annealing, either calcination and/or sintering, makes perovskites nearly dislocation-free, with a dislocation density of approximately 10^9 m^{-2} [15]. For comparison, the dislocation density of metals is roughly 10^{13} m^{-2}. The vast majority of dislocations thus need to be freshly nucleated during mechanical loading. This can happen by homogeneous nucleation, where the maximum shear stress (τ_{max}) must exceed the theoretical shear strength (τ_{th}) [13], [39] of

$$\tau_{th} \sim \frac{E}{4\pi(1+\nu)}, \tag{1.2}$$

where E is the Young's modulus and ν is the Poisson's ratio [/]. On the other hand, heterogeneous nucleation requires less stress than homogeneous nucleation, as it occurs from pre-existing defects. Various defects can serve as nucleation sources, including precipitates, dislocation loops, and even surface terrace steps [40].

Another big challenge for dislocations in perovskites is their motion. Dislocation motion proceeds step by step, with the half-plane advancing one unit cell at a time while overcoming lattice friction, also known as the Peierls barrier. In ceramics, this barrier can be particularly high, sometimes exceeding 5 GPa, making dislocation movement significantly difficult. Such high stresses can lead to the formation of cracks rather than sustained plasticity. The motion is mainly carried by the kink-pair mechanism [8], [41] and is presumed to be highly dependent on the dislocation core structure [42]. To reduce the energy required for motion, dislocations in perovskites often dissociate into two colinear partial dislocations and a stacking fault [43], as illustrated in Figure 1.7b:

$$\langle 110 \rangle \rightarrow \frac{1}{2}\langle 110 \rangle + \text{stacking fault} + \frac{1}{2}\langle 110 \rangle. \tag{1.3}$$

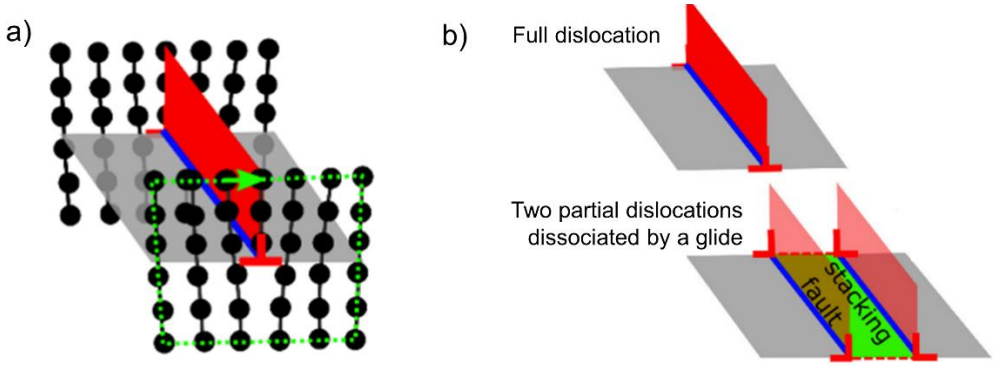

Figure 1.7: a) Schematic of an edge dislocation. The end of the inserted half-plane is marked by a red inserted T. The Burgers vector is drawn with a green arrow closing the Burgers circuit (green dashed line) drawn around the dislocation; b) Compression of a full dislocation with a dissociated dislocation into two partial dislocations and a stacking fault. Adapted after [2].

During motion, a dislocation can multiply through a number of mechanisms. In contrast to metals, where the dislocations predominantly multiplies from Frank-Read sources, a multiplication mechanism in which a pinned dislocation segment bends outward to form a loop that eventually detaches [38], multiplication in perovskites is presumably dominated by (multiple) cross-slip [8], with Frank-Read sources contributing minorly.

A comprehensive review on dislocations in ceramics can be found in Ref. [2], which provides a detailed discussion on dislocation formation, multiplication, and motion. However, plastic deformation in perovskites is not limited to dislocation activity; depending on the material's structural and microstructural characteristics, alternative mechanisms such as grain boundary sliding and twinning can also play a significant role.

1.4 Local Measurements of Mechanical Properties

1.4.1 Nanoindentation

Indentation is a versatile mechanical testing tool used to determine mechanical properties such as H and E, fracture toughness, creep, and phase transformations. It involves pressing an indentation probe (usually made of diamond) into the surface of a material while precisely controlling and recording the applied force and the resulting penetration depth.

1.4.1.1 Calculation of Hardness and Young's Modulus

During indentation, the indentation probe of a selected geometry controllably imprints into the sample surface until a maximum force (F_{max}) is reached. Figure 1.8a shows the surface profile at F_{max} and after the release of the force. At F_{max}, hardness can be calculated as

$$H = \frac{F_{max}}{A}, \tag{1.4}$$

where A [m^2] is the projected contact area calculated from the depth over which the contact is made (h_c) [m] considering the geometry of the indentation probe. h_c is read out from the depth measured during the application of the force, i.e., the force-depth indentation curve, as shown in Figure 1.8b.

The indentation curve is composed of two main parts: the loading portion of the curve and the unloading portion of the curve. The loading curve forms due to both elastic and plastic deformation of the material, while the unloading portion is caused by the elastic recovery of the material during unloading. Under this assumption, the reduced Young's modulus (E_r) can be calculated from the slope of the upper portion of the unloading curve that represents the stiffness of the elastic contact (S) [Nm^{-1}] as such:

$$E_r = \frac{\sqrt{\pi}}{2}\frac{S}{\sqrt{A}}. \tag{1.5}$$

E can be calculated from E_r by considering the elastic properties of the indentation probe (E_p) and the Poisson's ratios of both the probe (ν_p) [/] and the sample (ν) [44]:

$$\frac{1}{E_r} = \frac{(1-\nu_p^2)}{E_p} + \frac{(1-\nu^2)}{E}. \tag{1.6}$$

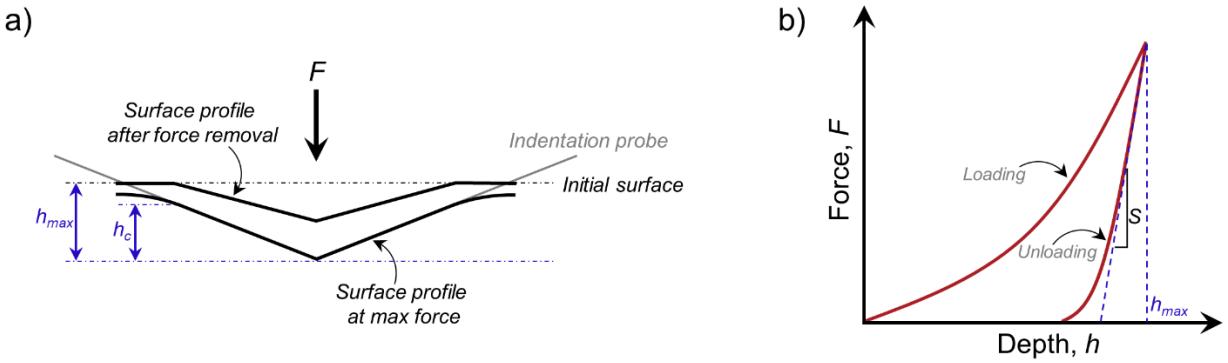

Figure 1.8: a) Cross-section of an indentation marking the profile of the surface at the maximum force applied and after the removal of the force; b) Indentation force-depth curve. Adapted after [44]. h_{max} and h_c represent the indentation depths at maximum force and after unloading, respectively, while S denotes the slope of the unloading curve, corresponding to the contact stiffness.

Nowadays, depth-sensing indentation instruments can be highly accurate, measuring the displacements of the indentation probe with high resolution, typically in the range of less than a nanometer, using a piezoelectric flexure or a three-plate capacitive transducer. Such instruments are referred to as nanoindentation systems. Nanoindentation offers an advantage over traditional macroscopic mechanical measurements by enabling the evaluation of specific features or small specimens. This capability is further enhanced when utilizing an *in-situ* indentation system [45], where the measuring system is placed inside an electron microscope (a SEM or a TEM), allowing for the accurate positioning of the indentation probe.

In the field of perovskites, nanoindentation plays a crucial role, primarily due to its ability to determine E and H with a high spatial resolution, particularly for films on substrates. For instance, nanoindentation has been used to assess the mechanical properties of a thick film prepared using aerosol deposition, i.e., a room-temperature deposition method where ceramic particles are accelerated with high kinetic energy toward a substrate, and the film grows by impact consolidation and fracture of the initial powder particles [46], [47]. Nanoindentation studies revealed that post-annealing an aerosol-deposited $BaTiO_3$ film on a stainless-steel substrate at 500 °C increased its E from ~130 GPa to ~150 GPa and its H from ~8 GPa to ~11 GPa. The authors attributed these enhancements, shown in

Figure 1.9, as a function of indentation depth, grain reorientation, space charge effects, and the relaxation of internal stresses [11]. However, further annealing up to 750 °C resulted in a decrease in E and H, accompanied by increased scattering of the force-displacement curve distribution. The decline was linked to grain growth, which resulted in an inhomogeneous microstructure, the development of internal stresses, and, ultimately, crack formation [48].

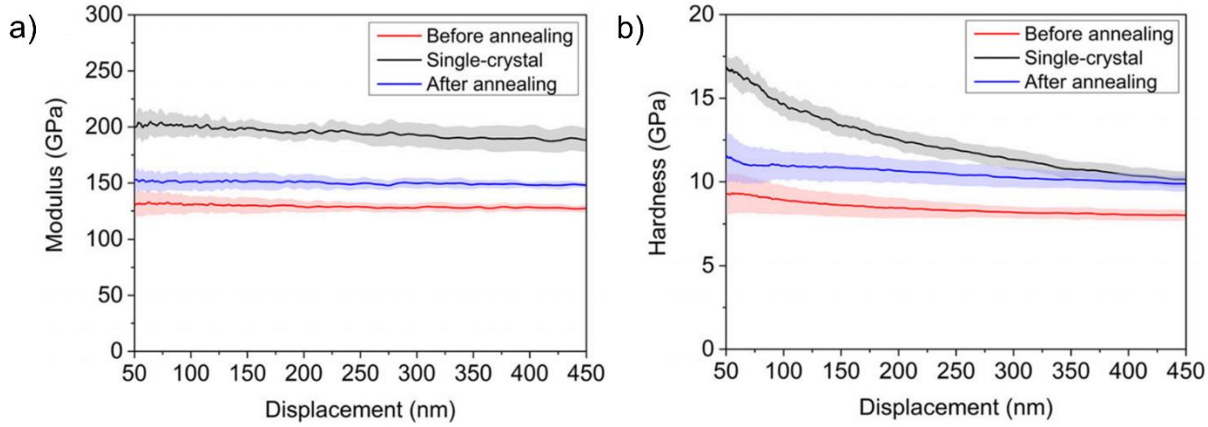

Figure 1.9: a) E and b) H as a function of indentation depth of pristine aerosol deposited $BaTiO_3$ film (red curve), the aerosol deposited $BaTiO_3$ annealed at 500 °C (blue curve) and a $BaTiO_3$ single crystal. The variation of E and H with indenter displacement was measured using nanoindentation in the continuous stiffness measurement mode (from [11]).

While nanoindentation is the method of choice for determining the E and H of films, there are some limitations of the technique that are often overlooked. One major concern is the influence of the substrate's mechanical properties on the measured values, especially on E. To mitigate this effect, the indentation depth should not exceed 10 % of the film thickness, as recommended by the standard ISO 14577-1:2015 for instrumented indentation testing of hardness [49]. This guideline, originally proposed by Bückle, is valid only for hard films on softer substrates and primarily applies to hardness measurements [50]. The plastically deformed zone, from which information about H is obtained, is localized around the indentation, as schematically illustrated in Figure 1.10a.

In contrast, the elastically deformed zone, which influences the measurement of E, is significantly larger than the plastic zone, as shown in Figure 1.10b [51], elastically deforming not only the film but also the substrate, making the 10 % rule inadequate for accurate E measurements in films. To improve accuracy, it has been proposed that the indentation depth be kept below 1 % of the film thickness [52]. Alternatively, a continuous stiffness measurement can be performed to monitor variations in E with indentation depth, ensuring reliable results and avoiding artifacts caused by the substrate, as demonstrated in the study presented in Figure 1.9a. If the substrate is found to influence E with increasing indentation depth, an extrapolation to zero penetration depth can be made to determine the true E of the film, as was done for La-doped $Pb(Zr,Ti)O_3$ (PZT) films with an E of 130 GPa [53].

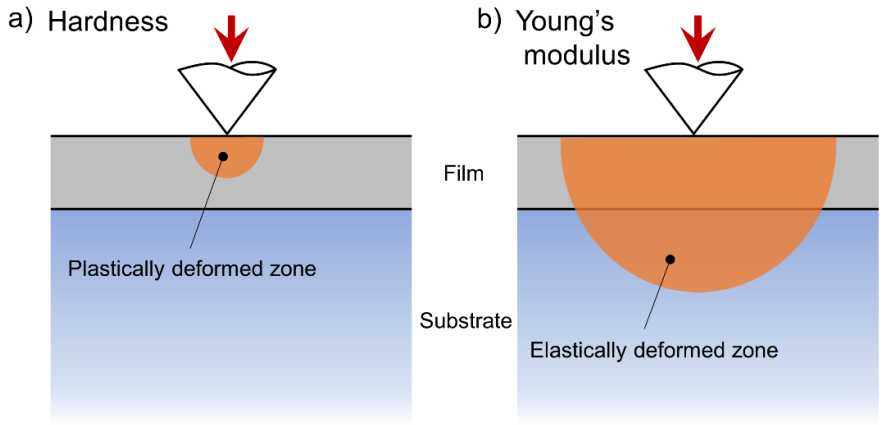

Figure 1.10: Schematically depiction of the sizes of a) the plastically deformed zone and b) the elastically deformed zone, which can extend into the substrate during the indentation of a film on a substrate. Adapted after [51].

Similarly to films on substrates, other heterostructures, secondary phases, and microstructural features, such as grain boundaries and pores, also influence the measured E. The E across the ferroelectric domains will also vary. Domains separated by non-180° DW, namely 90° DWs, have been observed to exhibit different E values for domains with in-plane P_s (a-domains) and domains with out-of-plane P_s (c-domains). However, E depends on the indentation position, as both neighboring domains undergo elastic deformation and contribute to the measurement [21]. In contrast, domains separated by 180° DWs should theoretically have identical elasticity. However, they can still be distinguished using nanoindentation due to changes in overall polarization and inhomogeneous strains generated during the indentation process. Specifically, downward-polarized domains were found to be stiffer than upward-polarized domains [54].

1.4.1.2 Elucidating Plastic Deformation Mechanisms

Imprinting a material with a probe induces significant plastic deformation. The resulting indentation curves are thus rich in information about the mechanisms of plastic deformation.

By comparing the evolution of H as a function of indentation depth of aerosol-deposited $BaTiO_3$ film and single crystal $BaTiO_3$ (Figure 1.9b) it was observed that while H of aerosol-deposited films remained constant, while it decreased at shallow depths before stabilizing in the single crystal [11]. The decrees of H with increasing indentation depth is a phenomenon called indentation size effect (ISE), where materials indented at lower forces (at the nanoindentation level, where indentation depths are below the micrometer regime) appear to be harder than they do macroscopically. Nix and Gao explained ISE through a model involving geometrically necessary dislocations (GNDs), which form during indentation to accommodate plastic deformation and the associated strain gradient [55]. In $BaTiO_3$ single crystal, plastic deformation is governed by the formation of GNDs, leading to a visible ISE. In contrast, aerosol-deposited films exhibit no apparent ISE, suggesting other mechanism(s). Specifically, deformation in these films is believed to be dominated by grain boundary sliding and the plastic flow of an amorphous phase present between grains [11].

For cases where dislocation-based plasticity is the primary deformation mechanism, the force-displacement curves can be used to assess the nucleation of dislocations by performing

an analysis of the first pop-ins. For a dislocation-free material, such as a $SrTiO_3$ single crystal (Figure 1.10a) [15], in the very early stages of indentation with a sharp indentation probe [39], the material will first deform elastically, as shown in Figure 1.11b. The elastic behavior of the material can be described by the Hertzian theory of elastic contact [56], [57] as shown in Figure 1.11a according to the equation:

$$F = \frac{4}{3} E_r \sqrt{R} h^{\frac{3}{2}}, \tag{1.7}$$

where R represents the radius of the curvature of the indentation probe and h is the indentation depth. At a certain point, the indentation curve deviates from the predicted elastic behavior, i.e., the Hertzian behavior, which is observed as an abrupt jump in displacement at a constant load. The feature is referred to as the first pop-in and marks the transition from elastic to elasto-plastic behavior of the material, where the onset of plasticity is associated with dislocation activity. Care should be taken in the first pop-in assignation, as cracking and phase transitions could also result in pop-in events [58].

From the first pop-in, the τ_{max} needed for the material to deform plastically can be expressed as [57]:

$$\tau_{max} = 0.31 \left(\frac{6E_r^2}{\pi^3 R^2} F_0\right)^{\frac{1}{3}}, \tag{1.8}$$

where F_0 is the force measured at the first pop-in. In the example in Figure 1.11a, b, e, τ_{max} of a $SrTiO_3$ single crystal with a dislocation density of $5 \cdot 10^9$ m^{-2} was found to be close to τ_{th}~17 GPa (Figure 11e, red data points) [15]. Further loading, however, will lead to multiplication and motion of dislocations, resulting in dislocation pile-up and, consequently, crack formation, as proposed by the Zener-Stroh model [59]–[61]. Regions of high dislocation density can also develop an ordered structure characterized by the arrangement of dislocations in sub-boundaries and the subsequent formation of sub-grains, as has been reported in $SrTiO_3$ [14].

In dislocation-enriched $SrTiO_3$, with a near-surface dislocation density of $5 \cdot 10^{14}$ m^{-2} (Figure 1.11c, d, e), the first pop-in occurs at a much lower indentation force (Figure 1.11d), and τ_{max} is significantly reduced (Figure 1.11e, blue data points). This reduction results from inhomogeneous dislocation nucleation, which requires lower stress compared to the nucleation of dislocations from a pristine crystal lattice. Given that the stress required to move a dislocation in $SrTiO_3$ is only 60 MPa [5], the presence of pre-existing dislocations facilitates plastic deformation at much lower stress levels [15].

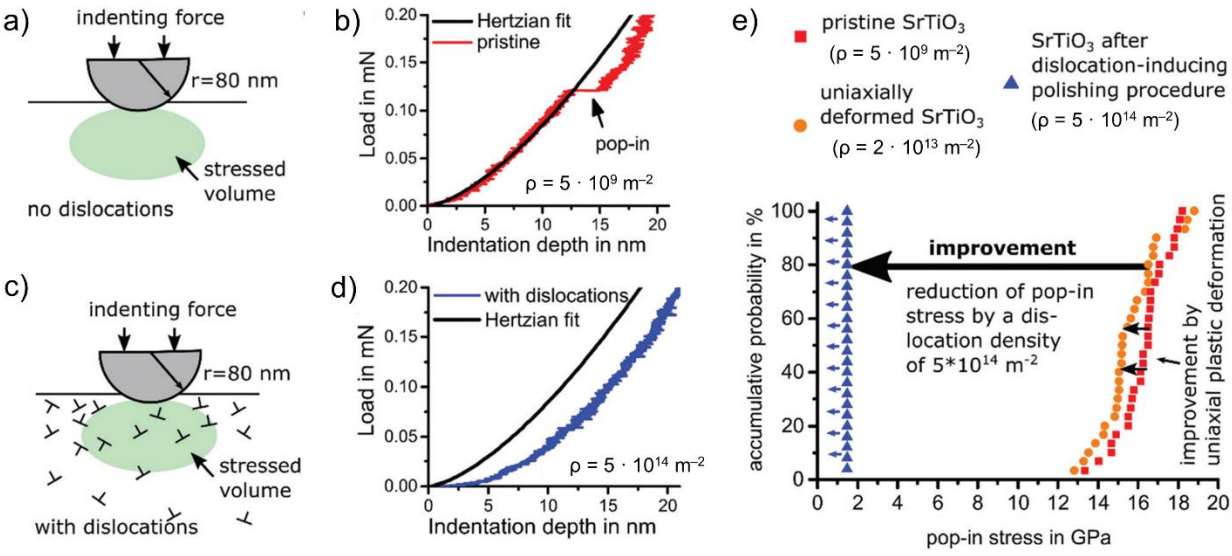

Figure 1.11: a) Schematic representation of the dislocation-free volume stress during indentation; b) Indentation curve in the initial stages of the pristine single crystal $SrTiO_3$ where the measured curve deviates from the Hertzian fit at the first pop-in; c) Schematic representation of the dislocation-rich volume stress during indentation; d) Indentation curve in the initial stages of the dislocation rich $SrTiO_3$; e) Comparison of τ_{max} measured in dislocation-free and dislocation-rich $SrTiO_3$ (from [15]).

Compared to non-ferroelectric perovskites, ferroelectrics can undergo anelastic and plastic deformation through reversible and irreversible non-180° DW ferroelastic motion, respectively. The onset of ferroelastic DW motion is triggered at forces lower than those required for dislocation nucleation in dislocation-free ferroelectrics. Indirect evidence of ferroelastic DW dynamics was obtained by analyzing the indentation curve in $BaTiO_3$, as shown in Figure 1.12a, where a small hysteresis appears before the first pop-in (Figure 1.12b). The small hysteresis observed in Figure 1.12a points to a mechanism that leads to remanence in deformation. The anomaly, which is atypical for purely elastic behavior where both parts of the curve overlay, is explained as domain reorientation and ferroelastic DW motion, which participate in the accommodation of the applied stress [62].

Direct evidence of domain reconfiguration has also been observed through in-situ nanoindentation experiments inside a TEM in PZT thin films [63], as shown in the image sequence in Figure 12c and the schematics in Figure 12d, as well in $BaTiO_3$ nanopillars [64].

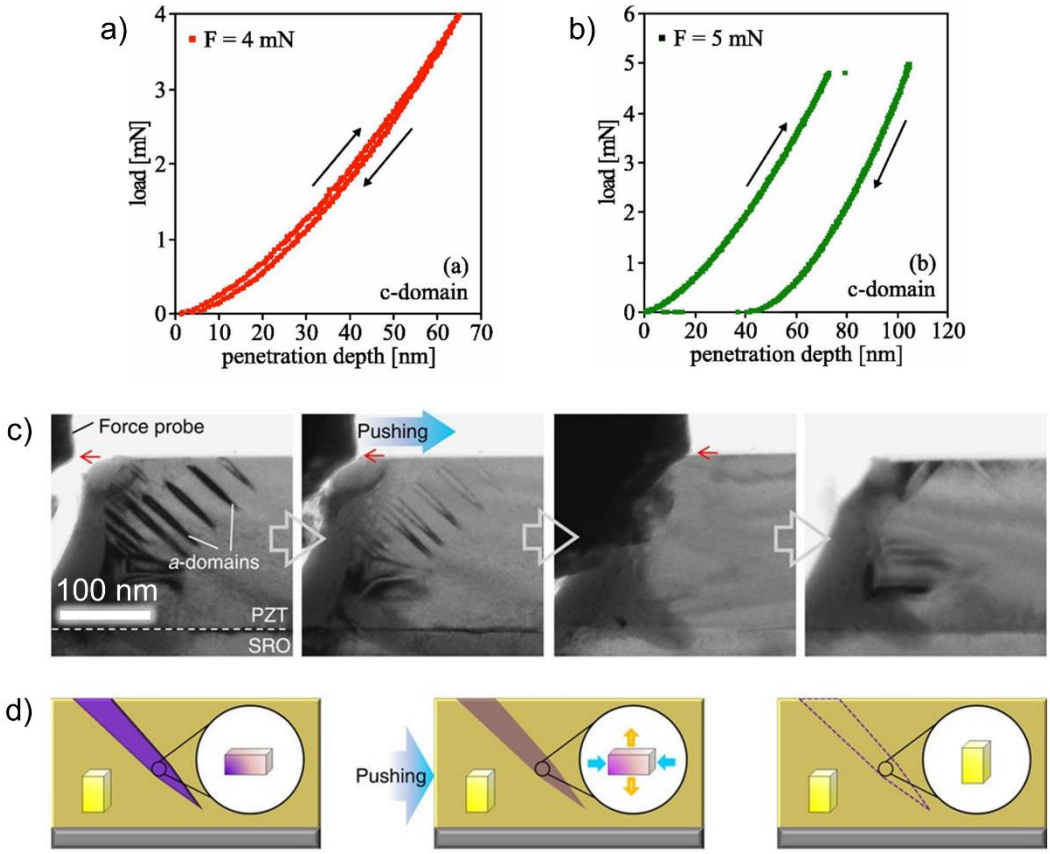

Figure 1.12: Indentation curves of $BaTiO_3$ a) before and b) after the first pop-in; c) sequence of TEM micrographs and d) schematic representations of ferroelastic switching in PZT during application of lateral force, Adapted after [62] and [64].

1.4.2 Atomic Force Microscopy Techniques Dedicated for Measuring Mechanical Properties

As discussed in Chapter 1.4.1.1, determining the elastic properties of thin films or nanoscale objects is challenging, even with nanoindentation. Instead, techniques based on atomic force microscopy (AFM) can be used for localized elasticity measurements, providing higher lateral resolution [65].

AFM is a subgroup of scanning probe microscopy where a sharp probe located at the end of a flexible cantilever scans the surface of the specimen line by line, bending the cantilever based on the topographical features of the sample surface. The deformation of the cantilever is detected by a laser that is reflected from the backside of the cantilever into a photodiode, producing a topography image on the computer screen. Scanning can be performed in several ways, i.e., contact mode, semi-contact mode, and non-contact mode [66].

Two AFM techniques that offer the ability to map local elastic properties are peak force quantitative nanomechanical mapping (PF-QNM) and contact resonance frequency mapping (CRFM). The former technique is based on indenting the surface to extract E from the resulting force-distance curves, while the latter calculates E based on the dynamic response of the mechanically excited tip-sample system, where changes in resonance frequency reflect variations in local elasticity.

1.4.2.1 Peak Force Quantitative Nanomechanical Mapping

PF-QNM is a commercial name for an AFM imaging technique where the cantilever oscillates at a frequency significantly lower than its resonance frequency, typically around 1−2 kHz, tapping the sample surface at a constant peak force of a few µN. At each imaging point, the AFM probe makes a brief contact with the sample surface, imprints it slightly (Figure 1.13a), and then retracts. This interaction is recorded as a force-distance curve, as illustrated in Figure 1.13b. From a single-point force-distance curve, the E_r is extracted by fitting the retraction portion of the curve using the Hertzian contact model (Figure 1.13, Equation 1.7).

To quantitatively determine E_r, the choice of AFM tip and cantilever is crucial. The AFM tip should be made of a material harder than the sample under investigation, ideally diamond, while the cantilever should be sufficiently stiff to avoid buckling or lateral rotation of the cantilever, as the Hertzian contact model does not account for cantilever deflections caused by shear forces [67].

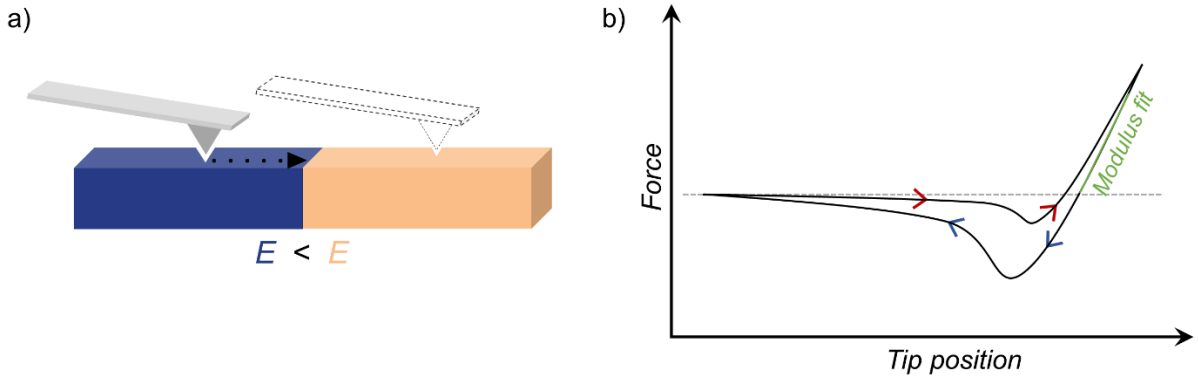

Figure 1.13: a) A schematic representation of the AFM tip making imprints in a sample with different local E. The black arrow marks the direction of scanning. b) A force-distance curve measured at each imaging point. Arrows mark the course of the curve. The portion of the curve used for the calculation of E_r is marked in green.

1.4.2.2 Contact Resonance Frequency Mapping

In CRFM, an image of local elastic priorities is constructed by following the contact resonance frequency of the mechanically exited tip-sample system. Mechanical excitation is introduced by mechanically exiting either the cantilever [68] or the sample holder [69] with a high-frequency actuator. Recent developments in AFM technology also enable the cantilever to be excited by photothermal actuation [70], where an additional laser is impinging on the cantilever, heating it with varying intensity and causing it to vibrate. A schematic of the experimental setup, where the cantilever is mechanically exited, is shown in Figure 1.14a.

The resonance frequency of the oscillating system is related to the elastic properties of the sample and may shift during scanning as the sample's elasticity locally changes. Shifts toward lower frequencies indicate a lower E of the material, and conversely, shifts to higher frequencies indicate a higher E (Figure 1.14b). The resonance frequency shifts are converted into E by modeling the elastic tip-sample interaction and the oscillation of the cantilever at the first or higher flexural resonance [71].

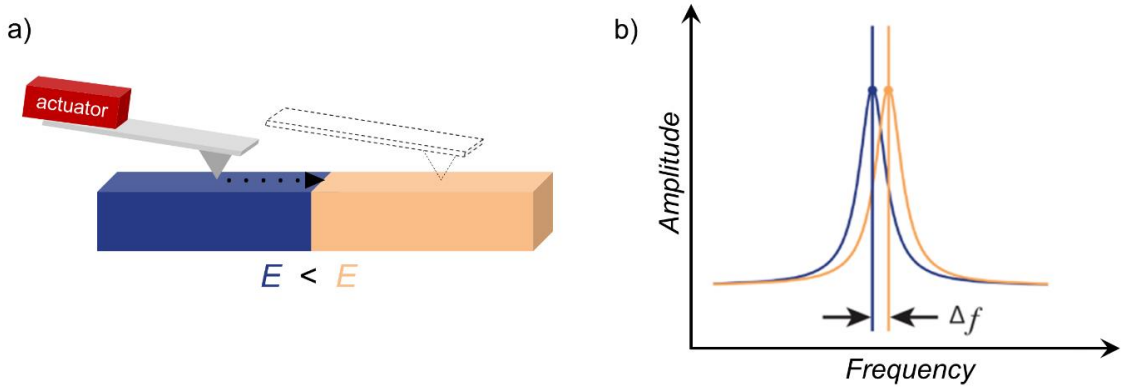

Figure 1.14: a) A schematic representation of the AFM cantilever mechanically exited by an actuator. The black arrow marks the direction of scanning. b) As the tip passes onto a region of higher E, the resonance frequency of the mechanically exited tip-sample system shifts towards higher frequencies. Adapted after [72].

Such techniques have proven to be indispensable in nanoscale studies of domains' elastic anisotropy [73] as well as the elastic properties of DWs. Experimental studies on elasticity measurements of DW are scarce in the literature, most relying on CRFM.

The different mechanical behavior of DWs was first reported in PZT ceramics [74]. The authors observed string-like features with lower contact resonance frequency within the material, which were confirmed to be DWs later using piezoresponse force microscopy (PFM). In a later work, combining cantilever vibration theory and Hertzian contact theory, the ratios of E of DWs and domains for 180° DW with different widths in PZT ceramics were determined to be 0.587 for a 2-nm wide DW and 0.826 for a 5-nm wide DW. At the time, the authors also presented three possible effects that could explain the observed phenomena: i) the atomic disorder of the crystal lattice at the DWs may reduce their stiffness; ii) the ability of DWs to switch and consequently move may reduce stiffness; and iii) the reduction in stiffness due to the reduced piezoelectric stiffening at the DW. Regarding the latter, in the AFM experiment on the domains, the polarization charge during the stress application cannot be compensated by the small contact area of the AFM probe, and the stiffness increases due to the depolarization field created. On the other hand, the average polarization at the DW is small, and the piezoelectric stiffening effect is weaker there than in domains [75].

Following the seminal work on PZT, 180° DWs that separate domains with out-of-plane P_s were investigated in a periodically poled $LiNbO_3$ single crystal, a $BaTiO_3$ single crystal, and a $PbTiO_3$ thin film using CRFM [19]. In all three cases, lower stiffness at the DWs was observed, indicating a universal phenomenon independent of the sample morphology and composition. In addition, the elastic softening was found to be independent of whether some domains were artificially created, as in $LiNbO_3$, or spontaneously formed via cooling across the Curie point, as in $BaTiO_3$. From the frequency shifts, considering the Hertzian contact theory and modeling the elastic interactions between the probe and the sample, E at the DWs of $BaTiO_3$ was calculated and found to be 51.5 GPa, which is 19 % less than the value of domains with out-of-plane P_s (63.6 GPa). A PFM image and CRFM image of the domain structure of the $BaTiO_3$ are shown in Figure 1.15a and Figure 1.15b, respectively. In both images, 180° DWs separating domains with out-of-plane P_s (c-c domains) appear as circular features, including in the CRFM image. However, 180° DWs that separate domains with in-plane P_s (a-a domains) exhibit no mechanical contrast [19].

This observation suggests that the absolute direction of P_s in the surrounding domains greatly influences the elastic properties of DWs.

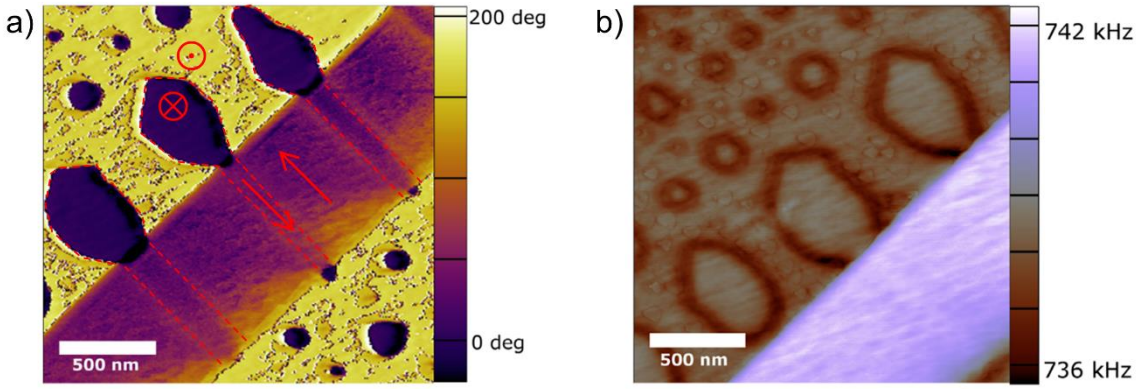

Figure 1.15: a) PFM phase image of $BaTiO_3$ single crystal; b) CRFM image of the roughly same area as shown in a). Dashed lines mark 180° DWs. ⊙ and ⊗ denote the out-of-plane direction of P_s, and arrows denote the in-plane direction of P_s, respectively (from [19]).

To determine the origins of the reduced stiffness of 180° DW in ferroelectrics, the three hypotheses proposed in the work on PZT were re-evaluated. First, the role of point defects was found to have a minor contribution [19] even though they act as elastic dipoles [76], generating local strain fields that can influence elasticity. Their effect may become significant in ferroelectrics where point defects are known to segregate at DWs, as found in $BiFeO_3$ [77].

The second hypothesis explored DW movement under AFM probe stress. Tensile stress in 180° domains creates reduced strain at DWs, forming a shallow surface depression. Probe interaction with the depression displaces the DW, which the AFM records as reduced stiffness [19]. As the DW movements can be restricted by defects present at the DW, the latter mechanism could be viewed as an indirect effect of defects' contribution to a softer elastic response of DWs.

Lastly, depolarization effects were analyzed. Stress from the AFM probe induces bound charges via inhomogeneous polarization, creating depolarizing fields that reduce stiffness. Two mechanisms of charge formation were identified: the "in-plane" mechanism, producing head-to-head or tail-to-tail patterns, and the "out-of-plane" mechanism, generating monopole- or dipole-like charges. The in-plane mechanism was found to be the main contributing factor, with DW softening increasing significantly with non-zero shear piezoelectric coefficients under open boundary conditions. While the out-of-plane polarization can be partially screened, the in-plane polarization consistently contributes to softening under AFM probe-induced fields [19].

The 90° DWs in $PbTiO_3$, exhibiting a ridge and valley topography as shown in Figure 1.16, were found to be elastically softer on one side of the domain (ridge topography) and harder on the other (valley topography). However, this effect was observed only in DWs separating domains with out-of-plane P_s on one side and in-plane P_s on the other (*a*-*c* DWs). The influence of topography on the measurement was refuted, with the alternating pattern instead attributed to differences in strain profiles at the DWs. The E of the elastically softer and harder DWs were measured at 43.5 ± 1.8 GPa and 60.7 ± 4.2 GPa, respectively, with the softening/hardening extending roughly 100 nm into the domains [20]. Molecular dynamics simulations also predicted an alternating elasticity pattern in 90° DWs with ridge and valley topographies, however, suggesting the opposite. The valley DWs should be softer than the ridges, with an elasticity variation of only ± 0.7 %. The authors further discussed the possibility that the measured elastic properties could be influenced

by artefacts from AFM, such as DW motion, which may either amplify or obscure the intrinsic elastic properties [78].

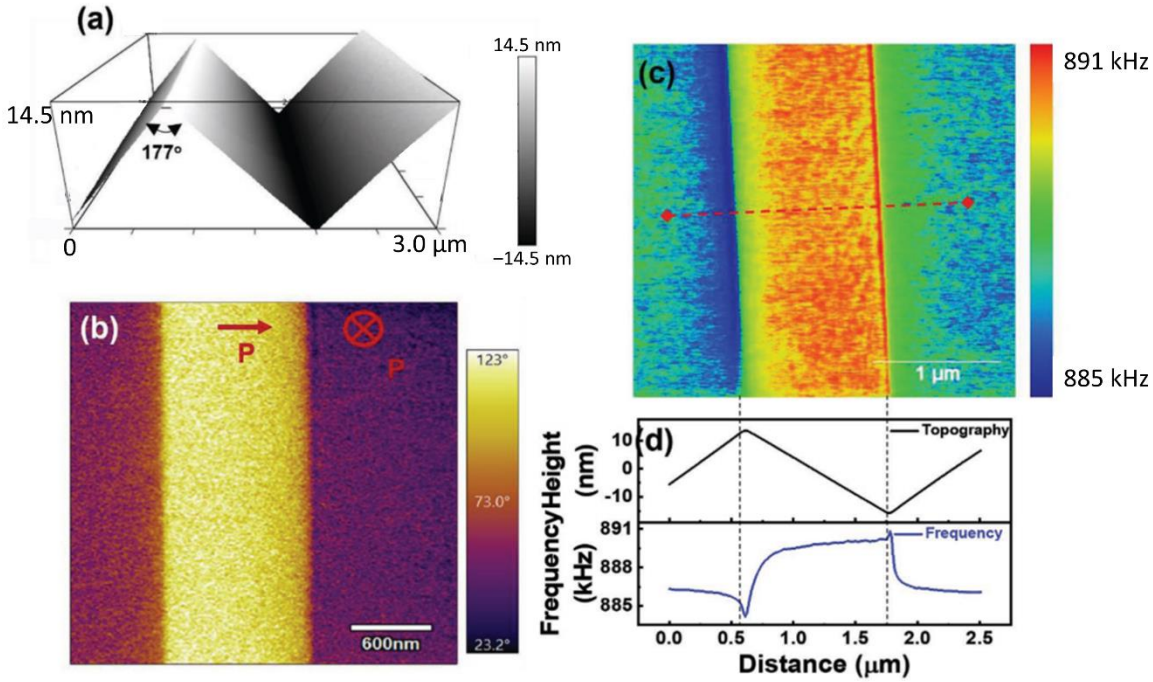

Figure 1.16: a) 3D topography of the *a*-*c* domains in $PbTiO_3$; b) Vertical PFM phase image of the same domain, showing the direction of P_s; c) CRFM image; d) Comparison of the line profiles of topography and frequency, taken from the region marked by the red dashed line in c) (from [20]).

Chapter 2

Aims and Hypothesis

The dissertation aims to investigate the local elastic and plastic properties of perovskite oxide ferroelectric materials, which are notable from an environmental perspective due to their energy-efficient preparation, such as aerosol-deposited thick films, or their environmentally friendly lead-free compositions. Thus, the first part of the dissertation focuses on understanding the local mechanical properties of films prepared using aerosol deposition, while the second part focuses on the local mechanical properties of two lead-free bulk ferroelectrics, namely bismuth ferrite and potassium sodium niobate.

The aims of the three parts of the dissertation are the following:

1) To determine the changes of Young's modulus and hardness using nanoindentation of aerosol-deposited $0.9Pb(Mg_{1/3}Nb_{2/3})O_3{-}0.1PbTiO_3$ thick films that occur during heat treatment at 500 °C, which is common practice to improve the functional properties of aerosol-deposited films. This part, therefore, aims to thoroughly investigate the structure and microstructure before and after the heat treatment using electron microscopy in order to correlate them with the local mechanical properties.
2) To measure Young's modulus and hardness of $BiFeO_3$ ceramics via nanoindentation as well as to investigate structural and microstructural defects resulting from the plastic deformation down to the atomic level.
3) To investigate the local changes in elasticity of the ferroelectric domain structure of $(K_{0.5}Na_{0.5})NbO_3$ single crystal by atomic force microscopy-based techniques and understand them with the help of finite element modeling.

The hypotheses of the dissertation are:

1) Structure and microstructure have an impact on Young's modulus and hardness. More so on Young's modulus due to the different sizes of elastic and plastic zones under the indentation probe. In the case of a layered material, the Young's modulus measured on the film is also affected by the elastic properties of the substrate. While for polycrystalline materials prepared by high-temperature annealing, hardness measurements are affected by the indentation size effect.
2) The microstructure affects the mechanism of plastic deformation, which will thus differ in bulk materials prepared by high-temperature annealing and aerosol-deposited films.
3) Bulk materials have a low dislocation density prior to mechanical deformation and deform through dislocation-mediated plasticity under mechanical loading.
4) The resolution of nanoindentation does not allow us to detect changes in the elasticity of domains and domain walls. Only by employing techniques with higher

lateral resolution, such as atomic force microscopy-based techniques, can the local elastic properties be determined.

5) Ferroelectric domains show anisotropic elastic behavior, which will be dependent on the direction of the spontaneous polarization.
6) Domain walls either have different elastic or the same elastic properties as neighboring domains.

Chapter 3

Influence of Thermal Treatment on the Cross-Sectional Properties of Aerosol-Deposited $Pb(Mg_{1/3}Nb_{2/3})O_3$—$PbTiO_3$ Thick Films

The present study focuses on the correlation of the microstructural changes induced by post-deposition annealing with the E and H values measured by nanoindentation across the cross-section of aerosol-deposited $0.9Pb(Mg_{1/3}Nb_{2/3})O_3$—$0.1PbTiO_3$ thick films on stainless steel substrates.

Post-deposition annealing is commonly performed to improve the dielectric, ferroelectric, and energy storage properties of aerosol-deposited films [11], [79]–[82]. We found that heating at 500 °C for 1 hour induces small but detectable structural and microstructural changes in the films. Annealing improves crystallinity, promotes grain growth, and redistributes the pores into chain-like defects, resulting in a less homogeneous microstructure. In addition, annealing causes oxidation at the interface between the film and the substrate, forming a multilayered structure with Fe-rich, Ni-rich, Cr_xO_y, and Fe_mO_n layers, each approximately 30–40 nm thick.

These structural and microstructural changes cause both E and H to increase after annealing. Furthermore, the force-displacement curves show a broader distribution after annealing due to the microstructural inhomogeneities introduced during the process. While H remains relatively constant over the entire film thickness, E decreases as the measurements are made further from the substrate due to the influence of the underlying stainless steel. The contribution of the multilayer oxide structure to the overall properties is estimated to be minor.

Interestingly, no cracking was observed around the indentations at the applied force of 1 mN, suggesting that the deformation mechanism is primarily governed by grain boundary sliding [11] rather than dislocation-mediated plasticity, which is typically accompanied by cracking.

This chapter addresses objective 1 and hypotheses 1 and 2.

Published in: K. Žiberna, M. Šadl, A. Drnovšek, G. Dražić, H. Uršič and A. Benčan, "Influence of Thermal Treatment on the Cross-Sectional Properties of Aerosol-Deposited $Pb(Mg_{1/3}Nb_{2/3})O_3$–$PbTiO_3$ Thick Films", *Crystals*, **13**, 536, 2023, https://doi.org/10.3390/cryst13030536.

My contribution: I metallographically prepared the cross-sectional surface of the films, performed *in-situ* nanoindentation, analyzed the nanoindentation data, and performed postmortem SEM analysis. I prepared electron-transparent samples with the focused ion beam (FIB) and performed STEM analysis in conjunction with EDS. Together with the co-authors, we interpreted the data, developed the manuscript concept, and wrote the paper.

crystals

MDPI

Article

Influence of Thermal Treatment on the Cross-Sectional Properties of Aerosol-Deposited $Pb(Mg_{1/3}Nb_{2/3})O_3-PbTiO_3$ Thick Films

Katarina Žiberna [1,2,*], Matej Šadl [1,2], Aljaž Drnovšek [3], Goran Dražić [1,2,4], Hana Uršič [1,2] and Andreja Benčan [1,2]

[1] Electronic Ceramics Department, Jožef Stefan Institute, Jamova Cesta 39, 1000 Ljubljana, Slovenia; matej.sadl@ijs.si (M.Š.); goran.drazic@ki.si (G.D.); hana.ursic@ijs.si (H.U.); andreja.bencan@ijs.si (A.B.)
[2] Jožef Stefan International Postgraduate School, Jamova Cesta 39, 1000 Ljubljana, Slovenia
[3] Department of Thin Films and Surfaces, Jožef Stefan Institute, Jamova Cesta 39, 1000 Ljubljana, Slovenia; aljaz.drnovsek@ijs.si
[4] Department of Materials Chemistry, National Institute of Chemistry, Hajdrihova 19, 1000 Ljubljana, Slovenia
* Correspondence: katarina.ziberna@ijs.si

Abstract: The thermal treatment of electromechanically active thick films prepared by aerosol deposition (AD) is a common practice to improve their electrical and electromechanical properties. We report on how post-deposition annealing in air affects the unique cross-sectional microstructure and mechanical properties of $0.9Pb(Mg_{1/3}Nb_{2/3})O_3-0.1PbTiO_3$ thick films prepared by AD. Transmission electron microscopy revealed minor but detectable changes, such as pore redistribution and grain growth after annealing at 500 °C. We also showed that the stainless-steel substrate is strongly affected by the annealing. The hardness and Young's modulus of the films increased after annealing, with both properties being discussed in terms of their distribution over the cross-sections of the films.

Keywords: aerosol deposition; thick films; microstructure; mechanical properties

Citation: Žiberna, K.; Šadl, M.; Drnovšek, A.; Dražić, G.; Uršič, H.; Benčan, A. Influence of Thermal Treatment on the Cross-Sectional Properties of Aerosol-Deposited $Pb(Mg_{1/3}Nb_{2/3})O_3-PbTiO_3$ Thick Films. *Crystals* **2023**, *13*, 536. https://doi.org/10.3390/cryst13030536

Academic Editor: Pavel Lukáč

Received: 22 February 2023
Revised: 17 March 2023
Accepted: 18 March 2023
Published: 21 March 2023

1. Introduction

Aerosol deposition (AD) is a method that enables the fabrication of high-density polycrystalline films at room temperature. The method was successfully used for preparing films for various applications, such as ferroelectric films for sensors and actuators, protective coatings, oxide ion-conductor layers in solid-oxide fuel cells, catalytic and superconductor layers [1,2]. The AD apparatus sprays submicron particles onto the substrate with high kinetic energy, and the film grows by impact consolidation and fracture of the initial powder particles [1,3,4]. Since the AD takes place at room temperature, a wide range of materials can be used as substrates, from metals with a low melting temperature [5–13] to ceramics [8,14,15], glass [8], and even polymers [16].

In some cases, a heat treatment is still required after the deposition to achieve the intended functionalities of the film. For example, additional annealing is essential for electromechanical films to improve dielectric, ferroelectric, and energy-storage properties [10–12,17–19]. The enhancement is thought to be related to the partial release of the residual stresses created in the films during deposition by the high-energy impacts [9,10,17,20]. For example, Khansur et al. reported a compressive stress in a $BaTiO_3$ film, measured by X-ray microdiffraction, that is not uniformly distributed across the film thickness. The peak stress of −800 MPa was measured near the film-substrate interface, and a significant decrease towards the surface was observed. Heat treatment at 500 °C reduced the total stress to −271 MPa, but the relaxation near the surface persisted [21]. At the same time, the annealing also affects the mechanical properties of these films. An increase in the hardness (H) and the Young's modulus (E) as well as a degradation in the plastic deformability and thus the crack resistance was observed after annealing [12,17], suggesting that an optimization

of the annealing temperature is required to achieve both the best electromechanical and mechanical properties of the AD films.

Studies of the mechanical properties of functional AD polycrystalline films are rare [7,12], mostly due to the experimental challenges related to the size of the film. The thickness of the film (up to few tens of μm) limits the application of most mechanical tests, leaving only the possibility of performing micro- and nano-mechanical tests, e.g., nanoindentation.

Here, we investigated the effects of heat treatment in air atmosphere on the cross-sectional mechanical properties of AD thick films using in-situ nanoindentation to gain a better understanding of the overall functional response of the films. The materials studied were aerosol-deposited $0.9Pb(Mg_{1/3}Nb_{2/3})O_3-0.1PbTiO_3$ (PMN−10PT) thick films on stainless steel, which showed a significant reduction in microstrains and an improvement in the energy-recovery density and energy-storage efficiency after heat treatment at 500 °C [10], but their mechanical behavior has not yet been investigated. In addition, we investigated the effects of heat treatment on the microstructure and composition throughout the film thickness, down to the nm range. We showed that the formation of nanopore-chain-like defects and grain growth are triggered when the film is annealed at 500 °C. The stresses created in the substrate by the impact of the powder particles during the deposition disappear after annealing, while the substrate oxidizes at the film-substrate interface. Although the microstructural changes appear to be minor, a non-negligible increase in the average H and E values was measured in the heat-treated film, with no cracking observed.

2. Materials and Methods

The $0.9Pb(Mg_{1/3}Nb_{2/3})O_3-0.1PbTiO_3$ (PMN−10PT) ceramic powder was synthesized by separately preparing the two end oxides from the initial powders, i.e., PbO (99.9%, Aldrich, St. Louis, MO, USA), MgO (99.95%, Alfa Aesar, Haverhill, MA, USA), TiO_2 (99.8%, Alfa Aesar, Haverhill, MA, USA) and Nb_2O_5 (99.9%, Aldrich, St. Louis, MO, USA). The prepared oxides, i.e., $Pb(Mg_{1/3}Nb_{2/3})O_3$ and $PbTiO_3$, were then mixed in the stoichiometric ratio and high-energy milled. Details of the procedure can be found elsewhere [10]. The high-energy-milled PMN−10PT powder was annealed at 900 °C for 1 h and then milled for 30 min with isopropanol using yttria-stabilized-zirconia milling balls with diameters of 3 mm at 200 min^{-1} to achieve the desired particle size and particle size distribution. Lastly, the powder was dried in a vacuum drier (10 mbar) at 100 °C for 12 h and sieved.

The substrate on which the film was deposited was a 15 mm × 15 mm stainless steel No. 304 (American Iron and Steel Institute, Washington, DC, USA) with a 0.8-mm thickness and a bright, polished surface (A480: No. 8, American Society for Testing and Materials, West Conshohocken, PA, USA). Prior to deposition, the stainless-steel substrates were cleaned with ethanol. The AD equipment was from InVerTec (Bayreuth, Germany). The deposition parameters are reported elsewhere [22].

Two films were prepared using the described procedure. One did not receive any further processing and is denoted in the text as as-deposited. The other film underwent a further heat treatment in air at 500 °C for 1 h with a heating and cooling rate of 2 K min^{-1} and is denoted in the text as annealed.

Scanning transmission electron microscopy (STEM) and transmission electron microscopy (TEM) were performed using a JEM 2100 (Jeol, Tokyo, Japan) and an ARM 200CF (Jeol, Tokyo, Japan) equipped with a Centurio 100-mm^2 SDD energy-dispersive X-ray spectroscopy system (EDS, Jeol, Tokyo, Japan), both operated at 200 kV. The 4D STEM data was obtained using a Merlin pixelated detector (Quantum Detectors, Oxford, UK). Samples for STEM/TEM were prepared by milling lamellae with a Ga^+-source focused ion beam (FIB) Helios Nanolab 650 HP (Thermo Fischer Scientific, Waltham, MA, USA). The volume percentage of defects in the FIB-prepared lamellae was estimated using Image J software (National Institute of Mental Health, Bethesda, MD, USA) [23].

The surface roughness was measured with a DektakXT Advanced System profilometer (Bruker, Billerica, MA, USA). Four line measurements of 2 mm each were performed on each sample and then averaged.

In-situ nanoindentation was performed with a Hysitron PI88 SEM PicoIndenter indentation system (Bruker, Billerica, MA, USA) inside a Quanta 650 ESEM (Thermo Fischer Scientific, Waltham, MA, USA). A force of 1 mN was applied over 5 s, held for 2 s and then released over 5 s. The hardness (H) and Young's modulus (E) of the films were determined using the methodology developed by Oliver and Pharr [24]. The Poisson's ratio (ν) used for the calculation of E was 0.3. This selection was made with the assumption that the ceramic PMN−10PT thick film had the same Poisson's ratio as the PMN ceramic [25]. A cube-corner diamond indentation probe with a nominal E = 1140 GPa and ν = 0.07 was used for indenting (Bruker, Billerica, MA, USA). The cross-sections of the two films on which the nanoindentation was performed were prepared by embedding the films in epoxy resin, grinding, and then polishing them with 9-µm, 6-µm, 3-µm, and $\frac{1}{4}$-µm diamond pastes. Fine polishing was achieved by polishing with a colloidal silica suspension for 15 h.

Scanning electron microscopy (SEM) after the nanoindentation was performed using a field-emission SEM Verios 4G HP (Thermo Fischer Scientific, Waltham, MA, USA) equipped with an EDS detector Aztec live, Ultim Max SSD 65 mm^2 from (Oxford Instruments, Abingdon, UK). Both imaging and EDS acquisition were performed at 15 keV. To avoid charging during the SEM analysis, the cross-sections of the films were coated with 5 nm of carbon using a Precise Etching and Coating System 628A (Gatan, Pleasanton, CA, USA).

Contact resonance frequency viscoelastic mappings (CRFMs) were made with a Jupiter XR atomic force microscope (Oxford Instruments Asylum Research, Santa Barbara, CA, USA) using AC160TS-R3 silicon tips with a nominal radius of 7 nm (Oxford Instruments Asylum Research, Santa Barbara, CA, USA).

3. Results and Discussion

3.1. Microstructure and Chemical Composition

First, we performed microstructural and compositional analyses of the cross-sections of both the as-deposited and the annealed ~6-µm-thick $0.9Pb(Mg_{1/3}Nb_{2/3})O_3-0.1PbTiO_3$ (PMN−10PT) films using scanning transmission electron microscopy (STEM). According to the X-ray diffraction (XRD) analysis, these films have a perovskite crystal structure (Figure S1) [10]. As shown in Figure 1 and Figure S2 (see Supplementary materials) both films have defects, i.e., some larger pores of 200 nm (marked by arrows in Figure 1a,c) and chain-like defects consisting of nanopores (marked by circles in Figure 1a,c). The volume percentage of defects is higher in the annealed film (1.1 vs. 0.6 %), indicating that the pores redistribute, and areas of lower local density are formed as the film is annealed. The roughness of the surface does not change significantly with annealing. The root-mean-square surface roughness of the as-deposited and the annealed films are (110 ± 10) nm and (105 ± 5) nm, respectively.

Energy-dispersive X-ray spectroscopy (EDS) mappings revealed a homogeneous distribution of all the elements across the cross-sections (Figure S3), with the exception of Mg (Figure 1b,d). Mg-rich nanosized impurities were found in both films. Similar inhomogeneities were observed in mechanochemically prepared PMN−10PT ceramics and identified as MgO, which due to its low reactivity remained unreacted during the mechanochemical reaction [26].

Next, we examined the region of the film near the substrate. Figure 2 shows the film-substrate interface (Figure 2a,c) and the elemental distribution of the main elements in the stainless-steel substrate, i.e., Fe, Cr, and Ni, at the film-substrate interface (Figure 2b,d) of the as-deposited film and the annealed film, respectively. As described above, the number of defects, i.e., nanoscale pores, is higher in the annealed film. In the as-deposited film we observed some brighter contrast at the interface (Figure 2a) extending about 500 nm into the substrate, indicating mechanical deformation of the substrate caused by the impact of the powder during deposition. Stresses in the substrate of the as-deposited film were also observed from the divergence map obtained from the 4D STEM data set

using differential phase contrast (Figure S4) that additionally revealed stresses of a higher magnitude localized at the film-substrate interface and around the defects in the film itself. According to the XRD studies, the internal stresses caused by particle impacts during the AD process on stainless-steel substrates are tensile stresses [8]. Stainless steel (hardness (*H*) of stainless steel No. 304 ~1.9 GPa [27]) is more susceptible to mechanical deformation than substrates with a higher *H*. For example, for $Pb(Zr_{0.52}Ti_{0.48})O_3$ deposited on Si, a 100−150-nm-layer damaged layer was reported for the substrate [6] (*H* of Si ~11.1 GPa [28]). The contrast caused by mechanical stresses is not seen in the substrate of the annealed film (Figure 2c), indicating that the stresses are relieved in the substrate during annealing.

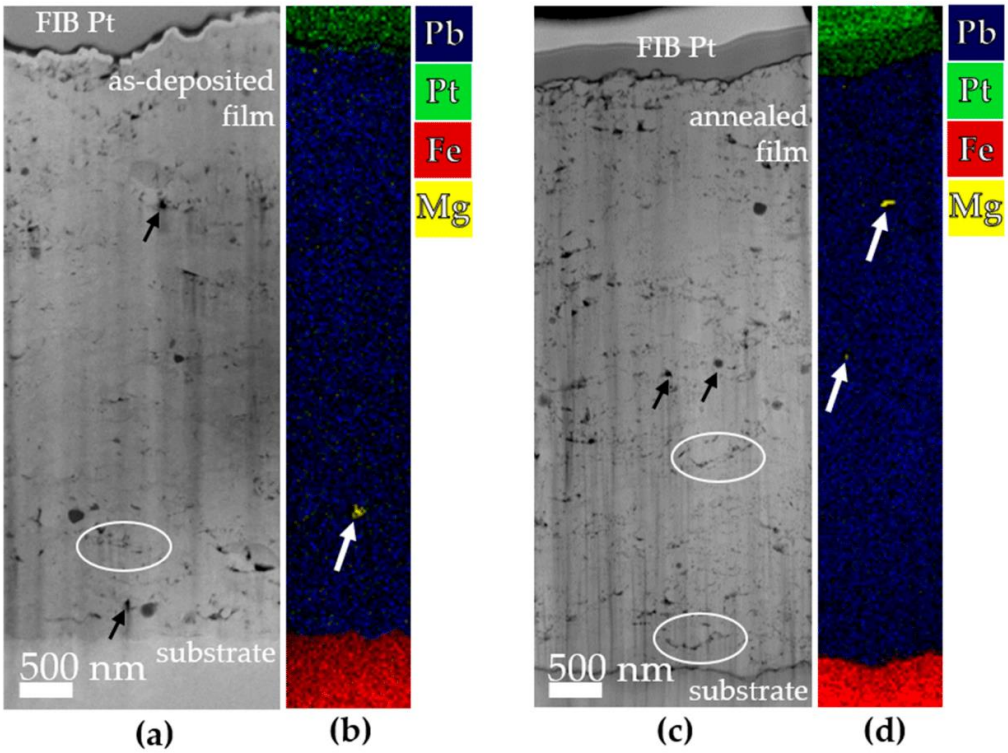

Figure 1. STEM dark-field and EDS analyses, respectively, of the (**a**,**b**) the as-deposited film and (**c**,**d**) the annealed PMN−10PT thick film. The black arrows on the STEM images (**a**,**c**) indicate larger pores in the films, while the circles mark the chain-like defects composed of nanopores. White arrows in the EDS mapping (**b**,**d**) mark Mg-rich inclusions in the films. Spectral lines Pb L, Pt M, Fe K, and Mg K were used for the EDS mapping.

In addition, a redistribution of the elements in the substrate occurs at the interface between the film and the substrate (Figure 2b,d). EDS showed that a layered structure is formed at the interface, which consists (from the substrate matrix to the film) of an Fe-rich and a Ni-rich layer, a Cr_xO_y layer, and an Fe_mO_n layer (Figure S5). Each layer is approximately 30−40-nm thick. Apart from the formation of the oxide layers, no reaction with the film was observed in the annealed sample. It is described in the literature that the passivation of stainless steel in air occurs at 300 °C due to the diffusivity of oxygen from the atmosphere into the substrate and metal ions towards the surface, forming a specific sequence of layers associated with the formation energies of Fe_mO_n, Cr_xO_y and NiO [29]. The source of oxygen forming the oxides in the substrate in our case has not been determined. However, there are some studies that support the claim that oxygen can diffuse through the film during annealing. Eckstein et al. argued that films deposited in an

oxygen-depleted carrier gas such as N_2, as used in this work, contain oxygen vacancies created during deposition that can serve as pathways for the oxygen, which presumably fills the vacancies during annealing in an oxygen-rich environment [13]. Another oxygen pathway through could be the grain boundaries, which have been reported to have a higher oxygen diffusivity than the grain matrix in nanocrystalline films [30]. The diffusion of oxygen might also be related to the redistribution of defects during annealing (Figure 1).

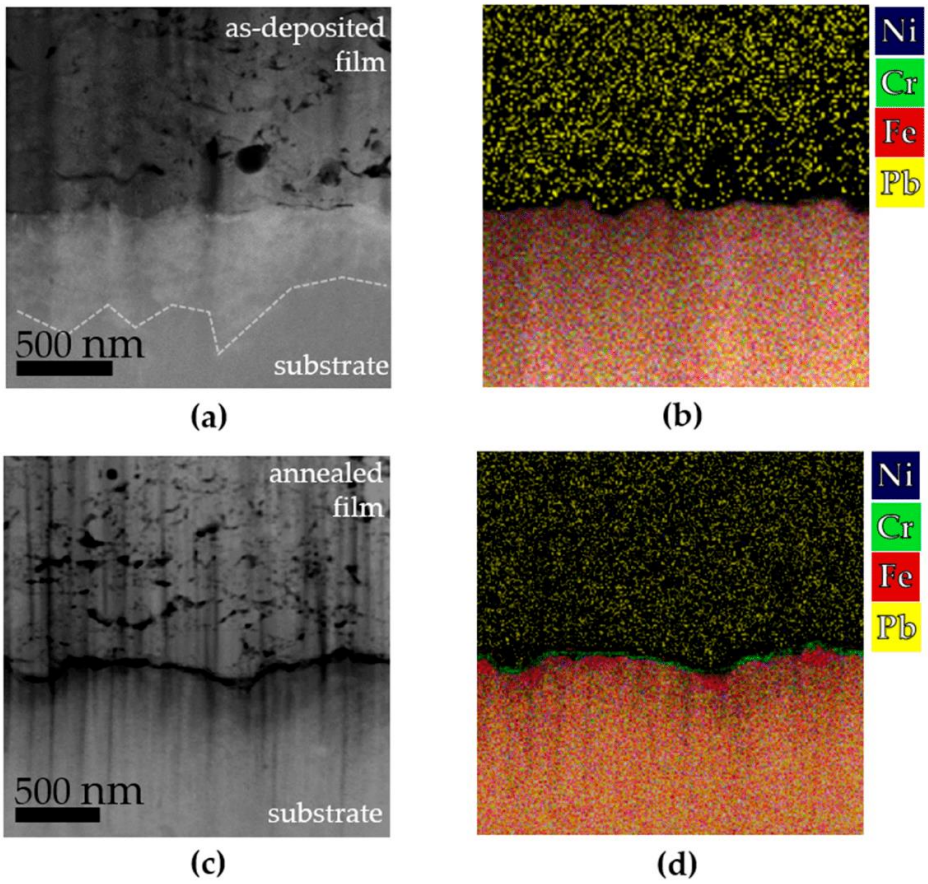

Figure 2. Film-substrate interface in STEM dark-field images and EDS, respectively, of (**a**,**b**) the as-deposited film and (**c**,**d**) the annealed film. In (**a**) the dashed line marks the extent of the mechanical deformation observed in the substrate due to particle impact. For the EDS mappings, the spectral lines Ni K, Cr K, Fe K and Pb L were used.

The influence of annealing on the grain size is shown in Figure 3. The as-deposited film consists of ~10 nm grains (Figure 3a), but the exact grain size is difficult to determine because the grains overlap. Annealing at 500 °C triggered grain growth (Figure 3b), with some grains growing up to about ~20 nm. The increase in grain size and crystallinity can also be observed from selected-area electron diffraction (SAED) recorded from larger areas of the FIB lamellae (Figure 3c), where more pronounced spots in diffraction rings are observed after annealing. The increase in grain size and better crystallinity after annealing affect the local stresses observed by XRD [10] and can contribute to improved electrical and electromechanical as well as mechanical properties of the heat-treated films.

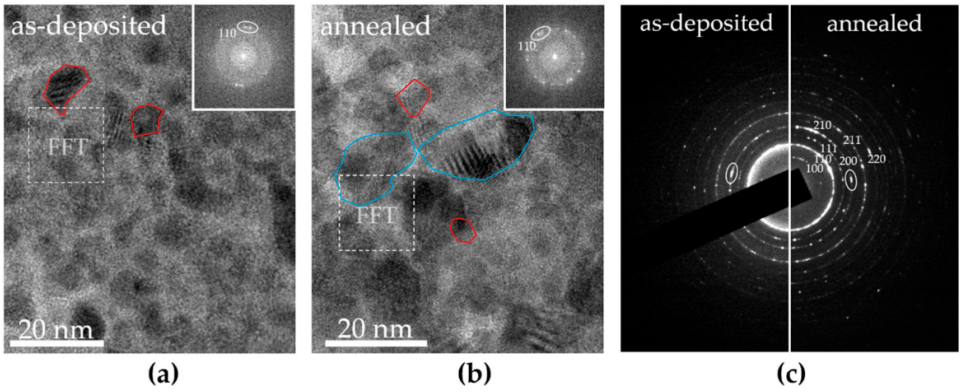

Figure 3. Transmission electron microscopy (TEM) images of grains in: (**a**) the as-deposited film with the FFT inset of the marked region; and (**b**) the annealed film (larger and smaller grains are circled in blue and red, respectively), with an inset of the FFT from the marked region. (**c**) Comparison of the SAED of both films. Circles mark reflections that are indicative of texturing. The $Pm\bar{3}m$ space group was used to index the SAED pattern (PDF#01-074-4513).

The proximity of the reflections in the SAED (some examples are circled in Figure 3c) indicates that the film has some texture. A fast Fourier transform (FFT) of selected regions in Figure 3a,b showed that the texture is very local and probably includes few neighboring grains. The local texturing is a result of deposition causing the larger particles to break upon impact. On a TiO_2 nanoparticle model system, Daneshian et al. predicted, using molecular dynamics, that a particle deposited by AD will fragment after impact and the fragmented parts will form low-angle grain boundaries [31]. Other authors also reported a reorientation of the crystallites during annealing at 500 °C in $BaTiO_3$ [12], which was not observed in our case, at least not to affect and thus reduce the local texturing after annealing.

3.2. Mechanical Behavior

Finally, the mechanical properties of the films were investigated by nanoindentation over cross-sections. A matrix of nanoindentations was made for each film, as shown in Figure 4a,b. At an applied load of 1 mN, both films exhibited good ductility as no cracks were observed around the indentations in either film. Zhuo et al. showed for $BaTiO_3$ that a threshold load of 200 g (~2 N) is required to see the difference in the crack resistance between the as-deposited and annealed films, with the as-deposited films performing better and not forming cracks around the indentations [12]. The crack resistance of the films, which is not characteristic of conventionally sintered ceramics [32], is probably related to the high density of the grain boundaries, which makes it easy for the grains to slide against each other during indentation, as well as to other defects in the films, such as dislocations [13].

The differences in the mechanical properties of the films can be seen from the force-depth curves in Figure 4c,d. The curves of the as-deposited film (Figure 4c) are more uniform, while the curves of the annealed film show a larger scatter and many pop-ins (sudden jumps of the measured depth at a constant force) are observed in the loading portions of the curves. The difference can be attributed to the change in microstructural properties, i.e., redistribution of the pores (Figure 1) and grain growth (Figure 3) observed after annealing. The overall increase in H and Young's modulus (E) of the AD films after annealing from (5.9 ± 0.3) GPa to (6.8 ± 0.6) GPa and from (107.6 ± 7.7) GPa to (125.5 ± 9.3) GPa, respectively, is in the literature associated with relaxation of residual stresses [12,17]. The increase in the standard deviation of H and E also reflects the changes in the microstructure caused by the heat treatment.

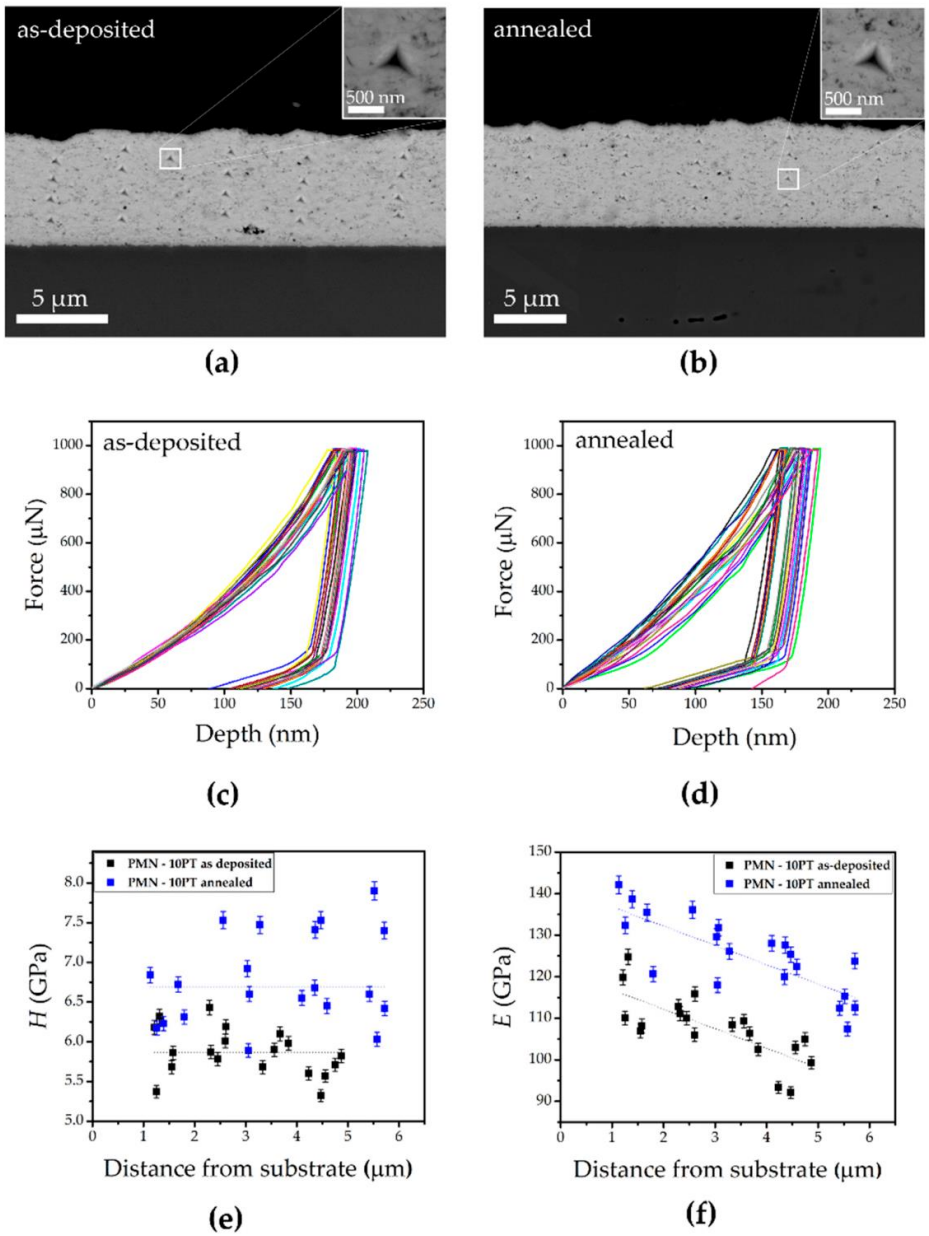

Figure 4. SEM images of indents made on cross-sections of (**a**) the as-deposited and (**b**) annealed film. Force-depth curves of (**c**) the as-deposited and (**d**) annealed film. (**e**) Hardness calculated from individual measurements plotted against indentation position for both films. (**f**) Young's modulus calculated from individual measurements, plotted against the position of the indentation for both films. The error bars represent the uncertainty of the method as determined from measurements on the fused-silica standard. The dashed lines serve only as a guide to the eyes.

In Figure 4e,f the calculated values of H and E, respectively, from the individual indentations are plotted as a function of position relative to the film-substrate interface. H (Figure 4e) shows no specific trend across the film thickness and no influence of the substrate on the measurement was observed (H of stainless steel No. 304 ~1.9 GPa [27]). The same cannot be said for E (Figure 4f). For both films, E decreases linearly as the surface is approached, which is a consequence of the elastic properties of the substrate being measured with those of the film. The E of the substrate is higher than that of the film, as confirmed by the contact resonance frequency maps, (Figure S6) (E of stainless steel No. 304 ~200 GPa [27]). The influence of the substrate is strongest near the film-substrate interface, so a higher E is measured, and appears to have a significant range of at least 5 µm. Measuring E by nanoindentation across the cross-section of films can be challenging due to the large elastic zone that is deformed under the indentation probe [33]. The oxides that form at the interface between the film and the substrate are likely to contribute little to the total E measured.

4. Conclusions

The microstructure of $0.9Pb(Mg_{1/3}Nb_{2/3})O_3-0.1PbTiO_3$ thick films deposited on stainless steel by aerosol deposition (AD) was studied before and after annealing in air at 500 °C to determine the changes in the unique microstructure created by the AD process. The changes appear to be small, but detectable, such as the redistribution of pores into chain-like defects consisting of nanopores and grain growth after heat treatment. Local texturing at the level of a few adjacent grains was also observed in both films. Interestingly, annealing affects the substrate as well by relieving stresses caused by the impact of particles during the AD process and the oxidation of the substrate at the film-substrate interface.

While annealing induced microstructural changes at the nanoscale, the mechanical properties, i.e., the hardness and Young's modulus, were significantly affected, as evidenced by the increase in both values after annealing. Both films resisted cracking at a force of 1 mN, which is not observed in conventionally produced ceramics, and is a consequence of the unique microstructure of the densely packed nanograins produced by the AD method.

Supplementary Materials: The following supporting information can be downloaded at: https://www.mdpi.com/article/10.3390/cryst13030536/s1, Figure S1: X-ray diffraction patterns of the as deposited and the annealed film. All peaks were indexed with a cubic perovskite structure (space group $Pm\bar{3}m$, JCPDS 81-0861) Figure S2: Scanning transmission electron microscopy (STEM) (a) dark-field and (b) bright-field images of the as-deposited film; (c) the dark-field and (d) bright-field images of the annealed film. Note that the black and white arrows point to pores locations, which are black in dark field and white in bright field. The vertical lines observed on the STEM images are a consequence of the focused ion beam curtain effect; Figure S3: Compositional analysis of the as deposited and the annealed film, respectively, performed using (a) and (b) EDS-STEM and (c) and (d) EDS-SEM with the corresponding EDS line analysis. The white arrows in (a) and (b) indicate the Mg-rich inclusions; Figure S4: (a) STEM dark-field image of the film-substrate interface in the as-deposited film; (b) the corresponding divergence map obtained from the 4D STEM dataset using differential phase contrast. Areas with higher contrast in the divergence map represent higher local strain; Figure S5: EDS of the film-substrate interface of the annealed PMN−10PT thick film resolving a layered structure formed due to oxidation of the substrate at 500 °C. The layer structure is composed (from substrate to film) of an Fe- and Ni-rich layer, a Cr_xO_y layer and an Fe_mO_n layer; Figure S6: (a) Topography and (b) frequency mapping at the film-substrate interface of the as-deposited film measured in the contact resonance frequency viscoelastic mapping mode. This is an atomic force microscopy technique in which the frequency measured is the resonant frequency of the tip-material system and is related to the Young's modulus of the material. The higher the frequency, the higher the Young's modulus and vice versa. In b, a higher frequency is measured in the substrate than in the film, which means that the substrate has a higher Young's modulus than the film.

Author Contributions: K.Ž. and A.B. designed the experiments. M.Š. and H.U. prepared the thick-film samples. K.Ž. and A.D. performed the in-situ nanoindentation. K.Ž. performed the SEM analysis and CRFM measurements. K.Ž., A.B. and G.D. performed the TEM analysis. K.Ž. and A.B. wrote the manuscript. All authors revised and edited the manuscript. A.B. supervised the project. All authors have read and agreed to the published version of the manuscript.

Funding: This work is funded by the Slovenian Research Agency in the frame of national postgraduate funding (K. Ž.), core funding P2-0105 and projects J7-4637, J2-3041, J2-3058, J2-2497 and I0-0005.

Data Availability Statement: Not applicable.

Acknowledgments: Jena Cilenšek is acknowledged for her help in preparing the samples for nanoindentation. Val Fišinger is acknowledged for helping with atomic force microscopy. JSI Director's fund 2017-ULTRACOOL project is also acknowledged.

Conflicts of Interest: The authors declare no conflict of interest.

References

1. Hanft, D.; Exner, J.; Schubert, M.; Stöcker, T.; Fuierer, P.; Moos, R. An Overview of the Aerosol Deposition Method: Process Fundamentals and New Trends in Materials Applications. *J. Ceram. Sci. Technol.* **2015**, *6*, 147–181. [CrossRef]
2. Schubert, M.; Hanft, D.; Nazarenus, T.; Exner, J.; Nieke, P.; Glosse, P.; Leupold, N.; Kita, J.; Moos, R. Powder Aerosol Deposition Method—Novel Applications in the Field of Sensing and Energy Technology. *Funct. Mater. Lett.* **2019**, *12*, 1930005. [CrossRef]
3. Akedo, J. Room Temperature Impact Consolidation (RTIC) of Fine Ceramic Powder by Aerosol Deposition Method and Applications to Microdevices. *J. Therm. Spray Technol.* **2008**, *17*, 181–198. [CrossRef]
4. Saunders, R.; Johnson, S.D.; Schwer, D.; Patterson, E.A.; Ryou, H.; Gorzkowski, E.P. A Self-Consistent Scheme for Understanding Particle Impact and Adhesion in the Aerosol Deposition Process. *J. Therm. Spray Technol.* **2021**, *30*, 523–541. [CrossRef]
5. Akedo, J.; Lebedev, M. Piezoelectric Properties and Poling Effect of Pb(Zr, Ti)O_3 Thick Films Prepared for Microactuators by Aerosol Deposition. *Appl. Phys. Lett.* **2000**, *77*, 1710–1712. [CrossRef]
6. Akedo, J.; Lebedev, M. Microstructure and Electrical Properties of Lead Zirconate Titanate (Pb(Zr_{52}/Ti_{48})O_3) Thick Films Deposited by Aerosol Deposition Method. *Jpn. J. Appl. Phys.* **1999**, *38*, 5397–5401. [CrossRef]
7. Kim, H.K.; Oh, J.M.; Kim, S.I.; Kim, H.J.; Lee, C.W.; Nam, S.M. Relation between Electrical Properties of Aerosol-Deposited $BaTiO_3$ Thin Films and Their Mechanical Hardness Measured by Nano-Indentation. *Nanoscale Res. Lett.* **2012**, *7*, 1–16. [CrossRef]
8. Khansur, N.H.; Eckstein, U.; Li, Y.; Hall, D.A.; Kaschta, J.; Webber, K.G. Revealing the Effects of Aerosol Deposition on the Substrate-Film Interface Using NaCl Coating. *J. Am. Ceram. Soc.* **2019**, *102*, 5763–5771. [CrossRef]
9. Khansur, N.H.; Eckstein, U.; Benker, L.; Deisinger, U.; Merle, B.; Webber, K.G. Room Temperature Deposition of Functional Ceramic Films on Low-Cost Metal Substrate. *Ceram. Int.* **2018**, *44*, 16295–16301. [CrossRef]
10. Sadl, M.; Condurache, O.; Bencan, A.; Dragomir, M.; Prah, U.; Malic, B.; Deluca, M.; Eckstein, U.; Hausmann, D.; Khansur, N.H.; et al. Energy-Storage-Efficient 0.9Pb($Mg_{1/3}Nb_{2/3}$)O_3–0.1$PbTiO_3$ Thick Films Integrated Directly onto Stainless Steel. *Acta Mater.* **2021**, *221*, 117403. [CrossRef]
11. Sadl, M.; Nadaud, K.; Bah, M.; Levassort, F.; Eckstein, U.; Khansur, N.H.; Webber, K.G.; Ursic, H. Multifunctional Energy Storage and Piezoelectric Properties of 0.65Pb($Mg_{1/3}Nb_{2/3}$)O_3-0.35$PbTiO_3$ thick Films on Stainless-Steel Substrates. *J. Phys. Energy* **2022**, *4*, 024004. [CrossRef]
12. Zhuo, F.; Eckstein, U.R.; Khansur, N.H.; Dietz, C.; Urushihara, D.; Asaka, T.; Kakimoto, K.I.; Webber, K.G.; Fang, X.; Rödel, J. Temperature-Induced Changes of the Electrical and Mechanical Properties of Aerosol-Deposited $BaTiO_3$ Thick Films for Energy Storage Applications. *J. Am. Ceram. Soc.* **2022**, *105*, 4108–4121. [CrossRef]
13. Eckstein, U.; Exner, J.; Bencan Golob, A.; Ziberna, K.; Drazic, G.; Ursic, H.; Wittkämper, H.; Papp, C.; Kita, J.; Moos, R.; et al. Temperature-Dependent Dielectric Anomalies in Powder Aerosol Deposited Ferroelectric Ceramic Films. *J. Mater.* **2022**, *8*, 1239–1250. [CrossRef]
14. Suzuki, M.; Akedo, J. Temperature Dependence of Dielectric Properties of Barium Titanate Ceramic Films Prepared by Aerosol Deposition Method. *Jpn. J. Appl. Phys.* **2010**, *49*, 09MA10. [CrossRef]
15. Khansur, N.H.; Eckstein, U.; Uršič, H.; Sadl, M.; Brehl, M.; Martin, A.; Riess, K.; de Ligny, D.; Webber, K.G. Enhanced Electromechanical Response and Thermal Stability of 0.93($Na_{1/2}Bi_{1/2}$)TiO_3-0.07$BaTiO_3$ Through Aerosol Deposition of Base Metal Electrodes. *Adv. Mater. Interfaces* **2021**, *8*, 2100309. [CrossRef]
16. Sadl, M.; Lebar, A.; Valentincic, J.; Ursic, H. Flexible Energy-Storage Ceramic Thick-Film Structures with High Flexural Fatigue Endurance. *ACS Appl. Energy Mater.* **2022**, *5*, 6896–6902. [CrossRef]
17. Maruyama, K.; Kawakami, Y.; Narita, F. Young's Modulus and Ferroelectric Property of $BaTiO_3$ Films Formed by Aerosol Deposition in Consideration of Residual Stress and Film Thickness. *Jpn. J. Appl. Phys.* **2022**, *61*, SN1011. [CrossRef]
18. Nadaud, K.; Sadl, M.; Bah, M.; Levassort, F.; Ursic, H. Effect of Thermal Annealing on Dielectric and Ferroelectric Properties of Aerosol-Deposited 0.65Pb($Mg_{1/3}Nb_{2/3}$)O_3-0.35$PbTiO_3$ thick Films. *Appl. Phys. Lett.* **2022**, *120*, 112902. [CrossRef]
19. Ryu, J.; Choi, J.J.; Hahn, B.D.; Park, D.S.; Yoon, W.H. Ferroelectric and Piezoelectric Properties of 0.948($K_{0.5}Na_{0.5}$)NbO_3−0.052$LiSbO_3$ Lead-Free Piezoelectric Thick Film by Aerosol Deposition. *Appl. Phys. Lett.* **2008**, *92*, 2006–2009. [CrossRef]

20. Hoshina, T.; Furuta, T.; Kigoshi, Y.; Hatta, S.; Horiuchi, N.; Takeda, H.; Tsurumi, T. Size Effect of Nanograined $BaTiO_3$ Ceramics Fabricated by Aerosol Deposition Method. *Jpn. J. Appl. Phys.* **2010**, *49*, 03MC02. [CrossRef]
21. Khansur, N.H.; Eckstein, U.; Riess, K.; Martin, A.; Drnec, J.; Deisinger, U.; Webber, K.G. Synchrotron X-ray Microdiffraction Study of Residual Stresses in $BaTiO_3$ Films Deposited at Room Temperature by Aerosol Deposition. *Scr. Mater.* **2018**, *157*, 86–89. [CrossRef]
22. Sadl, M.; Tomc, U.; Prah, U.; Ursic, H. Protective Alumina Coatings Prepared by Aerosol Deposition on Magnetocaloric Gadolinium Elements. *Inf. MIDEM* **2019**, *49*, 177–182. [CrossRef]
23. ImageJ. Available online: https://imagej.net/ij/ (accessed on 27 December 2022).
24. Oliver, W.C.; Phaar, G.M. An Improvved Techniques for Determining Hardness and Elastic Modulus Using Using Load and Dispacement Sensing Indentation Experiments. *J. Mater. Res.* **1992**, *7*, 1564–1583. [CrossRef]
25. Catalan, G.; Corbett, M.H.; Bowman, R.M.; Gregg, J.M. Effect of Thermal Expansion Mismatch on the Dielectric Peak Temperature of Thin Film Relaxors. *J. Appl. Phys.* **2002**, *91*, 2295–2301. [CrossRef]
26. Uršič, H.; Vrabelj, M.; Otoničar, M.; Furlanović, L.; Rožič, B.; Kutnjak, Z.; Bobnar, V.; Malič, B. Influence of Synthesis-Related Microstructural Features on the Electrocaloric Effect for $0.9Pb(Mg_{1/3}Nb_{2/3})O_3$–$0.1PbTiO_3$ Ceramics. *Crystals* **2021**, *11*, 372. [CrossRef]
27. Stainless Steel—Grade 304 (UNS S30400). Available online: https://www.azom.com/properties.aspx?ArticleID=965 (accessed on 13 January 2023).
28. Walls, M.G.; Chaudhri, M.M.; Tang, T.B. Stm Profilometry of Low-Load Vickers Indentations in a Silicon Crystal. *J. Phys. D Appl. Phys.* **1992**, *25*, 500–507. [CrossRef]
29. Devaraj, A.; Barton, D.J.; Li, C.H.; Lambeets, S.V.; Liu, T.; Battu, A.; Vaithiyalingam, S.; Thevuthasan, S.; Yang, F.; Guo, J.; et al. Visualizing the Nanoscale Oxygen and Cation Transport Mechanisms during the Early Stages of Oxidation of Fe–Cr–Ni Alloy Using In Situ Atom Probe Tomography. *Adv. Mater. Interfaces* **2022**, *9*, 2200134. [CrossRef]
30. Navickas, E.; Huber, T.M.; Chen, Y.; Hetaba, W.; Holzlechner, G.; Rupp, G.; Stöger-Pollach, M.; Friedbacher, G.; Hutter, H.; Yildiz, B.; et al. Fast Oxygen Exchange and Diffusion Kinetics of Grain Boundaries in Sr-Doped $LaMnO_3$ Thin Films. *Phys. Chem. Chem. Phys.* **2015**, *17*, 7659–7669. [CrossRef]
31. Daneshian, B.; Gärtner, F.; Assadi, H.; Vidaller, M.V.; Höche, D.; Klassen, T. Features of Ceramic Nanoparticle Deformation in Aerosol Deposition Explored by Molecular Dynamics Simulation. *Surf. Coat. Technol.* **2022**, *429*, 127886. [CrossRef]
32. Porz, L.; Klomp, A.J.; Fang, X.; Li, N.; Yildirim, C.; Detlefs, C.; Bruder, E.; Höfling, M.; Rheinheimer, W.; Patterson, E.A.; et al. Dislocation-Toughened Ceramics. *Mater. Horiz.* **2021**, *8*, 1528–1537. [CrossRef]
33. Zak, S.; Trost, C.O.W.; Kreiml, P.; Cordill, M.J. Accurate Measurement of Thin Film Mechanical Properties Using Nanoindentation. *J. Mater. Res.* **2022**, *37*, 1373–1389. [CrossRef]

crystals

MDPI

Supplementary material

Influence of Thermal Treatment on the Cross-Sectional Properties of Aerosol-Deposited $Pb(Mg_{1/3}Nb_{2/3})O_3$–$PbTiO_3$ Thick Films

Katarina Žiberna [1,2,*], Matej Šadl [1,2], Aljaž Drnovšek [3], Goran Dražić [1,2,4], Hana Uršič [1,2] and Andreja Benčan [1,2]

[1] Electronic Ceramics Department, Jožef Stefan Institute, Jamova cesta 39, 1000 Ljubljana, Slovenia; matej.sadl@ijs.si (M.Š.); hana.ursic@ijs.si (H.U.); andreja.bencan@ijs.si (A.B.)
[2] Jožef Stefan International Postgraduate School, Jamova cesta 39, 1000 Ljubljana, Slovenia
[3] Department of Thin Films and Surfaces, Jožef Stefan Institute, Jamova cesta 39, 1000 Ljubljana, Slovenia; aljaž.drnovsek@ijs.si (A.D.)
[4] Department of Materials Chemistry, National Institute of Chemistry, Hajdrihova 19, 1000 Ljubljana, Slovenia; goran.drazic@ki.si (G.D.)
* Correspondence: katarina.ziberna@ijs.si (K.Ž.)

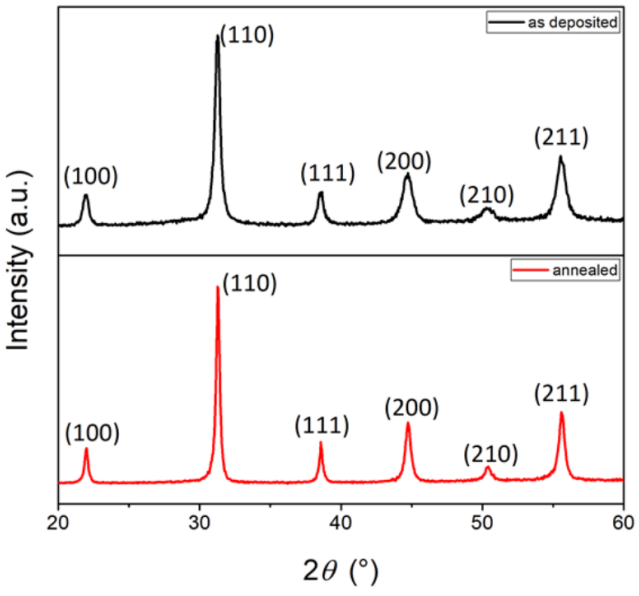

Figure S1: X-ray diffraction patterns of the as deposited and the annealed film. All peaks were indexed with a cubic perovskite structure (space group $Pm\bar{3}m$, JCPDS 81-0861).

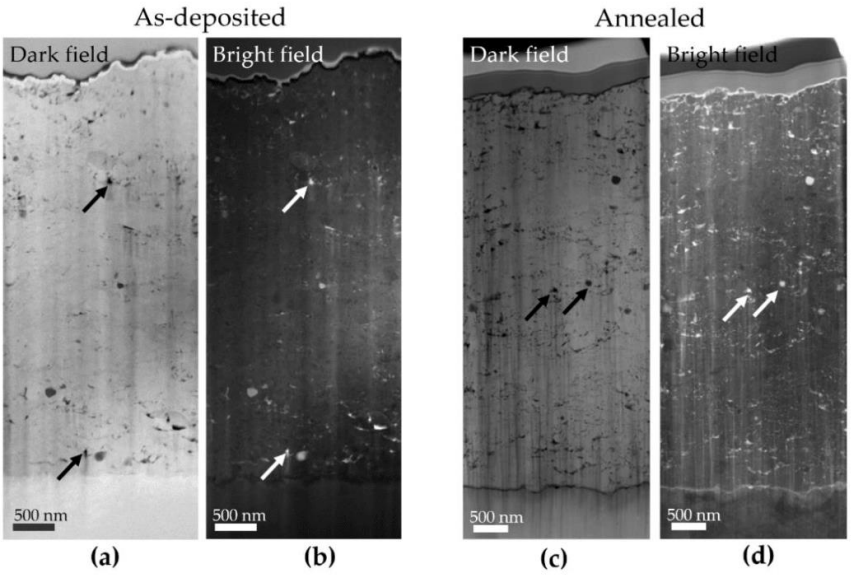

Figure S2. Scanning transmission electron microscopy (STEM) (**a**) dark-field and (**b**) bright-field images of the as-deposited film; (**c**) the dark-field and (**d**) bright-field images of the annealed film. Note that the black and white arrows point to pores locations, which are black in dark field and white in bright field. The vertical lines observed on the STEM images are a consequence of the focused ion beam curtain effect.

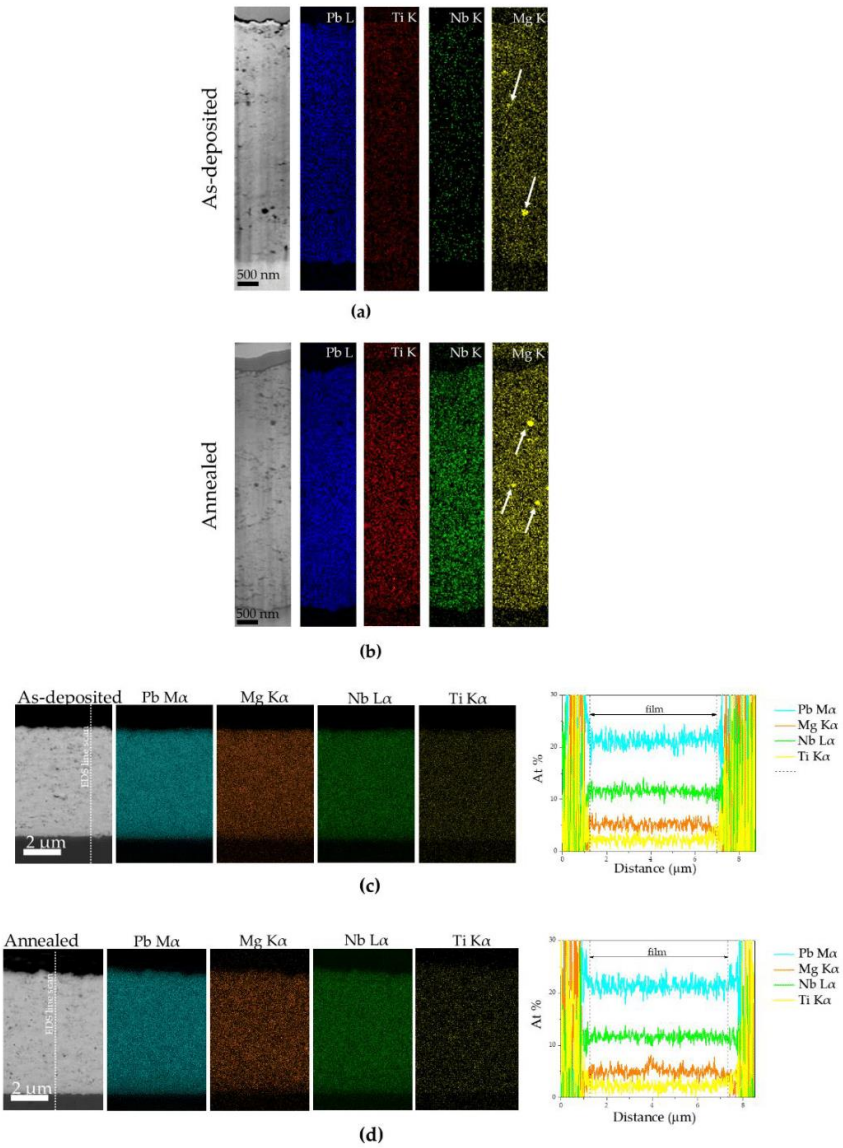

Figure S3. Compositional analysis of the as deposited and the annealed film, respectively, performed using **(a,b)** EDS-STEM and **(c,d)** EDS-SEM with the corresponding EDS line analysis. The white arrows in **(a,b)** indicate the Mg-rich inclusions.

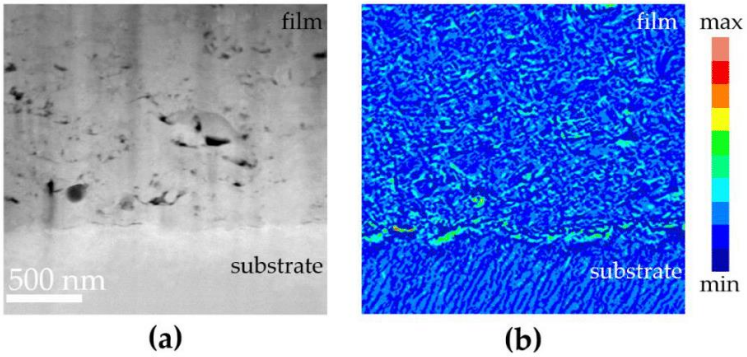

Figure S4. (**a**) STEM dark-field image of the film-substrate interface in the as-deposited film; (**b**) the corresponding divergence map obtained from the 4D STEM dataset using differential phase contrast. Areas with higher contrast in the divergence map represent higher local strain.

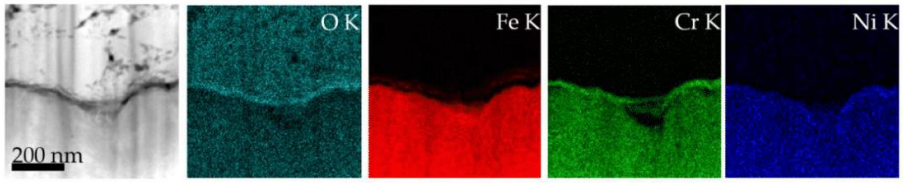

Figure S5. EDS of the film-substrate interface of the annealed PMN–10PT thick film resolving a layered structure formed due to oxidation of the substrate at 500 °C. The layer structure is composed (from substrate to film) of an Fe- and Ni-rich layer, a Cr_xO_y layer and an Fe_mO_n layer.

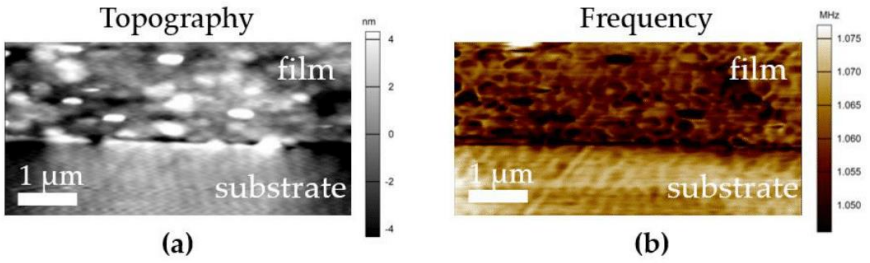

Figure S6. (**a**) Topography and (**b**) frequency mapping at the film-substrate interface of the as-deposited film measured in the contact resonance frequency viscoelastic mapping mode. This is an atomic force microscopy technique in which the frequency measured is the resonant frequency of the tip-material system and is related to the Young's modulus of the material. The higher the frequency, the higher the Young's modulus and vice versa. In **b**, a higher frequency is measured in the substrate than in the film, which means that the substrate has a higher Young's modulus than to the film.

Chapter 4

Nanomechanical Characterization of $BiFeO_3$ Ferroelectric Ceramics

The study reports the measured E and H of $BiFeO_3$ ceramics, along with the structural and microstructural defects formed during plastic deformation under a cube corner diamond indentation probe.

Within the measurement range of 200 μN to 2 mN, both E and H decreased from (113.7 ± 6.9) GPa and (9.9 ± 0.4) GPa, respectively (measured at 200 μN), to (105.1 ± 5.3) GPa and (6.6 ± 0.2) GPa (measured at 2 mN). The decrease in E is attributed to microstructural features in the ceramic, primarily grain boundaries and pores, as the elastic deformation zone increases with increasing force, while the decrease in H is associated with the indentation size effect.

Small-scale ductility was observed up to 500 μN. At 1 mN and above, the transition to characteristic brittle behavior was observed.

As soon as the theoretical shear stress of 7.4 GPa was exceeded during loading, the homogeneous formation of dislocations began. A dislocation array was observed emanating from the region near the imprinted surface, indicating dislocation multiplication and movement after nucleation. The dislocations near the imprinted surface began to reorganize into low-angle grain boundaries, forming subgrains that retained some of the original crystallographic orientation of the deformed crystallite. The accumulation of dislocations on these sub-grains is believed to be the cause of the surface cracks due to stress build-up.

Interestingly, there was no conclusive evidence of irreversible movement of the DWs motion during deformation.

This chapter addresses the objective 2 and hypotheses 1, 2, 3, 4, and 5.

Published in: K. Žiberna, M. Koblar, M. Bah, F. Levassort G. Dražić, H. Uršič and A. Benčan, "Nanomechanical characterization of $BiFeO_3$ ferroelectric ceramics", *Journal of the European Ceramic Society,* **44**, 7025-7031, 2024,
https://doi.org/10.1016/j.jeurceramsoc.2024.05.011.

My contribution: I metallographically prepared the ceramic sample and performed SEM, electron backscatter diffraction (EBSD), TEM, STEM, and 4D STEM analysis. I performed nanoindentation. I performed AFM measurements, in particular PFM, CRFM and analyzed the data. Together with the co-authors, we interpreted the data, developed the manuscript concept, and wrote the paper.

Journal of the European Ceramic Society 44 (2024) 7025–7031

Contents lists available at ScienceDirect

Journal of the European Ceramic Society

journal homepage: www.elsevier.com/locate/jeurceramsoc

Nanomechanical characterization of $BiFeO_3$ ferroelectric ceramics

Katarina Žiberna [a,b,*], Maja Koblar [a], Micka Bah [c], Franck Levassort [c], Goran Dražić [a,b,d], Hana Uršič [a,b], Andreja Benčan [a,b]

[a] Electronic Ceramics Department, Jožef Stefan Institute, Jamova cesta 39, Ljubljana 1000, Slovenia
[b] Jožef Stefan International Postgraduate School, Jamova cesta 39, Ljubljana 1000, Slovenia
[c] GREMAN UMR7347, Université de Tours, CNRS, INSA CVL, 16 rue Pierre et Marie Curie, Tours 37071, France
[d] Department of Materials Chemistry, National Institute of Chemistry, Hajdrihova 19, Ljubljana 1000, Slovenia

ARTICLE INFO

Keywords:
Nanoindentation
Mechanical properties
Plastic deformation
$BiFeO_3$ ceramics

ABSTRACT

Ferroelectric perovskites are pivotal in diverse technological applications; however, a gap persists in our comprehension of their mechanical properties, emphasizing the need for additional exploration. In the present study, we report on the nanomechanical behavior of $BiFeO_3$ ceramics in the force range between 200 μN and 2 mN, including the evolution of the hardness and the reduced Young's modulus from (9.9 ± 0.4) GPa and (113.7 ± 6.9) GPa, respectively, with increasing force. A sequence of plastic-deformation mechanisms under the cube-corner probe was revealed through a first pop-in analysis in combination with a variety of electron microscopy techniques, starting with a homogeneous dislocation nucleation, multiplication and rearrangement leading to sub-grain formation, a phenomenon observed in metals but not in ceramics.

1. Introduction

In terms of mechanical properties, oxide perovskites are best known for their brittleness. Whether in the form of ceramics or as single crystals, compared to metals, perovskites at room temperature exhibit very little ductility, i.e., plastically deformability, under mechanical loading due to their strong ionic/covalent bonds and the low density of plastic flow carriers in the form of dislocations. Dislocations are line defects that make materials ductile, but conventional synthesis routes that require high annealing temperatures make perovskites nearly free of dislocations with a dislocation density of ~ 10^9 m^{-2} (for comparison, the dislocation density in a metal is ~ 10^{14} m^{-2}) [1,2]. However, there are some perovskites that exhibit surprising plastic deformability at room temperature, namely $SrTiO_3$, which can withstand a level of plastic deformation of ~7% [3,4] and $KNbO_3$, which is deformable up to ~5% [5]. Deformability also varies with temperature [4,6,7] and across scales [8–10].

When deformed at room temperature with forces below a critical load, e.g., by nanoindentation, dislocations are formed by the activation of the room-temperature perovskite slip system family of $\{110\}_{pc}\langle\bar{1}10\rangle_{pc}$ (pc refers to the pseudo-cubic crystal lattice) without cracking of the material [8]. Such dislocations can also be referred to as geometrically necessary dislocations (GNDs), which form to adapt to plastic deformation [11]. With an increasing indentation force, dislocations pile up below the indented surfaces and serve as stress centers for crack nucleation with sharp indentation probes [12]. This is unlike for probes with large radii, where the crack nucleation and incipient plasticity occur simultaneously, due to a higher probability of probing pre-exiting defects that serve as crack-nucleation sites [13]. Understanding the competing mechanism of incipient plasticity and cracking during deformation provides an insight into the controlled introduction of dislocations into perovskites, both macroscopically and locally [14], as they can be used as structural defects for property tailoring. A sufficient amount of dislocations can enhance their plastic deformability and suppress cracking [15,16], and in the case of ferroelectrics, it can lead to ferroelectric hardening and an increase in the large signal d_{33}* coefficient, as reported for $BaTiO_3$ [17,18].

Ferroelectric perovskites are technologically indispensable and are widely used as sensors, actuators and transducers [19]. One of the features of ferroelectrics are microstructural elements called domain walls (DWs) that separate domains with homogeneous spontaneous polarization orientation [20]. In addition to dislocation nucleation and their dynamics, ferroelastic DWs, i.e. non-180° DWs, and their motion can also contribute to the remanent deformation of a ferroelectric. The cooperation between dislocation formation and ferroelastic switching has been evidenced in $BaTiO_3$ during nanoindentation [21,22], where

* Corresponding author at: Electronic Ceramics Department, Jožef Stefan Institute, Jamova cesta 39, Ljubljana 1000, Slovenia.
E-mail address: Katarina.Ziberna@ijs.si (K. Žiberna).

https://doi.org/10.1016/j.jeurceramsoc.2024.05.011
Received 5 February 2024; Received in revised form 26 April 2024; Accepted 6 May 2024
Available online 7 May 2024

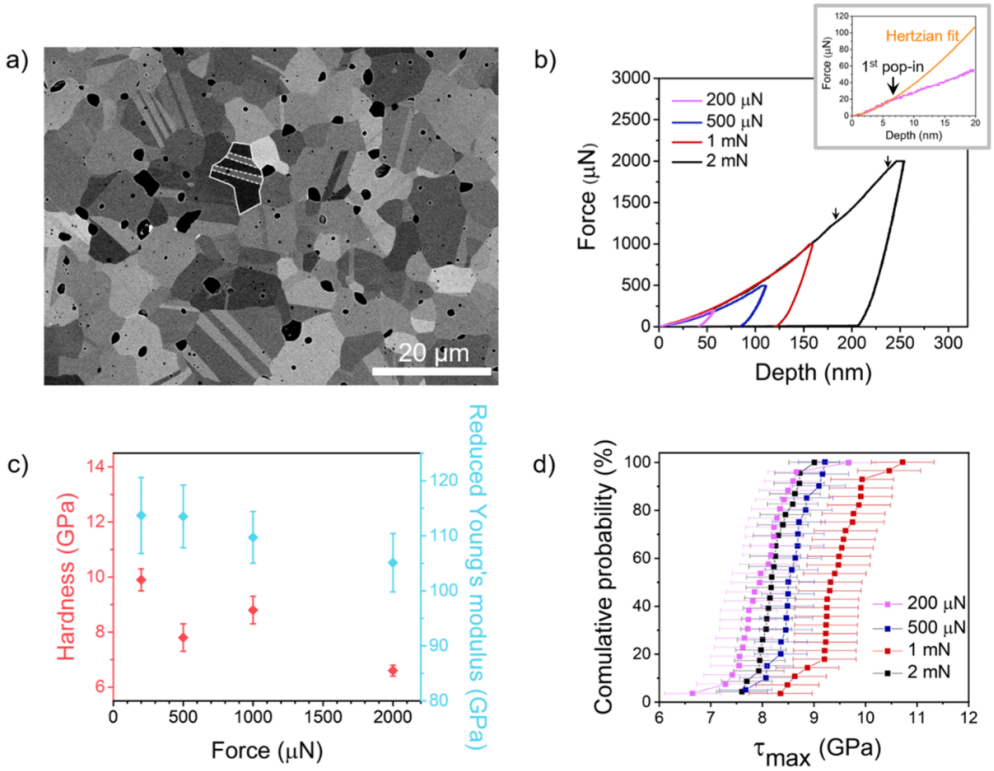

Fig. 1. a) BSE image of the BFO ceramic after sintering. DWs are marked with white dashed lines within the circled grain; b) Representative indentation curves at different forces. Black arrows mark examples of pop-in events at higher forces. The inset shows a close-up of a representative indentation curve at low forces fitted with the Hertzian theory of elastic contact. The deviation of the indentation curve from the Hertzian fit marks the transition from the elastic to the elastoplastic behavior of the material, also known as the first pop-in; c) H and E_r of BFO as a function of indentation force. The error bars represent the standard deviation; d) Statistical distribution of τ_{max} calculated from the first pop-ins for the four indentation forces used. The error bars represent the standard deviation.

preferred orientation. However, it should be noted that both properties are anisotropic and can vary from grain to grain depending on the crystallographic orientation [27]. Both H and E_r decrease with the increasing force. For H, the decrease can be explained by the so-called indentation size effect, which makes the H of the materials appear higher at lower indentation forces than expected from measurements of H in the bulk. The indentation size effect is a consequence of the GNDs that form to accommodate the plastic deformation and the strain gradients associated with the GNDs. Since the strain gradients are size dependent being greater at low indentation forces, the flow stress of a the material changes with the indentation force, making the material appear harder at lower forces [11].

Similarly, the strain gradients can also contribute to the decrease in E_r with increasing force through the flexoelectric effect, as observed in $BaTiO_3$ [28] and $SrTiO_3$ [29]. Larger strain gradients at low indentation forces induce polarization, which leads to an increase in the elastic constants of the material. The dependence of E_r on the indentation force is more pronounced for materials with high flexoelectric coefficients, which in turn depend on their dielectric constant [28,29]. However, it is likely that the main contribution to the decrease in E_r with increasing force is the increased likelihood of probing microstructural defects that would contribute to lowering the E_r, such as grain boundaries and pores. Even if the indentation were not made directly at the grain boundaries or in direct proximity to the pores, the elastically deformed hemispherical volume around the indentation can be up to 10 times larger than the indentation observed at the surface [30]. From this point of view, it can be assumed that the most realistic value for BFO was measured at 200 μN with $E_r = 113.6$ GPa, as the chances of probing microstructural defects are minimized. The E calculated from E_r at 200 μN is 116.9 GPa, taking into account the elastic properties of the indentation tip ($E_i = 1140$ GPa, $\nu_i = 0.07$) and the Poisson's ratio (ν) of the sample equal to 0.27 [31] according to [23]:

$$\frac{1}{E_r} = \frac{1-\nu_i^2}{E_i} + \frac{1-\nu^2}{E} \quad (1)$$

The calculated E agrees well with first-principles studies predicting an E of 118.2 GPa for rhombohedral BFO [31], as well as with estimates of E_r obtained using atomic force microscopy (AFM) techniques (Figure S3). We excluded the contributions of the observed secondary phase to the decrease in E_r (Figure S4) as well as any contributions from the mechanically softer ferroelectric and ferroelastic DWs that cannot be detected by nanoindentation due to the resolution of the technique (Figure S5). The reversible movement of the ferroelastic DWs, which would manifest as anelasticity, i.e. nonlinearity in the lower part of the unloading curve [32], was also excluded as a significant contribution, since the E_r value is extracted from the upper part of the unloading curve [23].

The second piece of information obtained from the indentation curves is the maximum shear stress (τ_{max}) required for the material to deform plastically. τ_{max} was calculated from the first pop-in in the indentation curves, which is associated with the transition from a purely elastic to an elasto-plastic behavior of the material, more precisely with the dislocation nucleation and motion [22]. An example of the first pop-in is showed in the inset of Fig. 1**b**. At low indentation forces, the

material response is initially elastic, which can be described mathematically according to the Hertzian theory of elasticity as follows [33,34]:

$$F = \frac{4}{3}E_r\sqrt{R}h^{\frac{3}{2}} \quad (2)$$

where F is the force, E_r is the reduced Young's modulus, R is the radius of the curvature of the indentation probe and h is the indentation depth. In our case we fitted this first part of the curves with $R = 60$ nm (Fig. 1**b**, inset, orange curve). The onset of the deviation for the measured curves from the Hertzian fit marks the first pop-in. The τ_{max} at the time of the first pop-in can be quantified as [34]:

$$\tau_{\max} = 0.31\left(\frac{6E_r^2}{\pi^3R^2}F_0\right)^{\frac{1}{3}} \quad (3)$$

where F_0 is the force at the first pop-in. Fig. 1**d** shows the statistical analysis of τ_{max} calculated for all four indentation forces. The distribution of τ_{max} appears to be similar in all four cases, with the average value being close to the estimated theoretical shear strength (τ_{th}) of $\tau_{th} \sim E/4\pi(1+\nu) \sim 118.2/4\pi(1+0.27) \sim 7.4$ GPa. A τ_{max} value as high as τ_{th} indicates a homogeneous nucleation of GNDs at the first pop-in in regions without pre-existing defects such as dislocations, dislocation sources, or surface defects [13,14]. The onset of the incipient dislocation plasticity appears to be independent of the rate of the applied force (note that the rate of force changes for each applied force, as the time of loading was held constant in all four cases regardless of the force), which was also observed in nanoindentation measurements on $SrTiO_3$ [35].

In addition to the first pop-ins, subtle pop-ins at higher forces were also observed in the indentation curves, which are normally associated with cracking [13]. They are most evident in the 2 mN curve (Fig. 1**b**, black curve, marked with black arrows), but in general they occur stochastically, unlike the first pop-ins.

For a deeper understanding of the incipient dislocation plasticity, i.e., dislocation nucleation, movement and propagation as well as crack formation, postmortem SEM surface analysis and STEM cross-sectional analysis of the regions deformed by the indentations were carried out.

The residual indentations for selected forces, i.e. 200 μN, 500 μN, 1 mN and 2 mN, are shown in Fig. 2. At 200 μN and 500 μN, no cracks were observed on the surface (Fig. 2**a** and Fig. 2**b**), which is consistent with the observations of a "ductile" mechanical response of other perovskites in nanoscale mechanical experiments [8,9]. At 1 mN and above, a change in the contrast of the BSE images around the indentation is observed (Fig. 2**c** and Fig. 2**d**), possibly caused by the severe plastic deformation or/and ferroelastic switching along with cracking and piling up of the material around the indentations. The observed cracking might also have contributed to the decreases in H and E_r at higher forces (Fig. 1**c**). In the case of the BFO indented with a cube-corner probe, the transition from ductile to brittle behavior is therefore between the indentation forces of 500 μN and 1 mN.

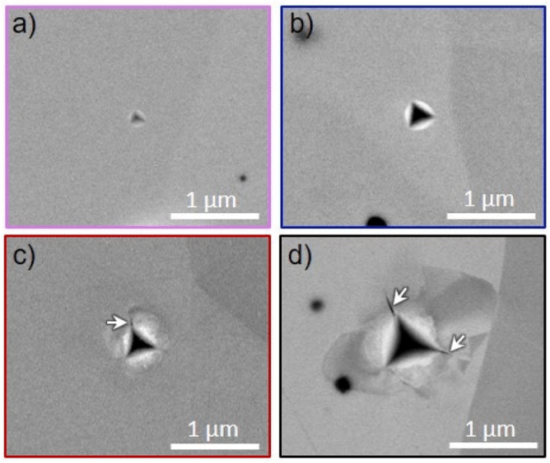

Fig. 2. BSE images of residual indentations created with forces of a) 200 μN, b) 500 μN, c) 1 mN and d) 2 mN. Cracking around indentations is indicated by with white arrows.

In Fig. 3**a**, a cross-sectional STEM image of the area under a 1-mN indentation is presented, revealing an asymmetrical arrangement of dislocations created under the hydrostatic stress acting on the material during the nanoindentation. Asymmetric distributions of the dislocations below the indentation have also been observed in other oxides [36] and can be attributed to the limited number of slip systems in perovskites and ceramics, in general, compared to metals in which the plastic deformation zone is more symmetrical in shape [37,38]. More specifically, the dislocations were identified as belonging to the room-temperature slip system of perovskites $\{110\}_{pc}\langle\bar{1}10\rangle_{pc}$ [39]. The dislocations that lie on $(011)_{pc}$ and $(0\bar{1}1)_{pc}$ are edge-on dislocations relative to the $[100]_{pc}$ viewing direction, while the dislocations that appear to lie on the $(010)_{pc}$ and $(001)_{pc}$ planes are non-edge on and in the $[100]_{pc}$ zone axis appear as projections of the dislocations on $(110)_{pc}$ or $(\bar{1}10)_{pc}$ and $(101)_{pc}$ or $(10\bar{1})_{pc}$ planes, respectively. For reference, we also looked at the cross-section of a non-deformed region (Figure S6), where there appears to be no pre-existing dislocations in the near-surface region. Thus, the observed dislocations were not present in the material before the nanoindentation, but formed to accommodate the stress caused during the nanoindentation, which is consistent with the prediction of homogeneous dislocation nucleation based on the calculation of τ_{max} (Fig. 1**d**).

A group of dislocations appears to be emitted from beneath the deformed surface, reaching deep into the material and forming a dislocation array (Fig. 3**a**). The dislocations appear to originate from a point source closer to the deformed surface and increase in size with depth, suggesting multiplication like from a Frank-Read source. Frank-Read sources have been reported to play a minor role in the multiplication of dislocations in macroscopically deformed perovskites, where other mechanisms predominate [1], e.g., (multiple) cross slip [5]. Similar array structures have also been observed in nanoindented ZnO and ZnS [36,40], suggesting that they might be a characteristic defect structure of ionic crystals deformed using nanoindentation.

The indentation in Fig. 3**a** was actually made on a DW that is not visible in the STEM image due to poor diffraction contrast. The same region as showed in Fig. 3a, can be seen in Figure S7 viewed in TEM mode, where due to better diffraction contrast, the DW below the plastically deformed region is visible. The DW was recognized as a 109° DW and thus possesses ferroelastic properties in addition to ferroelectric properties [20]. This suggests that the DW could potentially be mobile during the indentation, although its persistent position below the indentation and its unaltered morphology (Figure S7) observed after the indentation might be an indication of (partial) pinning by point defects known to segregate on DWs in BFO [25,41] and dislocations [17,18] that form in the early stages of the indentation (Fig. 1**b**).

Fig. 3**b** shows a close-up of the deformed surface of an indentation made at a force of 2 mN. A higher dislocation density was observed in the near-surface region compared to the entire area of plastic deformation, along with chipping of the piled-up material, cracking around the indentation and strains around the crack tip (Figure S8). A high-angle annular dark-field (HAADF) image of the area marked with a white square in Fig. 3**b** revealed that the material directly below the indented surface does not remain intact but appears to crumble into nm-sized sub-grains, which was observed to a greater extent around the 2-mN indentation (Fig. 3**c**). The sub-grains also appear to retain the original orientation of the indentation-deformed crystallite to some extent, as shown by the FFT in Fig. 3**d**. Sub-grains have also been

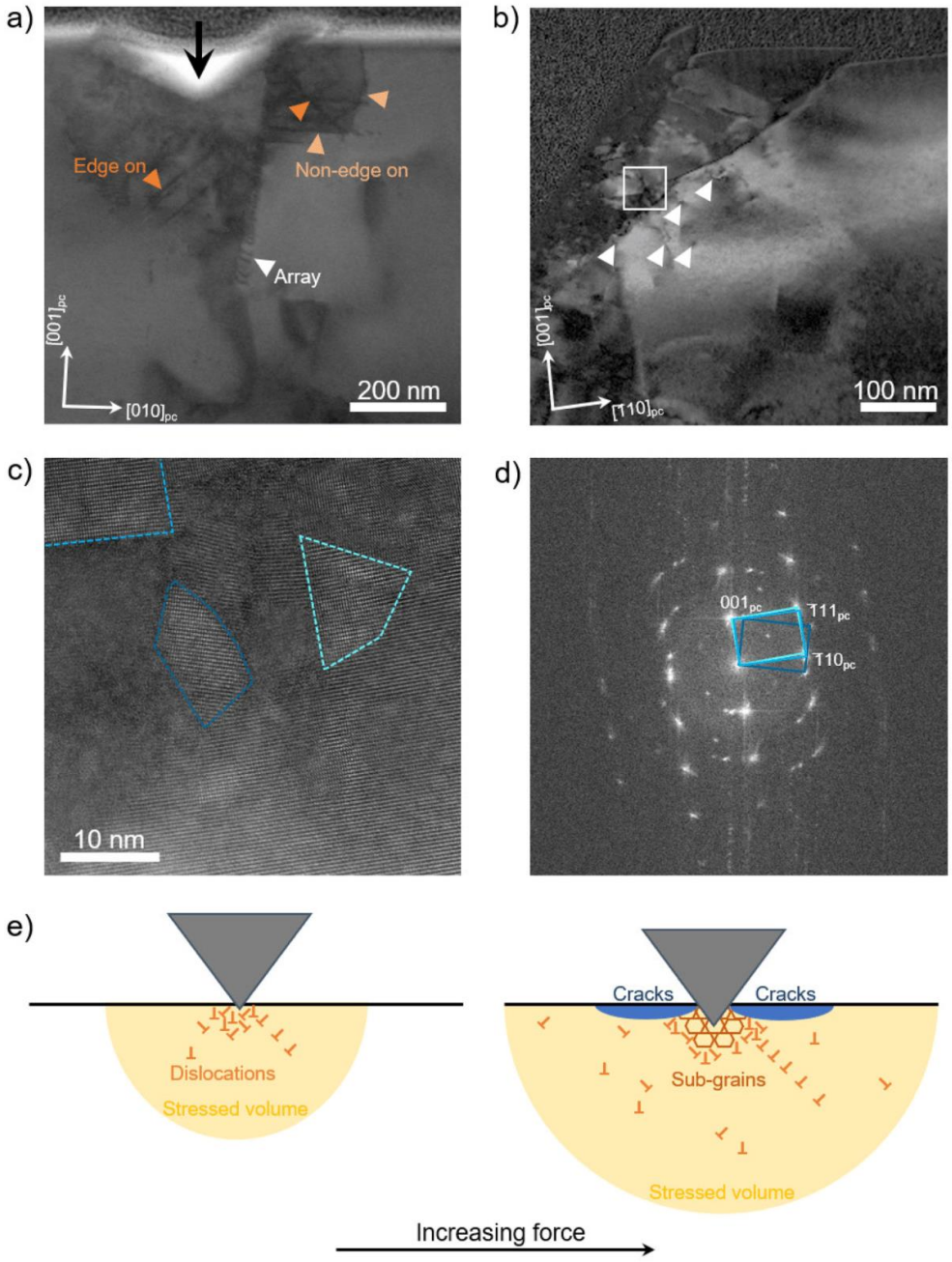

Fig. 3. a) Cross-sectional STEM bright-field image of the area below a 1-mN indentation. The black arrow marks the indented surface, while the triangles mark dislocations; b) Magnitude map of the vector-field calculated from the center of mass of a crack near the indented surface of a 2-mN indentation. White triangles mark dislocations; c) HAADF image of the region marked with a rectangle in b, showing the subdivision into smaller grains. Terminal planes of the grains are marked with dashed lines; d) FFT of image c. The selected diffraction spots marked with colors correspond to the grains marked in c; e) Schematic of the plastic-deformation sequence during indentation.

observed near a Vickers indentation in a (001) oriented $SrTiO_3$ single crystal, where the dislocations were arranged in a network and formed rectangular sub-grains of more than 1 μm in size [42].

Based on the results of the pop-in analysis and the microscopic analysis, we propose a deformation sequence in the BFO deformed with a cube-corner indentation probe, as shown in Fig. 3**e**. The deformation of a region without pre-existing defects starts with the homogeneous nucleation of dislocations, which additionally start to move and

[26] T. Rojac, H. Ursic, A. Bencan, B. Malic, D. Damjanovic, Mobile domain walls as a bridge between nanoscale conductivity and macroscopic electromechanical response, Adv. Funct. Mater. 25 (2015) 2099–2108, https://doi.org/10.1002/adfm.201402963.

[27] S. Sun, Y. Fang, G. Kieslich, T.J. White, A.K. Cheetham, Mechanical properties of organic-inorganic halide perovskites, $CH_3NH_3PbX_3$ (X = I, Br and Cl), by nanoindentation, J. Mater. Chem. A. 3 (2015) 18450–18455, https://doi.org/10.1039/c5ta03331d.

[28] M. Gharbi, Z.H. Sun, P. Sharma, K. White, The origins of electromechanical indentation size effect in ferroelectrics, Appl. Phys. Lett. 95 (2009) 142901, https://doi.org/10.1063/1.3231442.

[29] C.R. Robinson, K.W. White, P. Sharma, Elucidating the mechanism for indentation size-effect in dielectrics, Appl. Phys. Lett. 101 (2012) 17–19, https://doi.org/10.1063/1.4753799.

[30] S.J. Bull, Microstructure and indentation response of TiN coatings: the effect of measurement method, Thin Solid Films 688 (2019) 137452, https://doi.org/10.1016/j.tsf.2019.137452.

[31] N.V. Srihari, S. Nayak, P. Poornesh, K.K. Nagaraja, Variation in the electronic, mechanical, and structural properties among the polymorphs of bismuth ferrite: a first-principles approach, Eur. Phys. J. 138 (2023) 465, https://doi.org/10.1140/epjp/s13360-023-04102-1.

[32] M. Algueró, A.J. Bushby, M.J. Reece, M.L. Calzada, L. Pardo, Mechanical characterisation of ferroelectric thin films for mems, Integr. Ferroelectr. 32 (2001) 83–92, https://doi.org/10.1080/10584580108215680.

[33] H. Hertz, On the contact of elastic solids, J. FüR. Die Reine Und Angew. Math. 92 (1882) 156–171.

[34] K.L. Johnson, Contact Mechanics, Cambrige University Press, Cambridge, United Kingdom, 1985, https://doi.org/10.1017/CBO9781139171731.

[35] X. Wang, X. Liu, Y. Li, X. Fang, Determination of the controlling parameters for dislocation nucleation in $SrTiO_3$: an investigation by nanoindentation, J. Am. Ceram. Soc. 106 (2023) 6085–6097, https://doi.org/10.1111/jace.19218.

[36] Y. Li, X. Fang, E. Tochigi, Y. Oshima, S. Hoshino, T. Tanaka, H. Oguri, S. Ogata, Y. Ikuhara, K. Matsunaga, A. Nakamura, Shedding new light on the dislocation-mediated plasticity in wurtzite ZnO single crystals by photoindentation, J. Mater. Sci. Technol. 156 (2023) 206–216, https://doi.org/10.1016/j.jmst.2023.02.017.

[37] C.D. Hardie, S.G. Roberts, Nanoindentation of model Fe-Cr alloya with self-ion irradiation, J. Nucl. Mater. 433 (2013) 174–179, https://doi.org/10.1016/j.jnucmat.2012.09.003.

[38] D. Wei, Y. Koizumi, M. Nagasako, Y. Kubota, T. Aoyagi, Y. Nakagawa, M. Yoshino, A. Chiba, H. Kato, Introducing dislocations locally in Al-supersaturated α_2-Ti_3Al single crystal via nanoscale wedge indentation, Intermetallics 113 (2019) 106557, https://doi.org/10.1016/j.intermet.2019.106557.

[39] N. Doukhan, J.C. Doukhan, Dislocations in perovskites $BaTiO_3$ and $CaTiO_3$, Phys. Chem. Miner. 13 (1986) 403–410, https://doi.org/10.1007/BF00309185.

[40] A. Nakamura, X. Fang, A. Matsubara, E. Tochigi, Y. Oshima, T. Saito, T. Yokoi, Y. Ikuhara, K. Matsunaga, Photoindentation: a new route to understanding dislocation behavior in light, Nano Lett. 21 (2021) 1962–1967, https://doi.org/10.1021/acs.nanolett.0c04337.

[41] A. Bencan, G. Drazic, H. Ursic, M. Makarovic, M. Komelj, T. Rojac, Domain-wall pinning and defect ordering in $BiFeO_3$ probed on the atomic and nanoscale (https://doi.org/https://doi.org/), Nat. Commun. 11 (2020) 1762, https://doi.org/10.1038/s41467-020-15595-0.

[42] K.H. Yang, N.J. Ho, H.Y. Lu, Deformation microstructure in (001) single crystal strontium titanate by vickers indentation (https://doi.org/), J. Am. Ceram. Soc. 92 (2009) 2345–2353, https://doi.org/10.1111/j.1551-2916.2009.03189.x.

[43] N. Hansen, R.F. Mehl, New discoveries in deformed metals, Metall. Mater. Trans. A Phys. Metall. Mater. Sci. 32 (2001) 2917–2935, https://doi.org/10.1007/s11661-001-0167-x.

Supporting information

Nanomechanical characterization of $BiFeO_3$ ferroelectric ceramics

Katarina Žiberna[1,2,*], Maja Koblar[1], Micka Bah[3], Franck Levassort[3], Goran Dražić[1,2,4],

Hana Uršič[1,2] and Andreja Benčan[1,2]

[1]*Electronic Ceramics Department, Jožef Stefan Institute, Jamova cesta 39, 1000 Ljubljana, Slovenia*

[2]*Jožef Stefan International Postgraduate School, Jamova cesta 39, 1000 Ljubljana, Slovenia*

[3]*GREMAN UMR7347, Université de Tours, CNRS, INSA CVL, 16 rue Pierre et Marie Curie, 37071 Tours, France*

[4]*Department of Materials Chemistry, National Institute of Chemistry, Hajdrihova 19, 1000 Ljubljana, Slovenia*

*corresponding author: Katarina.Ziberna@ijs.si

S1: Microstructural characterization of BFO ceramic

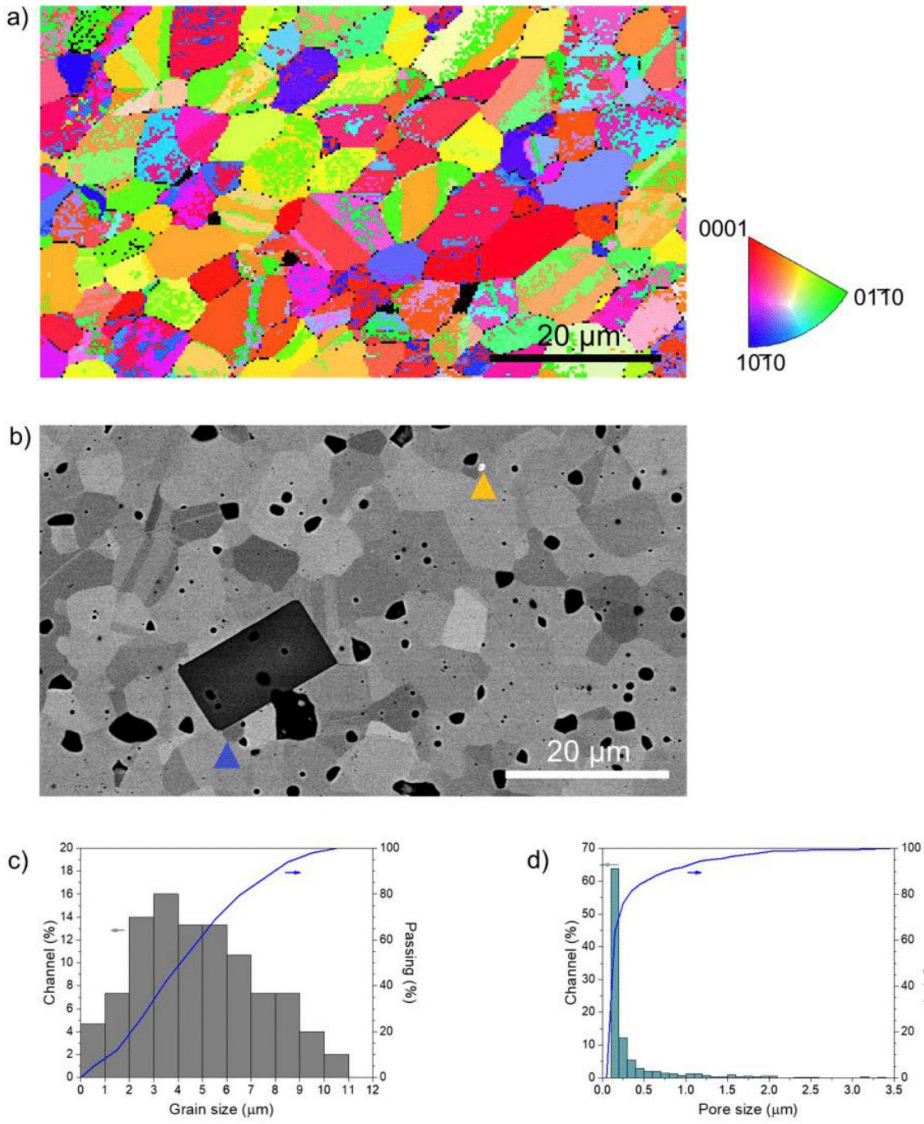

Figure S1: a) EBSD orientation map of the BFO ceramic, showing a random orientation of the grains within the ceramic. The *R*3*c* space group was used for indexing the Kikuchi patterns; b) BSE image of the BFO microstructure in which secondary phases, i.e. the bismuth-rich phase (yellow arrow) and the iron-phase (blue arrow), were detected. Secondary phases in BFO are very frequently observed [1] and are almost unavoidable due to the kinetic [2] and thermodynamic [3] particularities of the Bi_2O_3-Fe_2O_3 system; c) Grain size distribution of the ceramic; d) Pore size distribution of the ceramic.

S2. EBSD analysis of domain walls

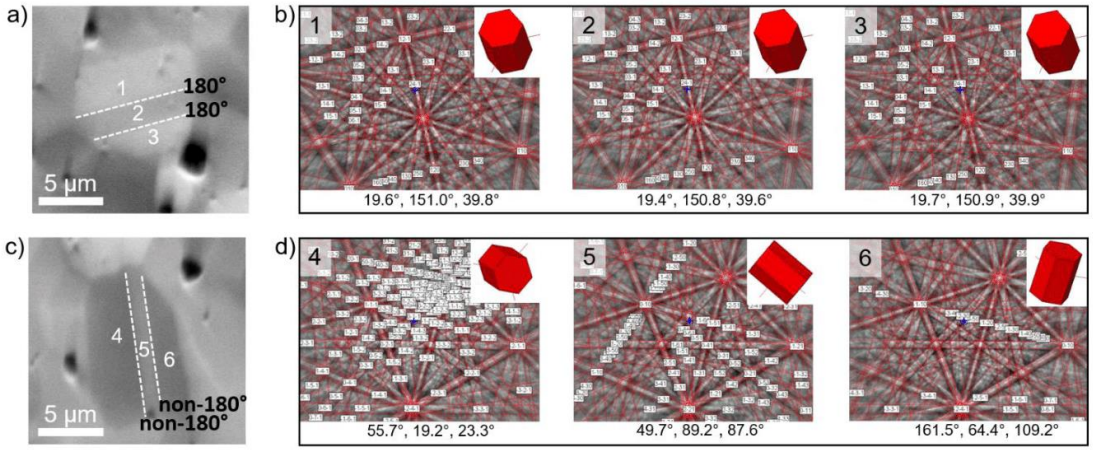

Figure S2: Analysis of the relative orientations of the domains was performed by EBSD to determine the types of DWs in the BFO ceramics. The *R*3*c* space group was used for indexing the patterns. The $[0001]_{hex}$ direction in the hexagonal setting is equivalent to the $[111]_{pc}$ direction in a pseudo-cubic representation, which is also the direction of spontaneous polarization for BFO [4]. a) and c) show grains containing two DWs each (dashed lines). b) and d) show the Kikuchi patterns obtained in domains marked 1, 2, 3 and 4, 5, 6 in a and c, respectively, together with the Euler angles corresponding to each orientation. The orientation relationship between two neighboring domains was determined by rotation of domain coordinate system to the initial sample coordinate system using the transposed rotation matrix g [5],

$$g = \begin{vmatrix} \cos\varphi_1\cos\varphi_2 - \sin\varphi_1\sin\varphi_2\cos\Phi & \sin\varphi_1\cos\varphi_2 + \cos\varphi_1\sin\varphi_2\cos\Phi & \sin\varphi_2\sin\Phi \\ -\cos\varphi_1\sin\varphi_2 - \sin\varphi_1\cos\varphi_2\cos\Phi & -\sin\varphi_1\sin\varphi_2 + \cos\varphi_1\cos\varphi_2\cos\Phi & \cos\varphi_2\sin\Phi \\ \sin\varphi_1\sin\Phi & -\cos\varphi_1\sin\Phi & \cos\Phi \end{vmatrix}$$

where φ_1, Φ, φ_2 are Euler angles.

Based on the results, we conclude that both 180° DWs and non-180° DWs (Fig. S2a and Fig. S2c) are present in the BFO ceramic.

S3. Reduced Young's modulus of a BFO grain measured with Peakforce Quantitative Nanomechanical Mapping

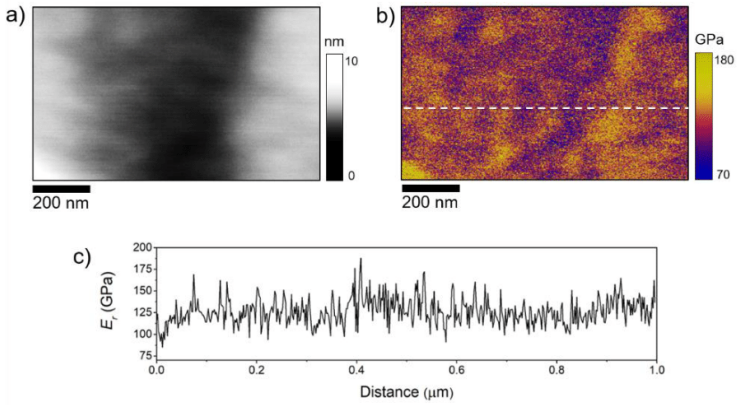

Figure S3: E_r of the BFO matrix was estimated using an atomic force microscopy-based technique, i.e. Peakforce Quantitative Nanomechanical Mapping [6] of higher spatial resolution. In a) we show the topography of a selected grain and in b) the mapping of E_r in the same area. c) Shows the line profile of E_r over the region of interest (dashed line in b), from which an average value of (126.2 ± 15.1) GPa was calculated. The E_r measured with Peakforce Quantitative Nanomechanical Mapping is close to the value measured with nanoindentation and thus supports the nanoindentation results, although the error of E_r in Peakforce Quantitative Nanomechanical Mapping is larger compared to nanoindentation.

S4. Mechanical properties of the iron-rich phase

a)

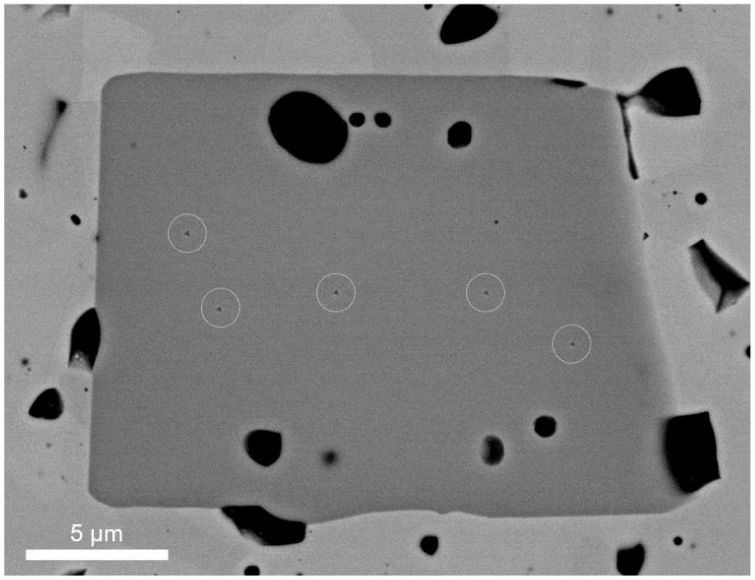

b)

	E_r (GPa)	H (GPa)
Iron-rich phase	128.7 ± 6.8	9.3 ± 0.5
BFO (500 µN)	113.5 ± 5.7	7.8 ± 0.5

Figure S4: E_r and H of the iron-rich phase were measured to determine their influence on the development of E_r and H of BFO. A total of 11 measurements were made on 3 iron-rich phases. a) An example of 5 indentations (circled) made on an iron-rich phase with a peak force of 500 µN. b) Comparison of the average E_r and H of the iron-rich phase and BFO at 500 µN, showing that the iron-rich phase has higher E_r and H compared to BFO.

S5. Mechanical properties of domain walls

a)

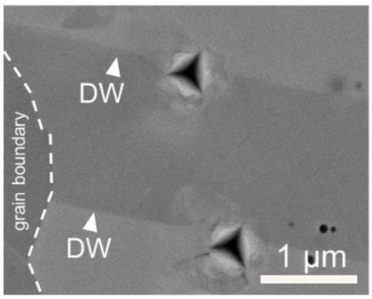

b)

	E_r (GPa)	H (GPa)
DWs	110.1 ± 4.2	8.3 ± 0.3
BFO (1 mN)	110.0 ± 6.0	8.1 ± 0.6

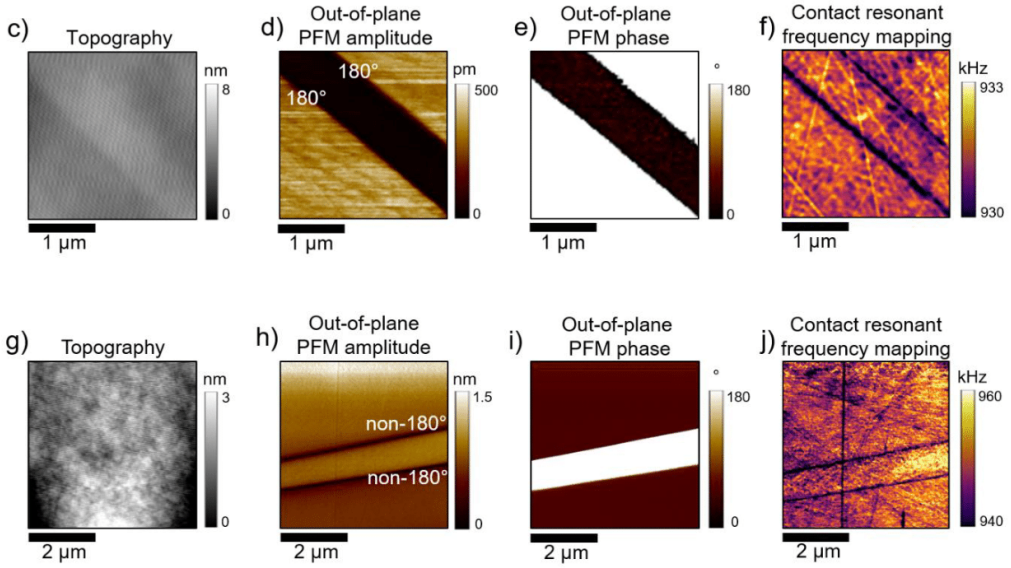

Figure S5: During the nanoindentation measurements at 1 mN, 6 out of 28 indentations were made on DWs. Figure a shows an example of two 1-mN indentations on DWs. The DWs can be seen in the BSE image as interphases between alternating contrast within the grain. There is both experimental [7–10] and theoretical [11] evidence that the DWs might have different mechanical properties than the surrounding matrix, while our indentation measurements did not show any statistically significant differences in H and E_r measured on the DWs and within the materials matrix (figure b). Due to the almost atomic-level structure of the DWs, the indentation measurements, even when performed on DWs, were still dominated by the properties of the matrix. Only by using AFM-derived techniques, were we able to observe DWs with a lower E_r

compared to the BFO matrix throughout the BFO sample. Figures c-f and figures g-j show an example of a pair of mechanically softer 180° and a pair of mechanically softer non-180° DWs, respectively (the type of DWs was determined using EBSD as described in Figure S2). Using PFM, we first identified the DWs as interfaces between regions with different out-of-plane PFM amplitude and phase in a region with minimal topographic features at the DWs, as shown in figures c-e and g-i in the topography. The same regions were then scanned again with CRFM, where we observed a decrease in the contact resonance frequency at the DWs, shown in figure f and j, which directly correlates with the decrease in E_r. According to the literature, there are several contributions to the observed softness, such as the topography effect [11], which we eliminated as much as possible by probing the DWs in topographically homogeneous regions (figure c and g), but also the absolute direction of the spontaneous polarization [9,10], depolarization due to electromechanical coupling [9], defects that might be segregated at the DWs [8,9], and, finally, the decrease in E_r on the DWs might be related to the reversible movements of the DWs under the AFM probe [9,11].

S6. Cross-sectional view of an undeformed region

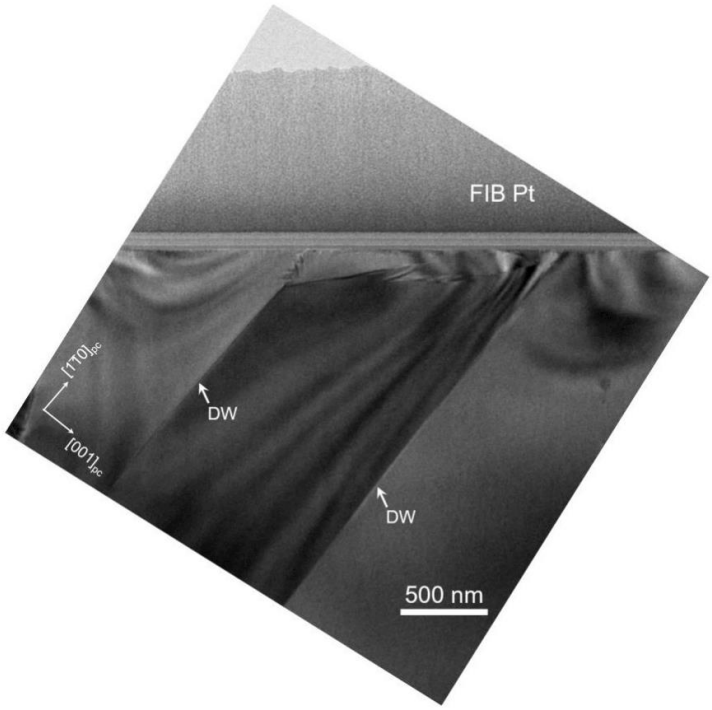

Figure S6: A near-surface TEM image of an undeformed grain of BFO in $[110]_{pc}$ zone axis, where no dislocations were found. The only defects observed were DWs (indicated by arrows), which have a lamellar morphology, as already observed in the SEM characterization.

S7: TEM of the area beneath a 1 mN indentation on a DW

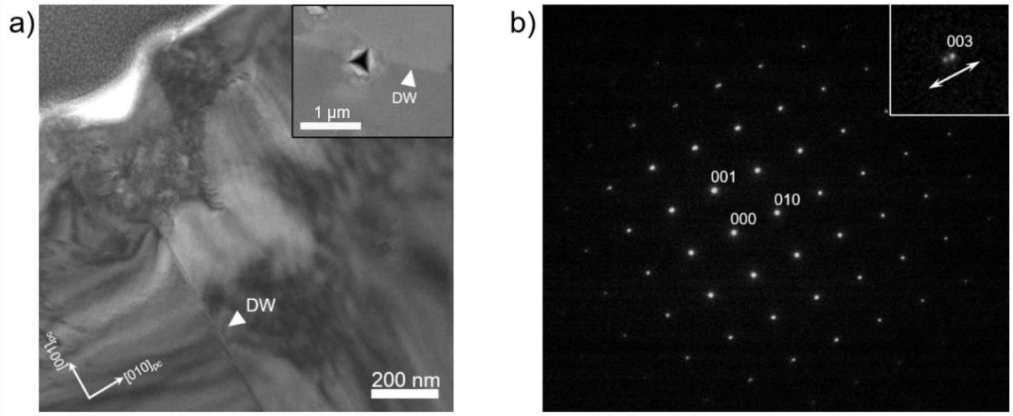

Figure S7: a) TEM image of the area beneath a 1-mN indentation presented in Figure 3a of the main text. Below the zone of the plastic deformation, a DW parallel to the $(001)_{pc}$ planes is observed. The inset shows the SEM image of the same indentation prior to the lamella preparation; b) Selected-area electron diffraction taken in the region below the plastic deformation zone, i.e. at the DW, showing splitting of the reflections in the $[010]_{pc}$ direction (inset).

Based on the DW position, the splitting direction of the reflections in the diffraction pattern, and assuming DW neutrality, we identify the observed DW as a 109° DW [12].

S8. Strains around the crack tip

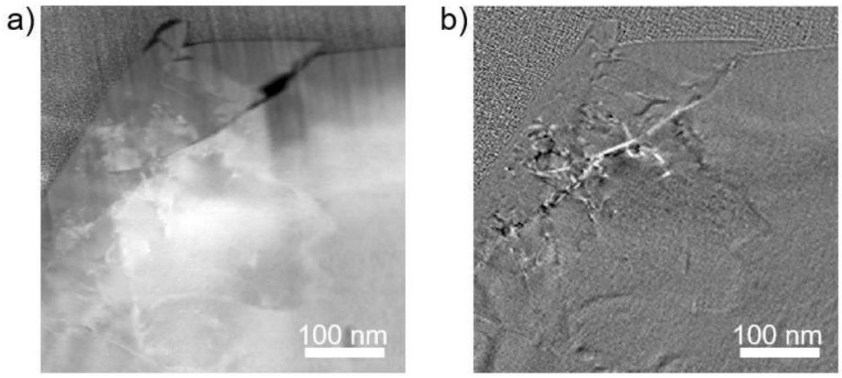

Figure S8: a) Virtual dark-field image of the deformed surface under a 2-mN indentation, created from a 4D-STEM dataset; b) Corresponding divergence map using the center of mass, where higher contrasts represent higher local strains. The strains appear to be distributed in the region between the crack tip and indented surface.

References

[1] T. Rojac, A. Bencan, B. Malic, G. Tutuncu, J.L. Jones, J.E. Daniels, D. Damjanovic, $BiFeO_3$ ceramics: Processing, electrical, and electromechanical properties, J. Am. Ceram. Soc. 97 (2014) 1993–2011. https://doi.org/10.1111/jace.12982.

[2] M.S. Bernardo, T. Jardiel, M. Peiteado, A.C. Caballero, M. Villegas, Reaction pathways in the solid state synthesis of multiferroic $BiFeO_3$, J. Eur. Ceram. Soc. 31 (2011) 3047–3053. https://doi.org/10.1016/j.jeurceramsoc.2011.03.018.

[3] S.M. Selbach, M.A. Einarsrud, T. Grande, On the Thermodynamic Stability of $BiFeO_3$, Chem. Mater. 21 (2009) 169–173. https://doi.org/10.1021/cm802607p.

[4] J.G. Park, M.D. Le, J. Jeong, S. Lee, Structure and spin dynamics of multiferroic $BiFeO_3$, J. Phys. Condens. Matter. 26 (2014). https://doi.org/10.1088/0953-8984/26/43/433202.

[5] H.-J. Bunge, Texture Analysis in Materials Science, Butterworth & Co, 1982. https://doi.org/https://doi.org/10.1016/C2013-0-11769-2.

[6] Bruker Corporation, PeakForce QNM User Guide, (2011). https://mmrc.caltech.edu/AFM Dimension Icon/Bruker Training/004-1036-000 PEAKFORCE QNM USERS GUIDE-F.pdf.

[7] T. Tsuji, H. Ogiso, J. Akedo, S. Saito, K. Fukuda, K. Yamanaka, Evaluation of domain boundary of piezo/ferroelectric material by ultrasonic atomic force microscopy, Japanese J. Appl. Physics, Part 1 Regul. Pap. Short Notes Rev. Pap. 43 (2004) 2907–2913. https://doi.org/10.1143/JJAP.43.2907.

[8] T. Tsuji, S. Saito, K. Fukuda, K. Yamanaka, H. Ogiso, J. Akedo, Y. Kawakami, Significant stiffness reduction at ferroelectric domain boundary evaluated by ultrasonic atomic force microscopy, Appl. Phys. Lett. 87 (2005) 1–4. https://doi.org/https://doi.org/10.1063/1.2012537.

[9] C. Stefani, L. Ponet, K. Shapovalov, P. Chen, E. Langenberg, D.G. Schlom, S. Artyukhin, M. Stengel, N. Domingo, G. Catalan, Mechanical Softness of Ferroelectric 180° Domain Walls, Phys. Rev. X. 10 (2020) 41001. https://doi.org/https://doi.org/10.1103/PhysRevX.10.041001.

[10] C.P.T. Nguyen, P. Schoenherr, J. Seidel, Intrinsic Mechanical Compliance of 90°

Domain Walls in $PbTiO_3$, Adv. Funct. Mater. 33 (2023). https://doi.org/10.1002/adfm.202211906.

[11] X. He, X. Ding, J. Sun, G.F. Nataf, E.K.H. Salje, Elastic softening and hardening at intersections between twin walls and surfaces in ferroelastic materials, APL Mater. 11 (2023). https://doi.org/10.1063/5.0159836.

[12] S. Mantri, J. Daniels, Domain walls in ferroelectrics, J. Am. Ceram. Soc. 104 (2021) 1619–1632. https://doi.org/10.1111/jace.17555.

Chapter 5

Elastic Properties of Domains and Domain Walls in $(K_{0.5}Na_{0.5})NbO_3$ Single Crystal

The study investigates the variation of the elastic properties of the domain structure on the part of the orthorhombic crystal $(K_{0.5}Na_{0.5})NbO_3$ consisting of only ferroelastic DWs, namely 90° DWs and 60° DW, using AFM techniques dedicated for the evaluation of elasticity. Variations in elasticity were observed by passing over different domains and DWs.

Differently oriented domains showed an elastic anisotropy, but a direct link between the elastic properties and the P_s direction was not established due to the complexity of determining the P_s orientation in the orthorhombic structure.

The 90° DWs were found to be elastically softer on one side of the domain, i.e., have a higher E_r, while they are elastically harder on the other side. The difference in the elasticity of domains and DWs was about ± 20 %. A similar trend in the elasticity of ferroelastic DWs was also observed by molecular dynamics, but with a much smaller variation in elasticity of ± 0.7 % [78], which was attributed as intrinsic elasticity solely to the stress/strain on the DWs.

It is assumed that the difference between the modeling and the experimental measurements with the AFM arises from additional extrinsic contributions, such as reduced or absent piezoelectricity of the DW, which makes it appear elastically softer, and the depolarizing field in the adjacent domain due to the piezoelectric effect when the AFM probe presses on the domains. If depolarizing fields are not properly screened, they can make the domains appear elastically harder, resulting in the DWs appearing softer compared to the neighboring domains.

Interestingly, no elastic contrast was observed at 60° DW, which could be attributed to an unfavorable orientation of the crystals, similar to what has already been reported for 180° and 90° DW [19], [20].

This chapter addresses the objective 3 and hypotheses 6 and 7.

Published in: K. Žiberna, M. Koblar, A. Bradeško, M. Bah, F. Levassort G. Dražić, H. Uršič and A. Benčan, "Elastic properties of domains and domain walls in $(K_{0.5}Na_{0.5})NbO_3$ single crystal", *Journal of the European Ceramic Society,* **45**, 117566, 2024, https://doi.org/10.1016/j.jeurceramsoc.2025.117566.

My contribution: I prepared the sample and performed dual resonance AC tracking PFM, CRFM, TEM, SAED, nanoindentation and analyzed the data. Together with the co-authors, we interpreted the data, elaborated the concept of the manuscript, and wrote the paper.

Journal of the European Ceramic Society 45 (2025) 117566

Contents lists available at ScienceDirect

Journal of the European Ceramic Society

journal homepage: www.elsevier.com/locate/jeurceramsoc

Elastic properties of domains and domain walls in $(K_{0.5}Na_{0.5})NbO_3$ single crystal

Katarina Žiberna [a,b,*], Maja Koblar [a], Andraž Bradeško [a], Micka Bah [c], Franck Levassort [c], Goran Dražić [d], Hana Uršič [a,b], Andreja Benčan [a,b,*]

[a] Electronic Ceramics Department, Jožef Stefan Institute, Ljubljana 1000, Slovenia
[b] Jožef Stefan International Postgraduate School, Ljubljana 1000, Slovenia
[c] GREMAN UMR7347, Université de Tours, CNRS, INSA CVL, Tours 37071, France
[d] Department of Materials Chemistry, National Institute of Chemistry, Ljubljana 1000, Slovenia

ARTICLE INFO

Keywords:
Elasticity
Ferroelectrics
Potassium sodium niobite
Domains
Domain walls

ABSTRACT

The elastic properties of ferroelectric materials at the nanoscale are intricate, with domains and domain walls each having their own distinct elasticity – a property which can be exploited for tailoring materials performance. In this study, we report on the elastic response of the ferroelectric domain structure of a $(K_{0.5}Na_{0.5})NbO_3$ single crystal, measured using an atomic force microscopy-based techniques. Before mapping the elastic properties, the domain structure was characterized using piezo-response force microscopy and transmission electron microscopy. The average measured reduced elastic modulus was ~130 GPa. The 90° domain walls exhibit a 20 % difference in the reduced modulus, appearing elastically harder on one side of the domain and elastically softer on the other. In contrast, 60° domain walls showed no mechanical contrast with the neighboring domains. Anisotropy in elasticity was also observed between domains with different piezoelectric activity.

1. Introduction

Distinct properties of domain walls (DWs) in ferroelectric materials are one of the key aspects driving their research for use in nanotechnological applications [1]. The structural differences between these quasi-2-D defects and the domains they separate give rise to a variety of properties that differ in bulk, such as altered electrical properties like increased conductivity [2,3].

A far less investigated property are DWs' mechanical characteristics. The nanometric width of DWs, poses a challenge in mechanical testing, and limits the number of techniques to a selected few, possessing high enough spatial resolution and the ability to measure mechanical properties. Most commonly used are atomic force microscopy (AFM)-based techniques, i.e., ultrasonic AFM, acoustic AFM, force-distance curves, offering non-destructive measurements of elastic properties at the nanoscale level, as well as the study of stress induced nanoscale phenomena [4].

DWs separate domains of different direction of the ferroelectric polar order called spontaneous polarization ($\vec{P_s}$). Depending on the symmetry of the ferroelectric phase, several different types of DWs can be found in the material, which can be classified by the angle formed between the $\vec{P_s}$ vectors in two neighboring domains, and can have different elastic properties. 180° DWs were reported to be elastically softer, i.e. have a lower elastic modulus, than the adjacent domains in periodically poled lithium niobate, $BaTiO_3$ and $PbTiO_3$ [5–7]. The elastic softening of 10–20 % was found to be independent of the morphology and composition of the samples. Interestingly, elastic softening was only observed for 180° DWs separating domains with out-of-plane $\vec{P_s}$, i.e. domains with $\vec{P_s}$ perpendicular to the sample's surface, while 180° DWs separating domains with in-plane $\vec{P_s}$, domains where $\vec{P_s}$ lies parallel to the sample surface, showed no elastic contrast. In addition, anisotropy between different domains was reported in $BaTiO_3$ and $PbTiO_3$. The in-plane domains exhibited higher elastic modulus compared to the out-of-plane domains, which highlights the importance of the absolute direction of $\vec{P_s}$ [7,8].

90° DWs in $PbTiO_3$ which are, in addition to being ferroelectric, also ferroelastic, with valley and ridge topography were observed to have a higher or a lower modulus than the adjacent domains. The variations of the modulus occured only when the $\vec{P_s}$ of one of the neighboring

* Corresponding authors at: Electronic Ceramics Department, Jožef Stefan Institute, Ljubljana 1000, Slovenia.
E-mail addresses: katarina.ziberna@ijs.si (K. Žiberna), andreja.bencan@ijs.si (A. Benčan).

https://doi.org/10.1016/j.jeurceramsoc.2025.117566
Received 18 December 2024; Received in revised form 25 April 2025; Accepted 26 May 2025
Available online 27 May 2025

domains was pointing out-of-plane (*a*-*c* DWs) [8,9].

The cause for the distinct mechanical DW behavior is still not clear. Some proposed contributions include defects segregated at the DWs [6,9], topography changes associated with twinning [8,9], DW tilt [8], strain states at different DWs [8], depolarization fields created by AFM tip pressure at the DW [7] and local DW movements at the surface under the AFM tip of both ferroelectric and ferroelastic DWs that result in elastic softening of the material [7]. The latter contribution can be especially concerning, as it can mask the intrinsic elastic hardening due to DW motion [9].

The different elastic properties of DWs have already attracted interest and suggestions have been made as to where this phenomenon could be exploited, for example they could be utilized to modulate thermal conductivity through the bulk [7,9–11]. At the surface, these properties could enable the mechanical detection of DWs in highly conductive materials where traditional probing methods are ineffective [7]. Additionally, in life sciences, the ability to control surface elasticity could influence bacterial adhesion, which is known to depend on the elastic properties of the surface [9]. Furthermore, domain engineering can be used to produce a material with a favorable modulus of elasticity by exploiting the elastic anisotropy of the differently oriented domains.

$(K_{0.5}Na_{0.5})NbO_3$ (KNN) and KNN-based compositions are investigated as potential lead-free alternatives to Pb(Zr, Ti)O_3-based ferroelectrics, not only due to the comparable piezoelectric activity and higher Curie temperature of 420 °C [12], but also because of the higher elastic modulus, which makes KNN and its derivatives more suitable for ultrasonic applications [13].

Here we look at the local elastic properties of domains and DWs in a KNN single crystal prepared by solid-state crystal growth [14,15] using Peak Force Quantitative NanoMechanical mapping (PF-QNM). Prior to mapping the elastic properties, the domain structure was characterized using a combination of off-resonance vector piezo-response force microscopy (PFM), cross-sectional transmission electron microscopy (TEM) and crystallographic orientation mapping.

2. Methods

The KNN sample prepared by solid-state crystal growth [14,15] was cut, polished with SiC grading papers and 3-μm and 0.25-μm diamond paste. To achieve a mirror-like surface finish and remove near-surface defects caused by mechanical polishing, the sample was additionally polished with colloidal silica for 2 hours. The polished surface was determined to be close to the (100) plane according to electron backscattered diffraction (EBSD) (Supplementary Materials, S1). EBSD and transmission Kikuchi diffraction (TKD) were performed in a scanning electron microscope Apreo 2 S (Thermo Fischer Scientific, Waltham, MA, USA) equipped with an EBSD analyzer C-Swift (Oxford Instruments, Abingdon, UK) at 30 kV. For EBSD, the sample was tilted at 70°, while for TKD the transparent sample was tilted for −20°. The diffraction patterns were indexed with the space group *Bmm*2 [16] in the AZtecCrystal program (Oxford Instruments, Abingdon, UK). The difference in orientation between two neighboring domains were determined by rotation of the coordinate system of one domain to the coordinate system of the neighboring domain using the transposed rotation matrix [17,18].

The off-resonance vector PFM mappings were done with a Bruker Dimension Icon (Bruker Nano Surfaces, Santa Barbara, CA, USA) using a DDESP-V2 probe coated with doped diamond (Bruker Nano Surfaces, Santa Barbara, CA, USA) with a nominal radius of 100 nm and a cantilever spring constant of 80 N/m. The driving voltage and frequency were 2 V and 15 kHz, respectively, while the scan rate was set to 0.3 Hz.

The PF-QNM was performed in a Bruker Dimension Icon (Bruker Nano Surfaces, Santa Barbara, CA, USA) with a diamond AFM probe DNISP-HS with a cube-corner geometry having a nominal tip radius of 40 nm and a cantilever spring constant of 353 N/m (Bruker Billerica, MA, USA). To gain a quantitative reduced elastic modulus, the deflection sensitivity and the effective tip radius were calibrated on sapphire and fused silica, respectively. The force applied during the measurement was 3 μN. PF-QNM is a tapping technique that makes a force-distance curve at each pixel of the image, allowing the extraction of the elasticity modulus [19].

After PFM and PF-QNM, a transparent lamella was prepared from the region of interest using a gallium source focused ion beam Helios Nanolab 650 HP (Thermo Fischer Scientific, Waltham, MA, USA). The bright field TEM images and the selected area electron diffractions (SAED) were acquired on a JEM 2100 (Jeol, Tokyo, Japan) operated at 200 kV.

3. Results and discussion

The 12 possible directions of $\vec{P_s}$ in KNN along $[110]_{pc}$ can give rise to four types of DWs, 180°, 120°, 90° and 60° DWs [20]. The domain structure can thus be fairly complex, composed of herringbone [21–24], watermarks [21–23] and zig-zag [23–25] patterns.

Fig. 1 presents the domain structure in the region of interest, probed using vector PFM, with a measured surface roughness of 1.6 nm (Fig. 1a). The domain structure consists of larger lamellar domains of approximately 2–2.5 μm in width (Fig. 1b-e, yellow arrows) with a substructure of smaller lamellar domains of less than 1 μm in width (Fig. 1b-e, white arrows) that extend over the larger domains.

Fig. 1b-e shows two components of the $\vec{P_s}$, the out-of-plane component (P_z) and one in-plane component (P_y), revealing a complex piezoelectric activity. The in-plane signal (Fig. 1b, c) of the larger domains appears to change the polar direction over the DW (marked with yellow arrows), while the out-of-plane component of $\vec{P_s}$ (Fig. 1d, e) does not change neither amplitude nor direction, which is indicative of non-180° DWs.

The smaller domains (marked with white arrows), however, have no PFM in-plane phase signal and zero in-plane amplitude signal (Fig. 1b, c). Once the smaller domains cross DWs separating the larger domains (marked with yellow arrows), the out-of-plane amplitude and phase change (Fig. 1d, e), indicating that the out-of-plane component of $\vec{P_s}$ changes directions, but not for 180° as the out-of-plane amplitude is different in the neighboring domains.

In cross-section, i.e., in the direction roughly perpendicular to the sample's surface, the regions of interest's domain structure appeared to have a zig-zag pattern (Fig. 2a). We have identified the domains that are inclined by about 10° with respect to the surface (Fig. 2a) as the larger domains highlighted with yellow arrows in Fig. 1. The smaller domains, marked with white arrows in Fig. 1, were observed to intersect the larger domains in a zig-zag-like fashion.

According to TEM and TKD (Fig. 2a, b, respectively), the DWs separating larger domains parallel to $(100)_{pc}$ planes are 90° DWs (Fig. 2a, yellow arrows), while DWs separating smaller domains (Fig. 2a, white arrows), are either 60° or 120° DWs, which cannot be separated during orientation indexing [17]. In addition, the DWs confining the smaller domains are not parallel to one of the expected $(110)_{pc}$ planes, suggesting their type is either uncharged 60° DW or charged 120° DWs, as they can occupy a random plane defined by the piezoelectric and electrostatic coefficients of the material [26].

The results are in line with the PFM analysis (Fig. 1). Assuming the favorable formation of neutral DWs, we conclude that the larger domains are thus separated by 90° DWs, while the smaller domains are separated by 60° DWs. This conclusion is further supported by comparing experimental SAED patterns over these DWs with the simulated ones, with the domain structure sketch provided in the Supplementary Materials (Supplementary Materials, S2).

Fig. 3 shows the map of the reduced elastic modulus for the same region of interest as in Fig. 1, obtained using PF-QNM, a technique based on the same principles as those previously used to probe the elastic properties of both domains and DWs [8]. The average value of the

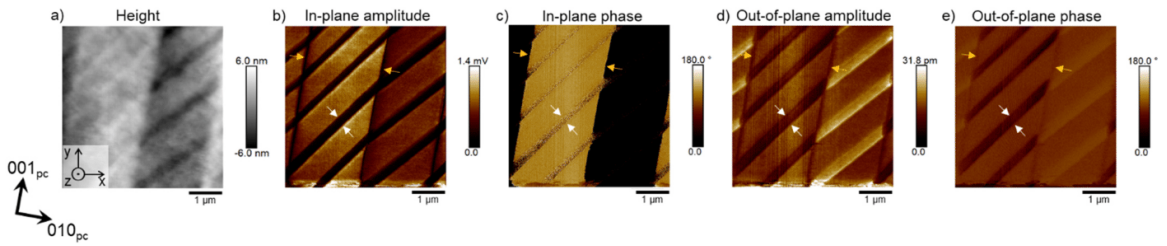

Fig. 1. PFM of the region of interest in the KNN single crystal: a) topography, b) in-plane PFM amplitude, c) in-plane PFM phase, d) out-of-plane PFM amplitude, e) out-of-plane PFM phase. Yellow and white arrows point to domain with similar morphology.

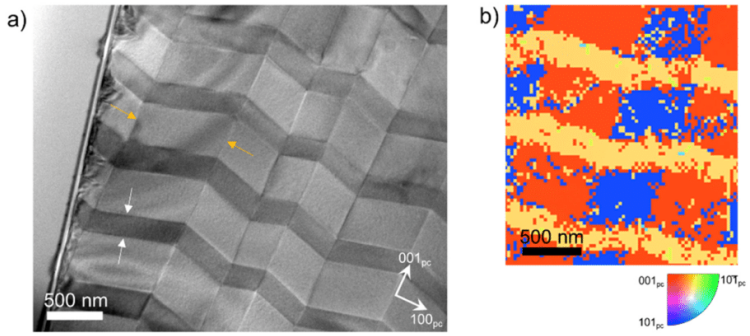

Fig. 2. a) TEM image of the KNN domain structure in cross-section. The yellow and white arrows mark the same types of domain as in Fig. 1; b) Filtered TKD orientation map of a part of the image in a and the corresponding inverse-pole figure legend. The TKD patterns were indexed with the space group *Bmm*2 [16] in the orthorhombic metric, which was then converted into pseudocubic notations.

reduced modulus obtained from the image is ~130 GPa, which agrees well with the reduced elastic modulus determined using nano-indentation (Supplementary Materials, S3). The three line profiles of the reduced modulus, along with the height profile, were extracted to see the correlation between the reduced modulus and changes in polarity direction in KNN (Fig. 1). One line profile was taken over a larger domain separated by 90° DWs (Fig. 3, labeled I) and two taken perpendicular over smaller domains separated by 60° DWs (Fig. 3, labeled II and III).

The line profile taken perpendicular to the 90° DWs separating larger domains (Fig. 3, label I) shows a significant variation in the reduced modulus on DWs separating larger domains. The variation of the modulus measured in between the DW of ± 4 % is regarded as noise. Interestingly, on one side of the domain, the DW exhibits a reduced modulus which is lower than that measured within domains, while on the opposite side, the DW shows a higher reduced modulus (Fig. 3, yellow arrows). The difference in the elastic modulus between the domains and DWs is approximately ± 20 %, which aligns well with other experimental measurements where differences up to ~28 % were observed between domains and DWs [8]. Additionally, the elastic softening and hardening effects were observed to extend over ~100 nm into the domain, likely due to the interactions between DWs and the surface, which may alter the stress/strain states and result in widening of the DW at the surface [27]. The widening can also be explained by the inclination of the DW relative to the surface, i.e., the DW not being measured edge on.

Based on the literature, the measured elastic contrast at the DWs can result from a combination of intrinsic elastic properties of DWs and extrinsic contributions. First, we rule out topographical effects, as in our case, surface variations are minimal, with gradual, non-abrupt changes ranging from 0.5 nm to 1.5 nm (Fig. 3 and Supplementary Materials, S4). Second, we exclude DW motion as a contributing factor, since such motion would uniformly soften the elastic response of all DWs, regardless of their intrinsic properties [7,9].

The intrinsic elastic response of 90° DWs is likely linked to variations in strain states at the as suggested by He et al., who, using molecular dynamics simulation, observed a slight variation (± 0.7 %) in the elastic modulus at ferroelastic 90° DWs with ridge and valley topography. [9]. As our material is ferroelectric, the 90° DWs investigated are in addition to being ferroelastic, also ferroelectric in character. The continuous change of $\vec{P_s}$ across the DWs may contribute to the measured elasticity through electromechanical effects triggered by the inhomogeneous stress fields under the AFM probe. Additionally, the favorable orientation of the surrounding domains plays a crucial role in detecting the DWs elastically. Specifically, when the adjacent domains have an out-of-plane $\vec{P_s}$ component, the DWs can be observed in elasticity measurements. In contrast, if the DWs were confined between purely in-plane $\vec{P_s}$ domains, their elastic contrast would not be detectable [7,8].

For the smaller domains (Fig. 3, labels II and III), a decrease in the reduced modulus of approximately 10–20 % was observed compared to the neighboring domains. The difference is likely due to a different direction of $\vec{P_s}$ within domains, similarly to what has been observed in ferroelectrics with a structure of higher symmetry, namely tetragonal $BaTiO_3$ and $PbTiO_3$. In these materials, the direction of $\vec{P_s}$ was directly correlated with the elastic modulus, where domains with out-of-plane $\vec{P_s}$ exhibit a lower elastic modulus than those with in-plane $\vec{P_s}$ [7,8,28]. However, due to the lower symmetry of the orthorhombic structure compared to the tetragonal structure, the elastic anisotropy of KNN is more complex, as shown in Figure S5 [29]. This complexity is especially pronounced when measurements are taken along non-low-zone axes, making it challenging to interpret the $\vec{P_s}$ direction solely based on the reduced elastic modulus.

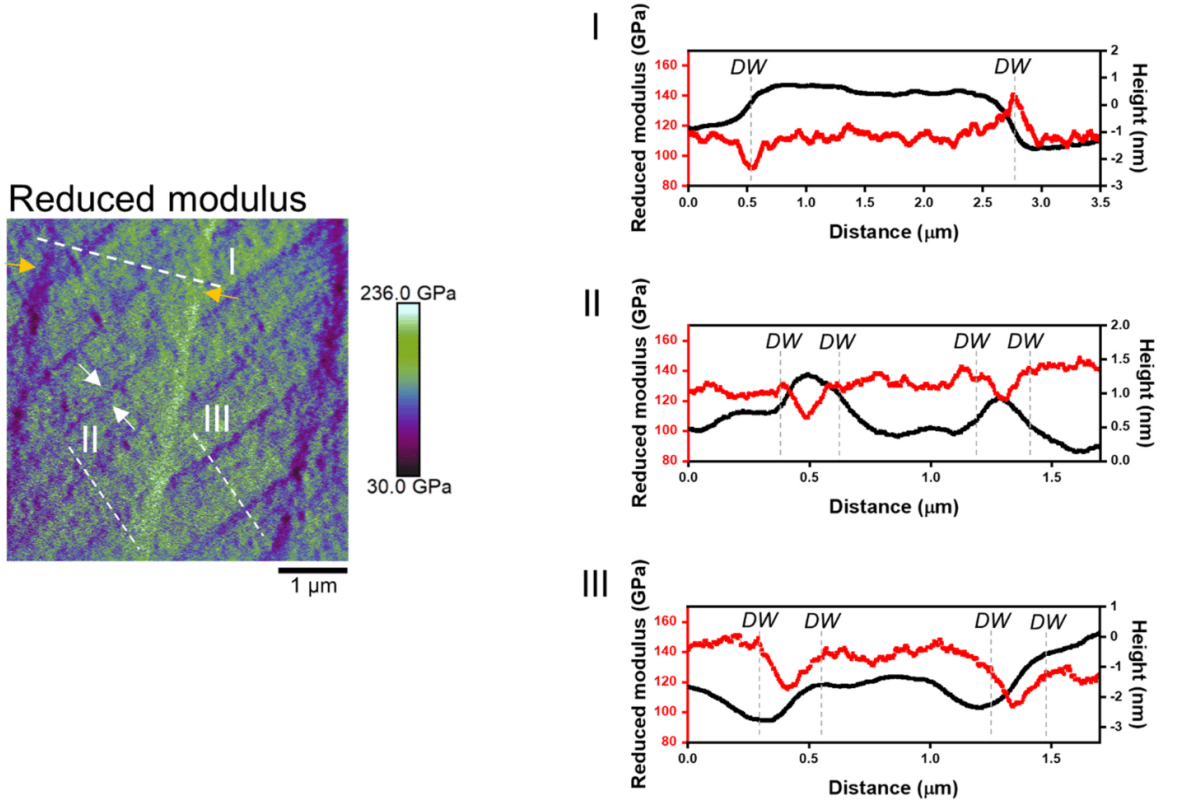

Fig. 3. Map of the reduced elastic modulus with line profiles taken over a larger domain (I) and smaller domains (II, III) accompanied by the height profiles. The positions of the DWs in the line profiles were determined from the PFM images in Fig. 1 and are marked by grey dashed lines.

The 60° DWs confining these smaller domains show no distinct elastic contrast. Although for 90° DWs mainly stress and strain are discussed as the main causes of their pronounced elastic response [8,9], in reality many properties such as structure and morphology, in addition to strain, contribute to their elastic response through electromechanical and mechanical contributions and are needed to determine the origin of the particular elasticity at the DWs.

4. Conclusions

In summary, this work shows the complex elastic response of KNN at the nanoscale. For the first time, the elastic properties in KNN were measured over 90° and 60° DWs, where 90° DWs show an increase in elasticity from the average reduced modulus of 130 GPa on one side of the domain and a decrease on the other side, while 60° DW shows no elastic contrast. Furthermore, anisotropy of the reduced elastic modulus was observed across domains with different piezoelectric activity. The orthorhombic symmetry does not allow for a straightforward interpretation of the $\vec{P_s}$ direction based on the elastic modulus, as is possible with tetragonal ferroelectrics.

CRediT authorship contribution statement

Andraž Bradeško: Writing – review & editing, Investigation, Formal analysis, Data curation. **Franck Levassort:** Writing – review & editing, Investigation, Funding acquisition. **Micka Bah:** Writing – review & editing, Investigation, Formal analysis, Data curation. **Maja Koblar:** Writing – review & editing, Investigation, Formal analysis. **Katarina Žiberna:** Writing – original draft, Visualization, Validation, Investigation, Formal analysis, Data curation, Conceptualization. **Hana Uršič:** Writing – review & editing, Validation, Investigation, Funding acquisition, Conceptualization. **Goran Dražić:** Writing – review & editing, Investigation. **Andreja Benčan:** Writing – review & editing, Validation, Supervision, Resources, Project administration, Investigation, Funding acquisition, Conceptualization.

Declaration of Competing Interest

The authors declare that they have no known competing financial interests or personal relationships that could have appeared to influence the work reported in this paper.

Acknowledgement

This work is supported by the Slovenian Research and Innovation Agency through core funding (project P2–0105), national postgraduate funding (project PR-10481), project J7–4637 and bilateral project BI-FR/22–23-PROTEUS-10. Val Fišinger is acknowledged for the help with the atomic force microscope.

Appendix A. Supporting information

Supplementary data associated with this article can be found in the online version at doi:10.1016/j.jeurceramsoc.2025.117566.

References

[1] D. Meier, S.M. Selbach, Ferroelectric domain walls for nanotechnology, Nat. Rev. Mater. 7 (2022) 157–173, https://doi.org/10.1038/s41578-021-00375-z.
[2] J. Seidel, L.W. Martin, Q. He, Q. Zhan, Y.H. Chu, A. Rother, M.E. Hawkridge, P. Maksymovych, P. Yu, M. Gajek, N. Balke, S.V. Kalinin, S. Gemming, F. Wang, G. Catalan, J.F. Scott, N.A. Spaldin, J. Orenstein, R. Ramesh, Conduction at domain walls in oxide multiferroics, Nat. Mater. 8 (2009) 229–234, https://doi.org/10.1038/nmat2373.
[3] T. Rojac, A. Bencan, G. Drazic, N. Sakamoto, H. Ursic, B. Jancar, G. Tavcar, M. Makarovic, J. Walker, B. Malic, D. Damjanovic, Domain-wall conduction in ferroelectric $BiFeO_3$ controlled by accumulation of charged defects, Nat. Mater. 16 (2017) 322–327, https://doi.org/10.1038/nmat4799.
[4] Y. Heo, P. Sharma, Y.Y. Liu, J.Y. Li, J. Seidel, Mechanical probing of ferroelectrics at the nanoscale, J. Mater. Chem. C. 7 (2019) 12441–12462, https://doi.org/10.1039/c9tc02661d.
[5] T. Tsuji, H. Ogiso, J. Akedo, S. Saito, K. Fukuda, K. Yamanaka, Evaluation of domain boundary of piezo/ferroelectric material by ultrasonic atomic force microscopy, Jpn. J. Appl. Phys., Part 1 Regul. Pap. Short. Notes Rev. Pap. 43 (2004) 2907–2913, https://doi.org/10.1143/JJAP.43.2907.
[6] T. Tsuji, S. Saito, K. Fukuda, K. Yamanaka, H. Ogiso, J. Akedo, Y. Kawakami, Significant stiffness reduction at ferroelectric domain boundary evaluated by ultrasonic atomic force microscopy, Appl. Phys. Lett. 87 (2005) 071909, https://doi.org/10.1063/1.2012537.
[7] C. Stefani, L. Ponet, K. Shapovalov, P. Chen, E. Langenberg, D.G. Schlom, S. Artyukhin, M. Stengel, N. Domingo, G. Catalan, Mechanical softness of ferroelectric 180° domain walls, Phys. Rev. X. 10 (2020) 41001, https://doi.org/10.1103/PhysRevX.10.041001.
[8] C.P.T. Nguyen, P. Schoenherr, J. Seidel, Intrinsic mechanical compliance of 90° domain walls in $PbTiO_3$, Adv. Funct. Mater. 33 (2023) 2211906, https://doi.org/10.1002/adfm.202211906.
[9] X. He, X. Ding, J. Sun, G.F. Nataf, E.K.H. Salje, Elastic softening and hardening at intersections between twin walls and surfaces in ferroelastic materials, APL Mater. 11 (2023) 071114, https://doi.org/10.1063/5.0159836.
[10] J.F. Ihlefeld, B.M. Foley, D.A. Scrymgeour, J.R. Michael, B.B. McKenzie, D. L. Medlin, M. Wallace, S. Trolier-Mckinstry, P.E. Hopkins, Room-temperature voltage tunable phonon thermal conductivity via reconfigurable interfaces in ferroelectric thin films, Nano Lett. 15 (2015) 1791–1795, https://doi.org/10.1021/nl504505t.
[11] P.E. Hopkins, C. Adamo, L. Ye, B.D. Huey, S.R. Lee, D.G. Schlom, J.F. Ihlefeld, Effects of coherent ferroelastic domain walls on the thermal conductivity and Kapitza conductance in bismuth ferrite, Appl. Phys. Lett. 102 (2013) 121903, https://doi.org/10.1063/1.4798497.
[12] Y. Saito, H. Takao, T. Tani, T. Nonoyama, K. Takatori, T. Homma, T. Nagaya, M. Nakamura, Lead-free piezoceramics, Nature 432 (2004) 84–87, https://doi.org/10.1038/nature03028.
[13] K. Uchino, Glory of piezoelectric perovskites, Sci. Technol. Adv. Mater. 16 (2015) 46001, https://doi.org/10.1088/1468-6996/16/4/046001.
[14] J.G. Fisher, A. Benčan, M. Kosec, S. Vernay, D. Rytz, Growth of dense single crystals of potassium sodium niobate by a combination of solid-state crystal growth and hot pressing, J. Am. Ceram. Soc. 91 (2008) 1503–1507, https://doi.org/10.1111/j.1551-2916.2008.02324.x.
[15] A. Benčan, E. Tchernychova, M. Godec, J. Fisher, M. Kosec, Compositional and structural study of a $(K_{0.5}Na_{0.5})NbO_3$ single crystal prepared by solid state crystal growth, Microsc. Micro 15 (2009) 435–440, https://doi.org/10.1017/S1431927609090722.
[16] N. Ishizawa, J. Wang, T. Sakakura, Y. Inagaki, K.I. Kakimoto, Structural evolution of $Na_{0.5}K_{0.5}NbO_3$ at high temperatures, J. Solid State Chem. 183 (2010) 2731–2738, https://doi.org/10.1016/j.jssc.2010.09.018.
[17] H.-J. Bunge, Texture Analysis in Materials Science, Butterworth & Co, Berlin, Germany, 1982, https://doi.org/10.1016/C2013-0-11769-2.
[18] K. Žiberna, M. Koblar, M. Bah, F. Levassort, G. Dražić, H. Uršič, A. Benčan, Nanomechanical characterization of $BiFeO_3$ ferroelectric ceramics, J. Eur. Ceram. Soc. 44 (2024) 7025–7031, https://doi.org/10.1016/j.jeurceramsoc.2024.05.011.
[19] A. Kwaśniewska, M. Świetlicki, A. Prószyński, G. Gładyszewski, The quantitative nanomechanical mapping of starch/kaolin film surfaces by peak force afm, Polymers 13 (2021) 244, https://doi.org/10.3390/polym13020244.
[20] S. Mantri, J. Daniels, Domain walls in ferroelectrics, J. Am. Ceram. Soc. 104 (2021) 1619–1632, https://doi.org/10.1111/jace.17555.
[21] F. Rubio-Marcos, A. Del Campo, R. López-Juárez, J.J. Romero, J.F. Fernández, High spatial resolution structure of $(K,Na)NbO_3$ lead-free ferroelectric domains, J. Mater. Chem. 22 (2012) 9714–9720, https://doi.org/10.1039/c2jm30483j.
[22] M. Bah, N. Alyabyeva, R. Retoux, F. Giovannelli, M. Zaghrioui, A. Ruyter, F. Delorme, I. Monot-Laffez, Investigation of the domain structure and hierarchy in potassium-sodium niobate lead-free piezoelectric single crystals, RSC Adv. 6 (2016) 49060–49067, https://doi.org/10.1039/c6ra07205d.
[23] Y. Qin, J. Zhang, W. Yao, C. Wang, S. Zhang, Domain structure of potassium-sodium niobate ceramics before and after poling, J. Am. Ceram. Soc. 98 (2015) 1027–1033, https://doi.org/10.1111/jace.13373.
[24] Y. Qin, J. Zhang, Y. Gao, Y. Tan, C. Wang, Study of domain structure of poled (K, Na)NbO_3 ceramics, J. Appl. Phys. 113 (2013) 204107, https://doi.org/10.1063/1.4807919.
[25] Y.X. Liu, W. Qu, H.C. Thong, Y. Zhang, Y. Zhang, F.Z. Yao, T.N. Nguyen, J.W. Li, M. H. Zhang, J.F. Li, B. Han, W. Gong, H. Wu, C. Wu, B. Xu, K. Wang, Isolated-oxygen-vacancy hardening in lead-free piezoelectrics, Adv. Mater. 34 (2022) 2202558, https://doi.org/10.1002/adma.202202558.
[26] J. Hirohashi, K. Yamada, H. Kamio, M. Uchida, S. Shichijyo, Control of specific domain structure in $KNbO_3$ single crystals by differential vector poling method, J. Appl. Phys. 98 (2005) 034107, https://doi.org/10.1063/1.2001148.
[27] W.T. Lee, E.K.H. Salje, U. Bismayer, Surface structure of domain walls in a ferroelastic system with a domain wall pressure, J. Phys. Condens. Matter 14 (2002) 7901–7910, https://doi.org/10.1088/0953-8984/14/34/308.
[28] D. Torres-Torres, A. Hurtado-Macías, R. Herrera-Basurto, E. Conteras, S. Sánchez, F. Mercader-Trejo, J. González-Hernández, O. Auciello, Anisotropic behavior of mechanical properties for the a- and c-domains in a (001) $BaTiO_3$ single crystal, J. Phys. Condens. Matter 35 (2023) 355703, https://doi.org/10.1088/1361-648X/acda08.
[29] Z. Tan, Y. Peng, J. An, Q. Zhang, J. Zhu, Intrinsic origin of enhanced piezoelectricity in alkali niobate-based lead-free ceramics, J. Am. Ceram. Soc. 102 (2019) 5262–5270, https://doi.org/10.1111/jace.16365.

Supplementary materials

Elastic properties of domains and domain walls in $(K_{0.5}Na_{0.5})NbO_3$ single crystal

Katarina Žiberna[a,b*], Maja Koblar[a], Andraž Bradeško[a], Micka Bah[c], Franck Levassort[c], Goran Dražić[d], Hana Uršič[a,b] and Andreja Benčan[a,b*]

[a] Electronic Ceramics Department, Jožef Stefan Institute, 1000 Ljubljana, Slovenia

[b] Jožef Stefan International Postgraduate School, 1000 Ljubljana, Slovenia

[c] GREMAN UMR7347, Université de Tours, CNRS, INSA CVL, 37071 Tours, France

[d] Department of Materials Chemistry, National Institute of Chemistry, 1000 Ljubljana, Slovenia

* Corresponding author: katarina.ziberna@ijs.si, andreja.bencan@ijs.si

Figure S1: Surface orientation

The orientation of the measured surface was determined using EBSD. The surface was found to be nearly parallel to the $\{100\}_{pc}$ planes, with an inclination of ~11.5°. The scale is expressed in multiple uniform distributions (MUD) - a unit used to quantify the crystallographic orientation distribution in pole figures which indicates the strength of clustering compared to a random distribution.

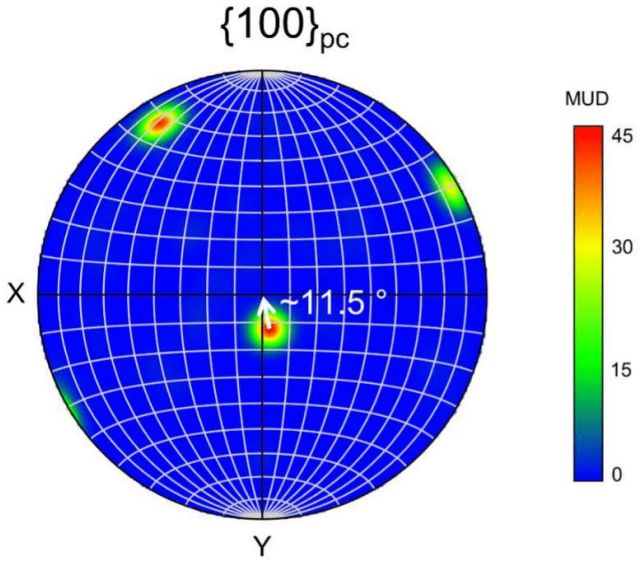

Figure S2: Determination of DW type from selected area electron diffraction patterns and domain structure sketch

The DW types labelled as 90° (Figure 1 and Figure 2, yellow arrows) and 60° (Figure 1 and Figure 2, white arrows) in the main text were additionally confirmed by the experimental selected area electron diffraction (SAED), which were compared with the simulated ones.

The simulated SAEDs for the DWs are constructed from two separate SAED patterns of domains on each side of the DW that are ultimately superimposed (one is shown in black and the other in pink) [1].

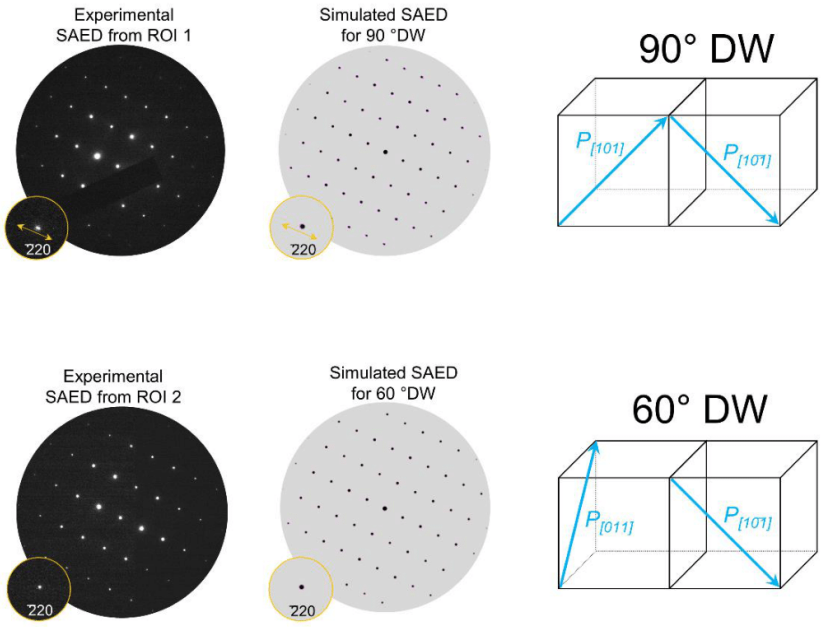

Based on the experimental data, i.e. in-plane (P_y) PFM and out-of-plane (P_z) PFM as well as transmission Kikuchi diffraction and selected are electron diffraction, a domain structure was reconducted considering the following assumptions:

- The x, y and z scanning directions are aligned with the $[010]_{pc}$, $[001]_{pc}$ and $[100]_{pc}$ directions, respectively.
- The $\overrightarrow{P_S}$ is parallel to $\{110\}_{pc}$ planes in the orthorhombic structure.
- As we do not have the PFM P_x in-plane image, in some domains, more than one variant of the orientation of $\overrightarrow{P_S}$ within one domain is possible. For example, the domains marked with white arrows in the Figure 1 and Figure 2 of the manuscript can have 2 possible direction of $\overrightarrow{P_S}$: in

the blue colored domains in the sketch below, the $\overrightarrow{P_s}$ can be pointing in $[1\bar{1}0]_{pc}$ or $[110]_{pc}$ direction, while for green ones $\overrightarrow{P_s}$ can be pointing in $[\bar{1}\bar{1}0]_{pc}$ or $[\bar{1}10]_{pc}$. For the sketch shown below, one variant of the blue domains was chosen arbitrarily, while the green domain variant was selected based on the fact that the 90° DW are parallel to $(001)_{pc}$ planes. The legend shows the two possible variants of the blue and green domains.

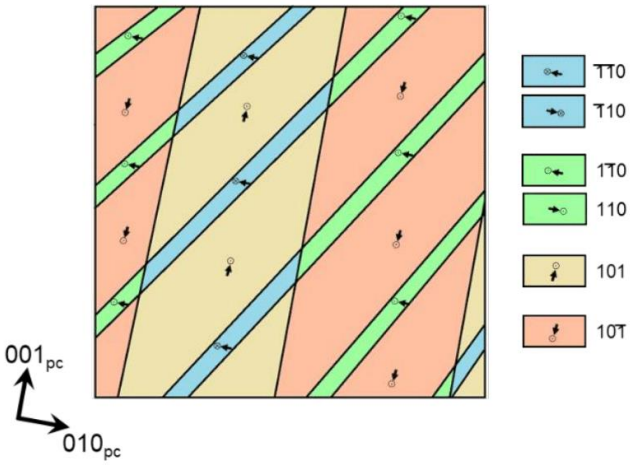

Figure S3: Reduced elastic modulus determined by nanoindentation

To confirm that the absolute values of the reduced elastic modulus measured with PF-QNM were correct, we determined the reduced elastic modulus with nanoindentation on an in situ indentation system Hysitron PI89 SEM PicoIndenter (Bruker, Billerica, MA, USA). The modulus was determined according to the methodology developed by Oliver and Pharr [2] from 20 measurements at (115 ± 9) GPa (the 20 indentation curves are shown below). A cube-corner diamond indentation probe was used for the measurements at a maximum peak force of 200 μN.

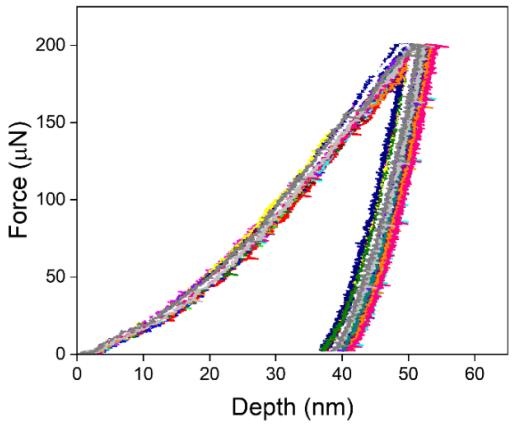

Figure S4: Elastic properties mapped using contact resonance frequency mapping and sample topography

To confirm our observations, the complex elastic response of the domains and DWs of KNN was additionally probed using another AFM-based method for measuring elastic properties, called contact resonance frequency mapping (CRFM), on a different part of the sample (first row). This technique tracks the resonance frequency of the interaction between the mechanically excited tip and the sample. A higher contact resonance frequency indicates a higher modulus of elasticity and vice versa, a lower contact resonance frequency indicates a lower modulus of elasticity.

In the second row, the 3D height map and the CRFM map of the area marked with a white square are shown enlarged. In this area, there is both a low roughness and a high roughness region that show an equally pronounced elastic response, indicating that the topography of the sample has no influence on the elasticity measurement. For example, in the low roughness region we can distinctly see features of a high contact resonance frequency (white empty arrow) and features of a lower contact resonance frequency (black empty arrow).

Both CRFM and PFM were made in a Jupiter XR atomic force microscope (Oxford Instruments Asylum Research, Santa Barbara, CA, USA). For CRFM, an AC160TS-R3 silicon tip with a nominal radius of 7 nm was used (Oxford Instruments Asylum Research, Santa Barbara, CA, USA). PFM was mapped with an ASYELEC.01-R2 probe with a Ti/Ir coating and a nominal radius of 25 nm (Oxford Instruments Asylum Research, Santa Barbara, CA, USA) at a driving voltage of 2 V in Dual AC Resonance Tracking mode.

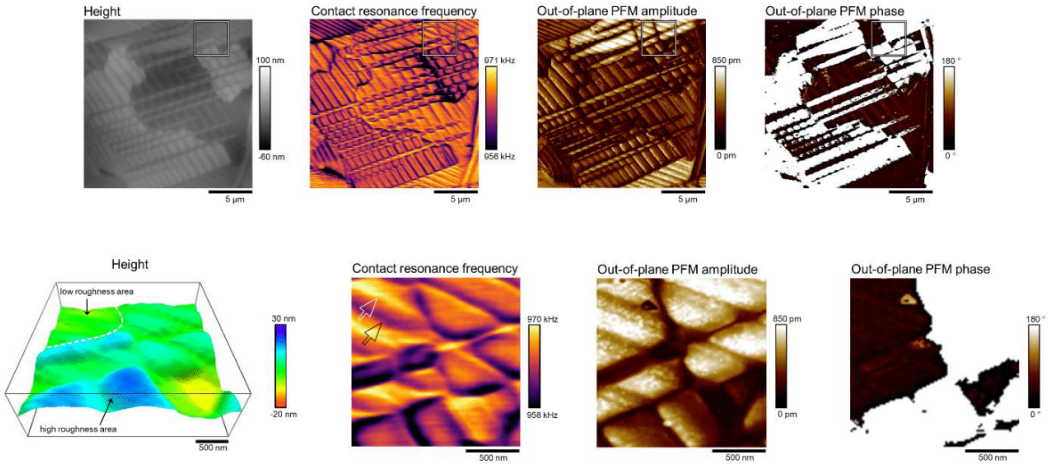

Figure S5: Elastic anisotropy of (K, Na)NbO_3

To show the complexity of the anisotropy of elastic properties in KNN, a projection of the Young's modulus was drawn in three dimensions based on the stiffness coefficient from Ref. [3], where the $[101]_{pc}$ direction is the polar direction. The projection was made using the ELATE software [4]. The scale is given in GPa.

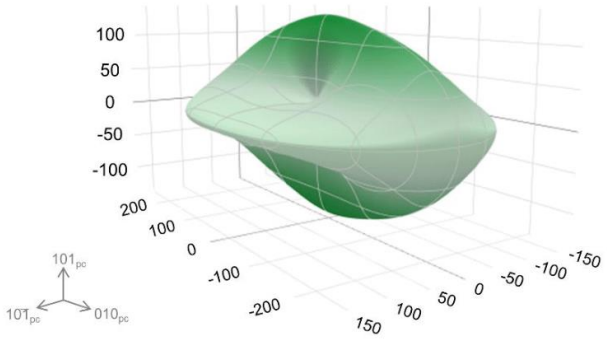

References

[1] O. Condurache, G. Dražić, A. Benčan, Voltage-driven ferroelectric domain dynamics in (K,Na)NbO_3 investigated by in situ transmission electron microscopy, Appl. Phys. Lett. 122 (2023) 202902. https://doi.org/10.1063/5.0149949.

[2] W.C. Oliver, G.M. Pharr, An improved technique for determining hardness and elastic modulus using load and displacment sensing indentation experiments, J. Mater. Res. 7 (1992) 1564–1583. https://doi.org/https://doi.org/10.1557/JMR.1992.1564.

[3] Z. Tan, Y. Peng, J. An, Q. Zhang, J. Zhu, Intrinsic origin of enhanced piezoelectricity in alkali niobate-based lead-free ceramics, J. Am. Ceram. Soc. 102 (2019) 5262–5270. https://doi.org/10.1111/jace.16365.

[4] R. Gaillac, P. Pullumbi, F.X. Coudert, ELATE: An open-source online application for analysis and visualization of elastic tensors, J. Phys. Condens. Matter. 28 (2016) 275201. https://doi.org/10.1088/0953-8984/28/27/275201.

Chapter 6

Conclusions

The work focuses on local measurements of mechanical properties of environmentally friendly ferroelectric materials, either from the perspective of energy consumption, as in the case of aerosol-deposited $0.9Pb(Mg_{1/3}Nb_{2/3})O_3{-}0.1PbTiO_3$ thick films, or lead-free ferroelectrics such as $BiFeO_3$ and $(K_{0.5}Na_{0.5})NbO_3$. The work on $0.9Pb(Mg_{1/3}Nb_{2/3})O_3{-}0.1PbTiO_3$ thick films and $BiFeO_3$ bulk ceramics primarily focuses on the evaluation of Young's modulus (E) and hardness (H) of both materials and assessing the deformation mechanism under mechanical loading. For $(K_{0.5}Na_{0.5})NbO_3$ single crystals, a high-resolution atomic force microscopy (AFM) technique was used to investigate the variation of elasticity between domains and domain walls (DWs).

6.1 Influence of Thermal Treatment on the Cross-Sectional Properties of Aerosol-Deposited $Pb(Mg_{1/3}Nb_{2/3})O_3{-}PbTiO_3$ Thick Films

The first study focuses on the evaluation of E and H across the cross-section of aerosol-deposited $0.9Pb(Mg_{1/3}Nb_{2/3})O_3{-}0.1PbTiO_3$ thick films on stainless steel substrates using nanoindentation. The mechanical properties of the prepared films were evaluated, and after additional annealing at 500 °C, the main purpose being to enhance the functional properties. The conclusions of this part are as follows:

- Annealing of aerosol-deposited $0.9Pb(Mg_{1/3}Nb_{2/3})O_3{-}0.1PbTiO_3$ films at 500 °C results in slight changes in the microstructure, namely grain growth and the redistribution of pores into chain-like defects consisting of nanopores. The increase in heterogeneity of the microstructure affected the mechanical properties, as evidenced by a larger scatter of the force-depth curves and numerous pop-ins after annealing.
- Both E and H increased after annealing, which, according to the literature, is related to the reduction of residual stresses in the structure during the aerosol deposition process.
- While H shows no specific trend across the cross-section of the films, both as-deposited and annealed, E decreases linearly as the indentations are further away from the substrate, indicating an influence of the elastic properties of the substrate on the measurement of E.
- Both films showed good crack resistance at a measurement force of 1 mN, which is attributed to the dense nanograined microstructure that likely favors the sliding of grain boundaries as a deformation mechanism over dislocation-mediated plasticity.

6.2 Nanomechanical Characterization of $BiFeO_3$ Ferroelectric Ceramics

The second part reports on the H and E_r of $BiFeO_3$ ceramics measured using a nanoindentation system with a cube corner probe in a force range of 200 μN to 2 mN. In addition, the mechanism of plastic deformation under the indentation probe is discussed based on the defects observed after deformation. The following conclusions were drawn:

- As the indentation peak force increases, the values of H and E_r decrease from (9.9 ± 0.4) GPa and (113.7 ± 6.9) GPa, respectively (values determined at the peak force of 200 μN) to (105.1 ± 5.3) GPa and (6.6 ± 0.2) GPa (measured at 2 mN). The decrease in H was attributed to the indentation size effect, while E_r is influenced by microstructural defects such as pores, which lead to a smaller E_r as the elastic zone becomes larger with increasing force.
- The size effect transition from ductile to brittle behavior was observed between 500 μN and 1 mN for a cube corner diamond indentation probe.
- Pop-in analysis in combination with (S)TEM images from an undeformed region showed homogeneous dislocation nucleation from a dislocation-free lattice near the shear stress of τ_{th} ~7.4 GPa. The newly formed dislocations were attributed to the room temperature perovskite slip system $\{110\}_{pc}<1\bar{1}0>_{pc}$.
- Evidence of dislocation movement and multiplication was observed in the form of an array, as well as near the deformed surface, where dislocations appear to arrange in low-angle and grain boundaries, forming sub-grains of approximately 10 nm in size. The accumulation of dislocations at the surface may serve as a high-stress region where cracks can develop.

6.3 Elastic Properties of Domains and Domain Walls in $(K_{0.5}Na_{0.5})NbO_3$ Single Crystal

Lastly, we investigated the mechanical response of domains and DWs in $(K_{0.5}Na_{0.5})NbO_3$ using specialized AFM techniques, which have higher spatial resolution compared to nanoindentation. The conclusions were the following:

- Only ferroelastic 90° and 60° DWs were found within the region of interest.
- The 90° DWs show an increase in elasticity from the average E_r of 130 GPa on one side of the domain and a decrease on the other side. The difference in E_r is estimated to be 20 %. While the origin of the elasticity variations in DWs remains unknown, it is likely a combination of the inherent elastic properties of DWs and extrinsic contributions, such as properties from the neighboring domains and the measurement itself.
- The 60° DWs showed no elastic contrast.
- The domains show different elastic properties due to the inherent elastic anisotropy. The elastic properties within the domain were not correlated with the direction of P_s due to the complexity of orthorhombic symmetry and sample orientation.

References

[1] K. Uchino, *Ferroelectric devices*. Boca Raton, USA: CRC Press, 2009.

[2] L. Porz, "60 years of dislocations in ceramics: A conceptual framework for dislocation mechanics in ceramics," *Int. J. Ceram. Eng. Sci.*, vol. 4, pp. 214–239, 2022.

[3] S. L. dos Santos e Lucato, D. C. Lupascu and J. Rödel, "Effect of Poling Direction on R-Curve Behavior in Lead Zirconate Titanate," *J. Am. Ceram. Soc.*, vol. 83, pp. 424–426, 2000.

[4] X. Wang, L. K. Venkataraman, C. Tan and Y. Li, "Fracture behavior in electrically poled alkaline bismuth- and potassium- based lead-free piezoceramics using Vickers indentation," *Scr. Mater.*, vol. 194, p. 113647, 2021.

[5] D. Brunner, S. Taeri-Baghbadrani, W. Sigle and M. Rühle, "Surprising Results of a Study on the Plasticity in Strontium Titanate," *J. Am. Ceram. Soc.*, vol. 84, pp. 1161–1163, 2001.

[6] S. Taeri, D. Brunner, W. Sigle and M. Rühle, "Deformation behaviour of strontium titanate between room temperature and 1800 K under ambient pressure," *Zeitschrift fuer Met. Res. Adv. Tech.*, vol. 95, pp. 433–446, 2004.

[7] X. Fang, J. Zhang, A. Frisch, O. Preuß, C. Okafor, M. Setvin and W. Lu, "Room-temperature bulk plasticity and tunable dislocation densities in $KTaO_3$," *J. Am. Ceram. Soc.*, vol. 107, pp. 7054–7061, 2024.

[8] M. Höfling, M. Trapp, L. Porz, H. Uršič, E. Bruder, H-J Kleebe, J. Rödel and J. Koruza, "Large plastic deformability of bulk ferroelectric $KNbO_3$ single crystals," *J. Eur. Ceram. Soc.*, vol. 41, pp. 4098–4107, 2021.

[9] K. Tsuji, Z. Fan, S. H. Bang, S. Dursun, S. Trolier-McKinstry and C. A. Randall, "Cold sintering of the ceramic potassium sodium niobate, $(K_{0.5}Na_{0.5})NbO_3$, and influences on piezoelectric properties," *J. Eur. Ceram. Soc.*, vol. 42, pp. 105–111, 2022.

[10] S. Salmanov, M. Koblar, B. Kmet, B. Malič, T. Rojac, D. Kuščer aand M. Otoničar, "Structure and electrical properties of cold-sintered strontium-doped potassium sodium niobate," *J. Eur. Ceram. Soc.*, vol. 43, pp. 7516–7523, 2023.

[11] F. Zhuo, U. R. Echstein, N. H. Khansur, C. Dietz, D. Urushihara, T. Asaka, K. Kakimoto, K. G. Webber, X. Fang and J. Rödel, "Temperature-induced changes of the electrical and mechanical properties of aerosol-deposited $BaTiO_3$ thick films for energy storage applications," *J. Am. Ceram. Soc.*, vol. 105, pp. 4108–4121, 2022.

[12] M. Sadl, A. Lebar, J. Valentincic and H. Ursic, "Flexible Energy-Storage Ceramic Thick-Film Structures with High Flexural Fatigue Endurance," *ACS Appl. Energy*

Mater., vol. 5, pp. 6896–6902, 2022.

[13] X. Fang, L. Porz, K. Ding and A. Nakamura, "Bridging the gap between bulk compression and indentation test on room-temperature plasticity in oxides: Case study on $SrTiO_3$," *Crystals*, vol. 10, p. 933, 2020.

[14] K. H. Yang, N. J. Ho and H. Y. Lu, "Deformation microstructure in (001) single crystal strontium titanate by vickers indentation," *J. Am. Ceram. Soc.*, vol. 92, pp. 2345–2353, 2009.

[15] L. Porz, A. J. Klomp, X. Fang, N. Li, C. Yildirim, C. Detlefs, E. Bruder, M. Höfling, W. Rheinheimer, E. A. Patterson, P. Gao, K. Durst, A. Nakamura, K. Albe, H. Simons and J. Rödel, "Dislocation-toughened ceramics," *Mater. Horizons*, vol. 8, pp. 1528–1537, 2021.

[16] O. Preuß, E. Bruder, W. Li, F. Zhuo, C. Minner, J. Zhang, J. Rödel and X. Fang, "Dislocation toughening in single-crystal $KNbO_3$," *J. Am. Ceram. Soc.*, vol. 106, pp. 4371–4381, 2023.

[17] M. Höfling, L. Porz, M. Scherer, S. Gao, F, Zhuo, D. Isaia and J. Rödel, "High-temperature plastic deformation of ⟨110⟩-oriented $BaTiO_3$ single crystals," *J. Mater. Res.*, vol. 37, pp. 737–746, 2022.

[18] F. Zhuo, X. Zhou, S. Gao, M. Höfling, F. Dietrich, P. B. Groszewicz, L. Fulanović, P. Brechner, A. Wohninsland, B-X. Xu, H-J. Kleebe, X. Tan, J. Koruza, D. Damjanovic and J. Rödel, "Anisotropic dislocation-domain wall interactions in ferroelectrics," *Nat. Commun.*, vol. 13, p. 6676, 2022.

[19] C. Stefani, L. Ponet, K. Shapovalov, P. Chen, E. Langenberg, D. G. Schlom, S. Artyukhin, M. Stengel, N. Domingo and G. Catalan, "Mechanical Softness of Ferroelectric 180° Domain Walls," *Phys. Rev. X*, vol. 10, p. 41001, 2020.

[20] C. P. T. Nguyen, P. Schoenherr and J. Seidel, "Intrinsic Mechanical Compliance of 90° Domain Walls in $PbTiO_3$," *Adv. Funct. Mater.*, vol. 33, p. 2211906, 2023.

[21] D. Torres-Torres, A. Hurtado-Macias, R. Herrera-Basurto, E. Conteras, S. Sanchez, F. Mercader-Trejo, J. Gonzalez-Hernandez and O. Auciello, "Anisotropic behavior of mechanical properties for the a- and c-domains in a (001) $BaTiO_3$ single crystal," *J. Phys. Condens. Matter*, vol. 35, p. 355703, 2023.

[22] D. Damjanovic, "Ferroelectric, dielectric and piezoelectric properties of ferroelectric thin films and ceramics," *Reports Prog. Phys.*, vol. 61, p. 1267, 1998.

[23] R. E. Cohen, "Origin of ferroelectricity in perovskite oxides," *Nature*, vol. 358, pp. 136–138, 1992.

[24] S. Mantri and J. Daniels, "Domain walls in ferroelectrics," *J. Am. Ceram. Soc.*, vol. 104, pp. 1619–1632, 2021.

[25] B. Jaffe, W. R. Cook and H. Jaffe, *Piezoelectric Ceramics*. London, UK: Academic Press, 1971.

[26] P. Zubko, G. Catalan and A. K. Tagantsev, "Flexoelectric effect in solids," *Annu. Rev. Mater. Res.*, vol. 43, pp. 387–421, 2013.

[27] J. Goldstein, *Scanning Electron Microscopy and X-Ray Microanalysis*. New York, USA: Springer New York, 2003.

[28] T. Rojac, A. Bencan, B. Malic, G. Tutuncu, J. L. Jacobs, J. E. Daniels and D. Damjanovic, "$BiFeO_3$ ceramics: Processing, electrical, and electromechanical

properties," *J. Am. Ceram. Soc.*, vol. 97, pp. 1993–2011, 2014.

[29] T. Rojac, M. Kosec, B. Budic, N. Setter and D. Damjanovic, "Strong ferroelectric domain-wall pinning in $BiFeO_3$ ceramics," *J. Appl. Phys.*, vol. 108, p. 074107, 2010.

[30] T. Rojac, E. Khomyakova, J. Walker, H. Uršič and A. Benčan, "$BiFeO_3$ ceramics anf thick films: Processing issues and electromechanical properties," in *Magnetic, ferroelectric and multiferoic metal oxides*, Springer, 2018.

[31] A. Ul-Hamid, *A Beginners Guide to Scanning Electron Microscopy*. Cham, Switzerland: Springer, 2018.

[32] D. B. Williams and C. B. Carter, *Transmission Electron Microscopy: A Tetx Book for Materials Science*. New York, USA: Springer, 2009.

[33] A. Bencan, T. Rojac, G. Drazic, M. Kosec and D. Damjanovic, "Domain Structure of $BiFeO_3$ Ceramics Determined by the Transmission Electron Microscopy," *Microsc. Microanal.*, vol. 17, pp. 1892–1893, 2011.

[34] M. J. Cabral, Z. Chen and X. Liao, "Scanning transmission electron microscopy for advanced characterization of ferroic materials," *Microstructures*, vol. 3, p. 2023040, 2023.

[35] C. Ophus, "Quantitative Scanning Transmission Electron Microscopy for Materials Science: Imaging, Diffraction, Spectroscopy, and Tomography," *Annu. Rev. Mater. Res.*, vol. 53, pp. 105–141, 2023.

[36] C. Ophus, "Four-Dimensional Scanning Transmission Electron Microscopy (4D-STEM): From Scanning Nanodiffraction to Ptychography and Beyond," *Microsc. Microanal.*, pp. 563–582, 2019.

[37] R. E. Newnham, *Properties of Materials: Anisotropy, Symmetry, Structure*. New York, USA: Oxford University Press, 2005.

[38] D. Hull and D. J. Bacon, *Introduction to Dislocations*. Amsterdam, Netherlands: Elsevier Ltd., 2011.

[39] X. Fang, H. Bishara, K. Ding, H. Tsybenko, L. Porz, M. Höfling, E. Bruder, Y. Li, G. Dehm and K. Durst, "Nanoindentation pop-in in oxides at room temperature: Dislocation activation or crack formation?," *J. Am. Ceram. Soc.*, vol. 104, pp. 4728–4741, 2021.

[40] J. J. Gilman, "Dislocation Sources in Crystals," *J. Appl. Phys.*, vol. 30, pp. 1584–1594, 1959.

[41] A. F. Mark, M. Castillo-Rodriguez and W. Sigle, "Unexpected plasticity of potassium niobate during compression between room temperature and 900 °C," *J. Eur. Ceram. Soc.*, vol. 36, pp. 2781–2793, 2016.

[42] P. Hirel, P. Cordier and P. Carrez, "<110>{-110} edge dislocations in strontium titanate: Charged vs neutral, glide vs climb," *Acta Mater.*, vol. 285, p. 120636, 2025.

[43] P. Hirel, P. Marton, M. Mrovec and C. Elsässer, "Theoretical investigation of {110} generalized stacking faults and their relation to dislocation behavior in perovskite oxides," *Acta Mater.*, vol. 58, no. 18, pp. 6072–6079, 2010.

[44] W. C. Oliver and G. M. Pharr, "An improved technique for determining hardness and elastic modulus using load and displacment sensing indentation experiments," *J. Mater. Res.*, vol. 7, pp. 1564–1583, 1992.

[45] H. Nili, K. Kalantar-Zadeh, M. Bhaskaran and S. Sriram, "In situ nanoindentation:

Probing nanoscale multifunctionality," *Prog. Mater. Sci.*, vol. 58, pp. 1–29, 2013.

[46] J. Akedo, "Room temperature impact consolidation (RTIC) of fine ceramic powder by aerosol deposition method and applications to microdevices," *J. Therm. Spray Technol.*, vol. 17, pp. 181–198, 2008.

[47] D. Hanft, J. Exner, M. Schubert, T. Stöcker, P. Fuierer and R. Moos, "An overview of the Aerosol Deposition method: Process fundamentals and new trends in materials applications," *J. Ceram. Sci. Technol.*, vol. 6, pp. 147–181, 2015.

[48] M. Bentzen, J. Maier, U. Eckstein, J. He, A. Henss, N. Khansur and J. Glaum, "Enhanced grain growth and dielectric properties in aerosol deposited $BaTiO_3$," *J. Eur. Ceram. Soc.*, vol. 43, pp. 4386–4394, 2023.

[49] "ISO 14577-1:2015: Metallic materials-Instrumented indentation test for hardness and materials parameters." Geneva, Switzerland, 2015.

[50] H. Bückle, "Use of hardness test to determine other material properties," in *The Science of Hardness Testing and Its Research Applications*, Novelty, USA: American Society for Metals, 1973.

[51] S. J. Bull, "Microstructure and indentation response of TiN coatings: The effect of measurement method," *Thin Solid Films*, vol. 688, no. July, p. 137452, 2019.

[52] S. Zak, C. O. W. Trost, P. Kreiml and M. J. Cordill, "Accurate measurement of thin film mechanical properties using nanoindentation," *J. Mater. Res.*, vol. 37, pp. 1373–1389, 2022.

[53] M. Algueró, A. J. Bushby, M. J. Reece, M. L. Calzada and L. Pardo, "Mechanical Characterisation of Ferroelectric Thin Films for Mems," *Integr. Ferroelectr.*, vol. 32, pp. 83–92, 2001.

[54] K. Cordero-Edwards, N. Domingo, A. Abdollahi, J. Sort and G. Catalan, "Ferroelectrics as Smart Mechanical Materials," *Adv. Mater.*, vol. 29, pp. 1–6, 2017.

[55] W. D. Nix and H. Gao, "Indentation size effects in crystalline materials: A law for strain gradient plasticity," *J. Mech. Phys. Solids*, vol. 46, pp. 411–425, 1998.

[56] H. Hertz, "On the contact of elastic solids," *J. für die reine und Angew. Math.*, vol. 92, pp. 156–171, 1882.

[57] K. L. Johnson, *Contact Mechanics*. Cambridge, United Kingdom: Cambrige University Press, 1985.

[58] W. W. Gerberich, J. C. Nelson, E. T. Lilleodden, P. Anderson and J. T. Wyrobek, "Indentation induced dislocation nucleation: The initial yield point," *Acta Mater.*, vol. 44, pp. 3585–3598, 1996.

[59] C. Zener, "The micro-mechanism of fracture," in *Fracturing of metals*, Novelty, USA: American Society for Metals, 1948.

[60] A. N. Stroh, "The form ation of cracks as a result of plastic flow," *Proc. R. Soc. A Mat. Phys. Eng. Sci.*, vol. 223, pp. 404–414, 1954.

[61] X. Fang, K. Ding, C. Minnert, A. Nakamura and K. Durst, "Dislocation-based crack initiation and propagation in single-crystal $SrTiO_3$," *J. Mater. Sci.*, vol. 56, pp. 5479–5492, 2021.

[62] G. A. Schneider, T. Scholz and F. J. Espinoza-Beltrán, "Rosette screw arms created by *ac*-domain structures and dislocations in barium titanate during nanoindentation," *Appl. Phys. Lett.*, vol. 92, p. 022906, 2008.

[63] P. Gao, J. Britson, C. T. Nelson, J. R. Jokisaari, C. Duan, M. Trassin, S-H. Baek, H. Guo, L. Li, Y. Wang, Y-H. Chu, A. M. Minor, C-B. Eom, R. Ramech, L-Q. Chen and X. Pan, "Ferroelastic domain switching dynamics under electrical and mechanical excitations," *Nat. Commun.*, vol. 5, p. 3801, 2014.

[64] Y. Deng, C. Gammer, J. Ciston, P. Ercius, C. Ophus, K. Bustillo, C. Song, R. Zhang, D. Wu, Y. Du, Z. Chen, H. Dong, A. G. Khacahaturyan and A. M. Minor, "Hierarchically-structured large superelastic deformation in ferroelastic-ferroelectrics," *Acta Mater.*, vol. 181, pp. 501–509, 2019.

[65] Y. Heo, P. Sharma, Y. Y. Liu, J. Y. Li and J. Seidel, "Mechanical probing of ferroelectrics at the nanoscale," *J. Mater. Chem. C*, vol. 7, pp. 12441–12462, 2019.

[66] S. Morita, *Roadmap of Scanning Probe Microscopy.* Berlin, Germany: Springer Science+Buisness Media, Inc., 2007.

[67] T. J. Young, M. A. Monclus, T. L. Burnett, W. R. Broughton, S. L. Ogin and P. A. Smith, "The use of the PeakForceTM quantitative nanomechanical mapping AFM-based method for high-resolution Young's modulus measurement of polymers," *Meas. Sci. Technol.*, vol. 22, p. 125703, 2011.

[68] K. Yamanaka and S. Nakano, "Ultrasonic Atomic Force Microscope with Overtone Excitation of Cantilever," *Jpn. J. Appl. Phys.*, vol. 35, pp. 3787–3792, 1996.

[69] U. Rabe, "Atomic Force Acustic Microscopy," in *Applied Scanning Probe Methods II: Scanning Probe Microscopy Techniques*, Berlin, Germany: Springer Science+Buisness Media, Inc., 2006.

[70] M. Kocun, A. Labuda, A. Gannepalli and R. Proksch, "Contact resonance atomic force microscopy imaging in air and water using photothermal excitation," *Rev. Sci. Instrum.*, vol. 86, p. 083706, 2015.

[71] D. C. Hurley, "Contact Resonance Force Microscopy Techniques for Nanomechanical Measurements," in *Applied Scanning Probe Methods XI: Scanning Probe Microscopy Techniques*, Berlin, Germany: Springer Science+Buisness Media, Inc., 2008.

[72] "Contact Resoncance Viscoeleasting Mapping Mode," 2014 [Online]. Avalible: https://afm.oxinst.com/assets/uploads/products/asylum/documents/Contact-Resonance-Viscoelastic-Mapping-Mode.pdf. [Accessed 15 4 2025].

[73] C. Stefani, E. Langenberg, K. Cordero-Edwards, D. G. Schlom, G. Catalan and N. Domingo, "Mechanical reading of ferroelectric polarization," *J. Appl. Phys.*, vol. 130, p. 074103, 2021.

[74] T. Tsuji, H. Ogiso, J. Akedo, S. Saito, K. Fukuda and K. Yamanaka, "Evaluation of domain boundary of piezo/ferroelectric material by ultrasonic atomic force microscopy," *Japanese J. Appl. Physics, Part 1 Regul. Pap. Short Notes Rev. Pap.*, vol. 43, pp. 2907–2913, 2004.

[75] T. Tsuji, S. Saito, K. Fukuda, K. Yamanaka, H. Ogiso, J. Akedo and Y. Kawamaki, "Significant stiffness reduction at ferroelectric domain boundary evaluated by ultrasonic atomic force microscopy," *Appl. Phys. Lett.*, vol. 87, p. 071909, 2005.

[76] D. Damjanovic, "Hysteresis in Piezoelectric and Ferroelectric Materials," in *The Science of Hysteresis*, Cambridge, USA: Academic Press, 2005.

[77] T. Rojac, A. Bencan, G. Drazic, N. Sakamoto, H. Ursic, B. Jancar, G. Tavcar, M.

Makarovic, J. Walker, B. Malic and D. Damjanovic, "Domain-wall conduction in ferroelectric BiFeO3 controlled by accumulation of charged defects," *Nat. Mater.*, vol. 16, pp. 322–327, 2017.

[78] X. He, X. Ding, J. Sun, G. F. Nataf and E. K. H. Salje, "Elastic softening and hardening at intersections between twin walls and surfaces in ferroelastic materials," *APL Mater.*, vol. 11, p. 071114, 2023.

[79] M. Sadl, O. Condurache, A. Bencan, M. Dragomir, U. Prah, B. Malic, M. Deluca, U. Eckstein, D. Hausmann, N. H. Khansur, K. G. Webber and H. Ursic, "Energy-storage-efficient $0.9Pb(Mg_{1/3}Nb_{2/3})O_3$–$0.1PbTiO_3$ thick films integrated directly onto stainless steel," *Acta Mater.*, vol. 221, p. 117403, 2021,

[80] M. Sadl, K. Nadaud, M. Bah, F. Levassort, U. Eckstein, N. K. Khansur, K. G. Webber and H. Ursic, "Multifunctional energy storage and piezoelectric properties of $0.65Pb(Mg_{1/3}Nb_{2/3})O_3$–$0.35PbTiO_3$ thick films on stainless-steel substrates," *J. Phys. Energy*, vol. 4, p. 117403, 2022.

[81] K. Maruyama, Y. Kawakami and F. Narita, "Young's modulus and ferroelectric property of $BaTiO_3$ films formed by aerosol deposition in consideration of residual stress and film thickness," *Jpn. J. Appl. Phys.*, vol. 61, 2022.

[82] J. Ryu, J. J. Choi, B. D. Hahn, D. S. Park and W. H. Yoon, "Ferroelectric and piezoelectric properties of $0.948(K_{0.5}Na_{0.5})NbO_3$–$0.052LiSbO_3$ lead-free piezoelectric thick film by aerosol deposition," *Appl. Phys. Lett.*, vol. 92, pp. 2006–2009, 2008.

Bibliography

Scientific Articles Related to the Thesis

K. Žiberna, M. Šadl, A. Drnovšek, G. Dražić, H. Uršič and A. Benčan, "Influence of Thermal Treatment on the Cross-Sectional Properties of Aerosol-Deposited $Pb(Mg_{1/3}Nb_{2/3})O_3$–$PbTiO_3$ Thick Films", *Crystals*, **13**, 536, 2023.

K. Žiberna, M. Koblar, M. Bah, F. Levassort, G. Dražić, H. Uršič and A. Benčan, "Nanomechanical characterization of $BiFeO_3$ ferroelectric ceramics", *Journal of the European Ceramic Society*, **44**, 7025-7031, 2024.

K. Žiberna, M. Koblar, A. Bradeško, M. Bah, F. Levassort G. Dražić, H. Uršič and A. Benčan, "Elastic properties of domains and domain walls in $(K_{0.5}Na_{0.5})NbO_3$ single crystal", *Journal of the European Ceramic Society*, **45**, 117566, 2024.

Other Scientific Articles

M. Makarovič, N. Kanas, A. Zorko, K. Žiberna, H. Uršič, D. R. Småbråten, S. M. Selbach and T. Rojac, "Tailoring the electrical conductivity and hardening in $BiFeO_3$ ceramics", *Journal of the European Ceramic Society,* **40**, 5483-5493, 2020.

S. W. Konsago, K. Žiberna, B. Kmet, A. Benčan, H. Urišč and B. Malič, "Chemical solution deposition of barium titanate thin films with ethylene glycol as solvent for barium acetate", *Molecules*, **27**, 3753, 2022.

U. Eckstein, J. Exner, A. Benčan, K. Žiberna, G. Dražić, H. Uršič, H. Wittkämper, C. Papp, J. Kita, R. Moos, K. G. Webber and N. H. Khansur, "Temperature-dependent dielectric anomalies in powder aerosol deposited ferroelectric ceramic films", *Jornal of Materiomics*, **8**, 1239-1250, 2022.

M. Fricaudet, K. Žiberna, S. Salmanov, J. Kreisel, D. He, B. Dkhil, T. Rojac, M. Otoničar, P.-E. Janolin and A. Bradeško, "Multifunctional properties of polyvinylidene-fluoride-based materials", *ACS applied electrnoic materials*, **4** ,5429-5436, 2022.

G. Ferrero, K. Astafiev, E. Ringgaard, L. S. Oliveira, B. R. Sudireddy, A. Bjørnetun Haugen, K. Žiberna, B. Malič and T. Rojac, "Piezoelectric properties of mechanochemically processed $0.67BFeO_3$–$0.33BaTiO_3$ ceramics", *Journal of the European Ceramic Society,* **43**, 350-361, 2023.

S. W. Konsago, K. Žiberna, J. Ekar, J. Kovač and B. Malič, "Designing the thermal processing of $Ba(Ti_{0.8}Zr_{0.2})O_3$–$(Ba_{0.7}Ca_{0.3})TiO_3$ thin films from ethylene glycol-derived precursor", *Journal of Materials Chemistry C*, **12**, 14658-14666, 2024.

S. W. Konsago, K. Žiberna, A. Matavž, B. Mandal, S. Glinšek, Y. Fleming, A. Benčan, G. Brennecka, H. Uršič and B. Malič, "Engineering the microstructure and functional properties of $0.5Ba(Zr_{0.2}Ti_{0.8})O_3$–$0.5(Ba_{0.7}Ca_{0.3})TiO_3$ thin films", *ACS Applied Electronic Materials*, **6**, 4467-4477, 2024.

S. Salmanov, M. Yao, K. Žiberna, M. Lachhab, B. Dkhil, B. Malič, T. Rojac, D. Kuščer and M. Otoničar, "Impact of transient liquid phase on the cold sintering of multiferroic $BiFeO_3$", *Journal of the European Ceramic Society,* **45**, 116846, 2025.

S. W. Konsago, K. Žiberna, A. Matavž, B. Mandal, S. Glinšek, G. Brennecka, H. Uršič and B. Malič, "High energy storage density and efficiency of $0.5Ba(Zr_{0.2}Ti_{0.8})O_3$–$0.5(Ba_{0.7}Ca_{0.3})TiO_3$ thin films on platinized sapphire substrates", *Journal of Materials Chemistry A*, **13**, 2911-2919, 2025.

Published Scientific Conference Contributions – Abstracts (Invited Lecture)

A. Benčan, O. Condurache, K. Žiberna and G. Dražić, "Structure and dynamics of ferroelectric domain walls down to the atomic level", *XVIIIth ECerS conference : Conference & Exhibition of the European Ceramic Society*, 2023, Lyon, France.

A. Benčan, O. Condurache, K. Žiberna and G. Dražić, "Atomic-scale structure and defect dynamics in lead-free perovskite ferroelectrics using STEM", *IEEE UFFC-JS 2024*, 2024, Taiper, Taiwan.

A. Benčan, O. Condurache, K. Žiberna and G. Dražić, "Exploring structure in lead-free ferroelectrics at the atomic level", *Electroceramics XIX Conference*, 2024, Vilnius, Lithuania.

A. Benčan, O. Condurache, K. Žiberna and G. Dražić, "Static and dynamic structural characteristics of defects in perovskite ferroelectrics through scanning transmission electron microscopy", *ECAPD 2024: European Conference on Applications of Polar Dielectrics*, 2024, Trondheim, Norway.

A. Benčan, O. Condurache, K. Žiberna, A. Kokalj, M. Poberžnik and G. Dražić, "In situ STEM investigation of perovskite ferroelectrics: structural defect dynamics down to the atomic level", *5th Slovene Microsocpy Symposyum*, 2024, Rogla, Slovenia.

M. Otoničar, S. Salmanov, K. Žiberna, M. Lachhab, A. Benčan, T. Rojac and D. Kuščer, "Pressure-dissolution-induced structural defects in ferroelectric perovskites", *20th DSL2024*, 2024, Barcelona, Spain.

Published Scientific Conference Contributions – Abstracts

S. Salmanov, M. Yao, K. Žiberna, B. Dkhil, A. Kocjan, T. Rojac and M. Otoničar, "Dense bismuth ferrite ceramic using cold sintering process", *Electroceramics XVII*, 2020, Darmstadt, Geramny.

K. Žiberna, S. W. Konsago, B. Malič, B. Kmet, O. Condurache and A. Benčan, "Electron microscopy study of $BaTiO_3$-based thin films prepared by chemical solution deposition", *27th Annual Meeting of the Slovenian Chemical Society*, 2021, Portorož, Slovenia.

S. W. Konsago, K. Žiberna, B. Kmet, H. Urišč and B. Malič, "Preparation of solid solution of barium titanate-based thin films by chemical solution deposition", *Throughout knowledge towards a green new world: 13th Jožef Stefan International Postgraduate School Students' Conference and 15th Young Researchers' Day of Chemistry, material science, biochemistry and environment (CMBE day)*, 2021, online.

K. Žiberna, S. W. Konsago, O. Condurache, B. Kmet, B. Malič, and A. Benčan, "Microstructural characterisation of ferroelectric $BaTiO_3$-based thin films", *Throughout knowledge towards a green new world: 13th Jožef Stefan International Postgraduate School Students' Conference and 15th Young Researchers' Day of Chemistry, material science, biochemistry and environment (CMBE day)*, 2021, online.

G. Ferrero, K. Astafiev, E. Ringgaard, R. Lou-Møller, B. R. Sudireddy, A. Bjørnetun Haugen, K. Žiberna, M. Makarovič, T. Rojac and B. Malič, "Effect of $BaTiO_3$ seeding on the piezoelectric properties of mechanochemically activated

$0.67BiFeO_3$–$0.33BaTiO_3$ ceramics", *Piezo 2021 : Piezoelectrics for End Users XI*, 2021, online.

S. Salmanov, M. Yao, K. Žiberna, T. Rojac, D. Kuščer, B. Malič, B. Dkhil, C. A. Randall and M. Otoničar, "Optimization of cold-sintering of bismuth ferrite", *IEEE ISAF 2021 joint ISAF ISIF-PMF virtual Conference, IEEE International Symposium on Applications of Feeroelectric, (ISAF) and International Symposium on Integrated Functionalities, (ISIF) and Piezoresponse Force Microscopy Workshop, (PFM),* 2020, online.

G. Ferrero, K. Žiberna, M. Makarovič, T. Rojac, B. Malič, Astafiev, E. Ringgaard, R. Lou-Møller, A. Bjørnetun Haugen and B. R. Sudireddy, "Effect of $BaTiO_3$ seeding on the piezoelectric properties of mechanochemically activated $0.67BiFeO_3$–$0.33BaTiO_3$ ceramics", *IEEE ISAF 2021 joint ISAF ISIF-PMF virtual Conference, IEEE International Symposium on Applications of Feeroelectric, (ISAF) and International Symposium on Integrated Functionalities, (ISIF) and Piezoresponse Force Microscopy Workshop, (PFM),* 2020, online.

S. W. Konsago, K. Žiberna, B. Kmet, H. Urišč and B. Malič, "Chemical solution deposition of $BaTiO_3$-based thin films on $LaNiO_3$ seed layers", *56th International Conference on Microelectronics, Devices and Materials & the Workshop on Personal Sensor for Remote Health Care Monitoring*, 2021, Ljubljana, Slovenia.

K. Žiberna, M. Koblar, A. Drnovšek, H. Uršič and A. Benčan, "Nanomechanical properties of ferroelectric $BiFeO_3$ ceramics", *28th Annual Meeting of the Slovenian Chemical Sociaty,* 2022, Portorož, Slovenia.

M. Fricaudet, M. Koblar, K. Žiberna, S. Salmanov, S. K. Chandrashekar, D. He, J. Kreisel, B. Dkhil, T. Rojac, M. Otoničar, P.-E. Janolin and A.Bradeško, "PVDF-based materials for multiphysic energy harvesting", *ISAF 2022 : ISAF-PFM-ECAPD*, 2022, Tours, France.

S. W. Konsago, K. Žiberna, B. Kmet, A. Benčan, H. Urišč and B. Malič, "$Ba(Zr,Ti)O_3$–$(Ba,Ca)TiO_3$ ferroelectric thin films from ethylene glycol-based solutions", *ISAF 2022 : ISAF-PFM-ECAPD*, 2022, Tours, France.

K. Žiberna, A. Drnovšek, H. Uršič, T. Rojac and A. Benčan, "Nanomechanical probing of lead-free ferroelectrics", *CIMTEC 2022*, 2022, Perugia, Italy.

M. Fricaudet, B. Dkhil, M. Otonicar, M. Koblar, K. Žiberna, S. Salmanov, D. He, J. Kreisel, T. Rojac, P.-E. Janolin, S. K. Chandrashekar and A. Bradesko, "Multiphysic energy harvesting using PVDF-based materials", *57th International Conference on Microelectronics, Devices and Materials & The Workshop on Energy Harvesting: Materials and Applications*, 2022, Maribor, Slovenia.

S. W. Konsago, K. Žiberna, B. Kmet, A. Benčan, H. Urišč and B. Malič, "Influence of the choice of the solvents on microstructure and properties of solution-derived barium titanate-based thin films", *57th International Conference on Microelectronics, Devices and Materials & The Workshop on Energy Harvesting: Materials and Applications,* 2022, Maribor, Slovenia.

M. Koblar, O. Condurache, K. Žiberna, K. Pušnik, Črešnar, , K. Fras, L. Zemljič, M. Kušter, A. Benčan and M. Otoničar, "Correct determination of chemical composition using Monte Carlo simulation in Energy Dispersive X-ray Spectroscopy (EDXS)", *4th Slovene Microsocpy Symposyum*, 2022, Ankaran, Slovenia.

K. Žiberna, V. Fišing, A. Drnovšek, H. Uršič and A. Benčan, "Site-specific mechanical probing of lead-free ferroelectric materials", *4th Slovene Microsocpy Symposyum*, 2022, Ankaran, Slovenia.

K. Žiberna, A. Drnovšek, M. Koblar, T. Rojac, H. Uršič and A. Benčan, "Mechanical response of domain walls in lead-free ferroelectrics", *16th Multinational Congress on Microscopy,16MCM*, 2022, Brno, Czech Republic.

S. W. Konsago, K. Žiberna, B. Kmet, A. Benčan, H. Urišč and B. Malič, "Influence of solution formulation on microstructural features of solution-derived barium titanate-based thin films", *14th Jožef Stefan International Postgraduate School Students' Conference*, 2022, Kamnik, Slovenia.

M. Fricaudet, S. Salmanov, M. Koblar, T. Rojac, K. Žiberna, M. Otoničar, T. Martin, D. He, B. Dkhil, P.-E. Janolin and A.Bradeško, "Optimizing PVDF-based materials for multiphysic energy harvesting", *XVIIIth ECerS conference : Conference & Exhibition of the European Ceramic Society*, 2023, Lyon, France.

S. W. Konsago, K. Žiberna, B. Kmet, A. Benčan, H. Urišč, Geoff Brennecka and B. Malič, "Microstructure and properties of $0.5Ba(Zr_{0.2}Ti_{0.8})O_3$-$0.5(Ba_{0.7}Ca_{0.3})TiO_3$ thin films by ethylene-glycol based solution route", *XVIIIth ECerS conference : Conference & Exhibition of the European Ceramic Society*, 2023, Lyon, France.

K. Žiberna, M. Bah, F. Levassort, A. Drnovšek, G. Dražić, H. Uršič and A. Benčan, "Mechanical probing of ferroelectric bulk materials using nanoscale techniques", *XVIIIth ECerS conference : Conference & Exhibition of the European Ceramic Society*, 2023, Lyon, France.

S. W. Konsago, K. Žiberna, A. Matavž, B. Mandal, S. Glinšek, A. Benčan, H. Uršič, G. Brennecka and B. Malič, "Enhanced dielectric, electromechanical and energy storage properties of $0.5Ba(Zr_{0.2}Ti_{0.8})O_3$–$0.5(Ba_{0.7}Ca_{0.3})TiO_3$ thin films by the ethylene glycol based chemical solution deposition", *ISOE2023: 7th International School of Oxide Electronics*, 2023, Cargèse, France.

K. Žiberna, M. Šadl, A. Drnovšek, G. Dražić, H. Uršič and A. Benčan, "Effect of heat-treatment on microstructure and mechanical properties of thick films prepared by aerosol deposition", *CrossNano 2023 : Crossborder Workshop in Nanoscience and Nanotechnology*, 2023, Trieste, Italy.

K. Žiberna, M. Šadl, A. Drnovšek, G. Dražić, H. Uršič and A. Benčan, "Impact of thermal treatment on the microstructure and mechanical properties of aerosol-deposited $Pb(Mg_{1/3}Nb_{2/3})O_3$–$PbTiO_3$ thick films", *Beyond imperfections: new structure-property relationships in ceramics and glasses: 788. WE-Heraeus-Seminar*, 2023, Bad Honnef, Germany.

S. W. Konsago, K. Žiberna, A. Benčan, H. Urišč and B. Malič, "Ethylene-glycol based chemical solution deposition of $0.5Ba(Zr_{0.2}Ti_{0.8})O_3$–$0.5(Ba_{0.7}Ca_{0.3})TiO_3$ thin films", *International Conference on Microelectronics, Devices and Materials & The Workshop on Chemical sensors: Materials and Applications*, 2023, Lipica, Slovenia.

K. Žiberna, M. Koblar, M. Bah, F. Levassort, G. Dražić, H. Uršič and A. Benčan, "Local mechanical properties of $BiFeO_3$ ceramics", *Nanobrücken 2024: A Nanomechanical testing conference and Bruker user meeting*, 2024, Valpre-Lyon, France.

K. Žiberna, M. Koblar, M. Bah, F. Levassort, H. Uršič, G. Dražić and A. Benčan, "Structural and microstructural defects in mechanically deformed lead-free ferroelectrics", *Microscopy & Analysis 2024 Meeting*, 2024, Cleveland, USA.

M. Otoničar, M. Lachhab, S. Salmanov, A. A. Shah, K. Žiberna, A. Benčan, T. Rojac and D. Kuščer, "Pressure-induced dissolution and plastic deformation of perovskite ferroelectric", *IEEE UFFC-JS 2024*, 2024, Taipei, Taiwan.

M. Lachhab, M. Koblar, S. Salmanov, K. Žiberna, G. Dražić, M. Vallet, B. Dkhil and M. Otoničar, "Unraveling crystal lattice of cold sintered lead-free perovskite", *FerroSchool 2024*, 2024, Ljubljana, Slovenia.

S. W. Konsago, K. Žiberna, A. Matavž, B. Mandal, S. Glinšek, A. Benčan, H. Uršič and B. Malič, "Electromechanical and energy storage properties of $0.5Ba(Zr_{0.2}Ti_{0.8})O_3$—$0.5(Ba_{0.7}Ca_{0.3})TiO_3$ thin films by chemical solution deposition", *FerroSchool 2024*, 2024, Ljubljana, Slovenia.

G. Dražić, K. Žiberna, O. Condurache and A. Benčan, "Exploring polar ordering in lead-free $K_{0.5}Na_{0.5}NbO_3$ ferroelectrics using in situ biasing and 4D STEM techniques", *European Microscopy Congress 2024*, 2024, Copenhagen, Denmark.

S. W. Konsago, K. Žiberna, J. Ekar, A. Matavž, J. Kovač, A. Benčan, H. Uršič and B. Malič, "Homogeneity and multifunctionality of $0.5Ba(Zr_{0.2}Ti_{0.8})O_3$-$0.5(Ba_{0.7}Ca_{0.3})TiO_3$ ceramic thin films by chemical solution deposition", *Electroceramics XIX Conference*, Vilnius, Lithuania.

S. W. Konsago, K. Žiberna, A. Matavž, B. Mandal, A. Benčan, S. Glinšek and B. Malič, "Microstructure design for optimized functional properties of $Ba(Zr_{0.2}Ti_{0.8})O_3$-$(Ba_{0.7}Ca_{0.3})TiO_3$ thin films by chemical solution deposition", *ECAPD 2024: European Conference on Applications of Polar Dielectrics*, 2024, Trondheim, Norway.

S. W. Konsago, K. Žiberna, B. Mandal, S. Glinšek, A. Matavž, H. Uršič and B. Malič, "Energy storage properties of $0.5Ba(Zr_{0.2}Ti_{0.8})O_3$-$0.5(Ba_{0.7}Ca_{0.3})TiO_3$ thin films by ethilene glycol-based chemical solution deposition", *59th International Conference on Microelectronics, Devices and Materials & Workshop on Electromagnetic Compatibility: From Theory to Practice*, 2024, Rimske Toplice, Slovenia.

K. Žiberna, M. Koblar, M. Poberžnik, A. Kokalj, G. Dražić and A. Benčan, "STEM study of spontaneous polarization direction and point defects in $(K_{0.5}Na_{0.5})NbO_3$", *5th Slovene Microscopy Symposyum*, 2024, Rogla, Slovenia.

M. Otoničar, M. Lachhab, M. Koblar, S. Salmanov, K. Žiberna, G. Dražić and A. Benčan, "Electron-microscopy study of pressure-dissolution process in perovskites", *5th Slovene Microscopy Symposyum*, 2024, Rogla, Slovenia.

M. Lachhab, K. Žiberna, S. Salmanov, M. Koblar and M. Otoničar, "Lattice strain analysis of cold-sintered perovskites", *5th Slovene Microscopy Symposyum*, 2024, Rogla, Slovenia.

M. Koblar, K. Žiberna, S. Salmanov, M. Otoničar, G. Dražić and A. Benčan, "TEM sample preparation of perovskite ferroelectrics using a combination of ion-beam-milling techniques", *5th Slovene Microscopy Symposyum*, 2024, Rogla, Slovenia.

K. Žiberna, M. Koblar, M. Bah, F. Levassort, H. Uršič, G. Dražić and A. Benčan, "Plastic deformation of $BiFeO_3$ under a cube-corner indentation probe", *29th International Conference on Materials and Technology*, 2024, Portorož, Slovenia.

M. Lachhab, S. Salmanov, K. Žiberna, M. Koblar, B. Dkhil and M. Otoničar, "Crystallographic defects in cold-sintered ferroelectric ceramics", *16th Jožef Stefan International Postgraduate School Students' Conference*, 2024, Piran, Slovenia.

Unpublished Scientific Conference Contributions

G. Ferrero, K. Žiberna, B. Malič and T. Rojac, "Piezoelectric properties of mechanochemically processed $BiFeO_3$—$BaTiO_3$ ceramics", *ISAF 2022 : ISAF-PFM-ECAPD*, 2022, Tours, France.

S. Salmanov, M. Yao, M. Koblar, K. Žiberna, A. Benčan, B. Dkhil, A. Kocjan, B. Malič, T. Rojac, D. Kuščer and M. Otoničar, "Pressure-solution-induced features in selected cold-sintered perovskites", *IEEE International Symposium on Applications of Ferroelectrics (ISAF), International Symposium on Integrated Functionalities (ISIF) & Piezoresponse Force Microscopy Workshop (PFM), ISAF-ISIF-PFM 2023*, 2023, Cleavland, USA.

S. W. Konsago, K. Žiberna, B. Kmet, H. Uršič, B. Malič, "Chemical solution deposition of barium titanate based thin films using different combinations of solvents", *7th Japan-Slovenia web workshop on piezoelectric thin films*, Ljubljana, Slovenia.

S. W. Konsago, K. Žiberna, A. Matavž, G. Brennecka, H. Uršič, B. Malič, "$0.5Ba(Zr_{0.2}Ti_{0.8})O_3$–$0.5(Ba_{0.8}Ca_{0.3})TiO_3$ thin films by the ethylene glycol based chemical solution deposition", *8th Japan-Slovenia web workshop on piezoelectric thin films*, Ljubljana, Slovenia.

K. Žiberna, G. Dražić and A. Benčan, "4D STEM of $Pb(Mg_{1/3},Nb_{2/3})O_3$–$PbTiO_3$ thick films on stainless-steel substrate: questions in need of answers", *AdSTEM3-European School on 4D STEM Imaging*, Piran, Slovenia, 2023.

K. Žiberna, M. Koblar, G. Dražić and A. Benčan, "Scanning transmission electron microscopy study of mechacanially deformed lead-free ferroelectrics", *Solid State Studies in Ceramics, Gordon Research Conference*, 2024, South Hadley, USA.

Awards

- Poster selected among top three in the field of material science, 16th Multinational Congress on Microscopy, 4th–9th September 2022, Brno, Czech Republic
  Poster title: *Mechanical response of domain walls in lead-free ferroelectrics*
- Best student talk award, Nanobrücken 2024, 19th–21st March 2024, Lyon, France
  Presentation title: *Local mechanical properties of $BiFeO_3$ ceramics*
- Best poster award in the field of materials science, 5th Slovene Microscopy Symposium, 16th–17th May 2024, Rogla, Slovenia
  Poster title: *STEM Study of Spontaneous Polarization Direction and Point Defects in $(K_{0.5}Na_{0.5})NbO_3$*
- 1st place in the student talk contest, 29th International Conference on Materials and Technology, 2nd–4th September 2024, Portorož, Slovenia
  Presentation title: *Plastic Deformation of $BiFeO_3$ Under a Cube-Corner Indentation Probe*

Workshop attendance

- AdSTEM 2023-European School on 4D STEM imaging, 15th–17th May 2023, Piran, Slovenia
- 2023 ECerS Summer School on Advanced Characterization Techniques, 29th–30th June 2023, Lyon, France

Research Visit

- GREMAN, University of Tours, CNRS, INSA Centre Val de Loire, 27th February–6th March 2023
  Research topic: *Quantitative Elastic Measurements of Nanometric Defects in Ferroelectrics Using Advanced Atomic Force Microscopy Techniques*

Biography

The author was born on January 23rd, 1995, in Postojna. After finishing the Gymnasium in Sežana in 2014, she enrolled at the Faculty of Chemistry and Chemical Technology at the University of Ljubljana. In 2018, she obtained a BSc degree in Chemistry and started working as a student in the Electronic Ceramics Department at the Jožef Stefan Institute. She continued her studies at the Faculty of Chemistry and Chemical Technology at the University of Ljubljana and completed her MSc studies in 2020. The MSc thesis entitled 'Ferroelectric domain structure of piezoelectric solid solution $BiFeO_3$-$SrTiO_3$ was prepared under the supervision of Prof. Dr. Tadej Rojac at the Electronic Ceramics Department, Jožef Stefan Institute.

In 2020, she enrolled in the Sensor Technologies PhD program at the Jožef Stefan International Postgraduate School. She took up the position of Young Researcher in the Electronic Ceramics Department at the Jožef Stefan Institute under the supervision of Prof. Dr. Andreja Benčan Golob and the co-supervision of Assoc. Prof. Dr. Hana Uršič. Her research focuses on the structural and microstructural characterization of lead-free ferroelectric materials using advanced electron microscopy techniques, spanning from the micro- to the atomic scale, with a focus on defects induced by mechanical deformation.